A STUDY OF DYNAMIC COMPRESSOR SURGE CONTROL STRATEGIES FOR A GAS TURBINE ENGINE

by

Gregory Scott McNulty

B.S. Aeronautics & Astronautics, Purdue University (1991)

Submitted to the Department of Aeronautics and Astronautics
in Partial Fulfillment of the Requirements for the Degree of

Master of Science in Aeronautics and Astronautics

at the

Massachusetts Institute of Technology
September 1993

Signature of Author _____
Department of Aeronautics and Astronautics
September 20, 1993

Certified by _____
Professor Edward M. Greitzer
Thesis Supervisor

Accepted by _____
Professor Harold Y. Wachman
Chairman, Department Graduate Committee

A STUDY OF DYNAMIC COMPRESSOR SURGE CONTROL STRATEGIES FOR A GAS TURBINE ENGINE

by

Gregory Scott McNulty

Submitted to the Department of Aeronautics and Astronautics on September 21, 1993
in partial fulfillment of the requirements for the degree of
Master of Science in Aeronautics and Astronautics

Abstract

An analytical study has been performed to assess actuation and sensing approaches for dynamic surge suppression in a helicopter gas turbine engine through the use of closed-loop feedback control. The motivation for the research is to relax the constraints that aerodynamic instabilities, specifically compressor surge, place on gas turbine engine operating range and performance.

A lumped parameter model of a helicopter gas turbine engine was used to assess the importance of features of the engine environment, such as high compressor pressure ratios, non-isentropic processes (specifically, combustor heat-release and energy dynamics) and rotor speed fluctuations. The analysis showed that for the pressure ratios and heat-release levels expected, density fluctuations at the compressor inlet and heat addition in the combustor can have a significant effect, but rotor speed fluctuations had a negligible influence on engine stability.

Various surge control actuation strategies were evaluated involving mass injection at the diffuser throat, a close-coupled valve (flow-fence), mass injection at the compressor inlet, mass flow bleed at the compressor exit, fuel-flow modulation, and an auxiliary plenum which functions as an aerodynamic damper. The sensors examined were compressor duct mass flow, burner pressure, and compressor inlet total pressure. A stability analysis of each actuator/sensor pair was performed using model parameters estimated for a LTS-101 helicopter engine. Constraints were imposed on the controller bandwidth and gain to represent practical implementation limitations.

The results indicate that the most effective actuation approaches are close-coupled to the compressor to modulate the flow momentum in the duct, namely, diffuser throat injection, the close-coupled valve, and compressor inlet injection. All three actuators performed well with mass flow sensing, however, the practical constraints on actuator bandwidth were found to limit their performance. Diffuser throat injection combined with an inlet total pressure sensor was the most promising scheme. Several actuator/ sensor combinations were also observed to perform well with low bandwidth actuators. Finally, for the engine system parameters examined a passive aerodynamic damper was also predicted to provide some stabilization capability, although considerably less than the best active control approaches.

Thesis Supervisor: Professor Edward M. Greitzer
Title: H.N. Slater Professor of Aeronautics and Astronautics

Acknowledgements

My stay at the Gas Turbine Lab has been a rewarding experience that has been shaped by many people. First and foremost, I wish to thank my advisor and teacher Prof. Greitzer for his constant support and guidance. I am truly grateful for the opportunity to have worked with him. I would also like to thank Prof. Epstein for his interest, useful suggestions and support. Jon Simon, Dan Gysling and Gavin Hendricks are also appreciated for many useful discussions and explanations during this project. Thanks are also given to Professors Cumpsty and Marble for their advice and encouragement.

Thanks are also in order to my friends at GTL who have made my stay at MIT an enjoyable one. I wish them success and happiness in the future.

Special thanks is expressed to my Mom, Dad and sister Shelly for their love and support. Without them this would have never been possible.

Finally I wish to express my gratitude to Laura. Her love and patience during the past two years has been remarkable. I can only hope to be as understanding and supportive in her years ahead in medical school.

Support for this research was provided by the following sources: the Office of Naval Research under Grant Number N00014-91-J-1575, Dr. E. Hendricks technical monitor, Textron Lycoming Corp., Dr. A. Sehra technical monitor, and by the Air Force Research in Aero-Propulsion Technology (AFRAPT) Program, under Grant Number AFOSR-91-0052. This support is gratefully acknowledged.

Table of Contents

List of Figures

Chapter 1

Chapter 2

Chapter 3

3.23 Maximum Stable Compressor Slope for Compressor Inlet Injection with Compressor Mass Flow Sensor as a Function of the Stability Parameter and Inertia Ratio: ω_C/ω_H=3, -2.5<K_N<2.5, θ_B=2, LTS-101 Ch'ic, $P^*_{O,inj}$=2.

3.24 Maximum Stable Compressor Slope for Compressor Inlet Injection with Compressor Mass Flow Sensor as a Function of the Controller Bandwidth and Inertia Ratio: β=0.5, -2.5<K_N<2.5, θ_B=2, LTS-101 Ch'ic, $P^*_{O,inj}$=2.

3.25 Schematic of Compressor Exit Bleed Actuator.

3.26 Closed-Loop Stability for Compressor Exit Bleed with Compressor Mass Flow Sensor (W_C) as a Function of Controller Bandwidth (ω_C/ω_H) and Gain (K_N): β=0.4, L_u/L_d=0.4, θ_B=2, LTS-101 Ch'ic.

3.27 Closed-Loop Stability for Compressor Exit Bleed with Downstream Duct Mass Flow Sensor (W_d) as a Function of Controller Bandwidth (ω_C/ω_H) and Gain (K_N): β=0.4, L_u/L_d=0.4, θ_B=2, LTS-101 Ch'ic.

3.28 Closed-Loop Stability for Compressor Exit Bleed with Burner Pressure Sensor (P^*_B) as a Function of Controller Bandwidth (ω_C/ω_H) and Gain (K_N): β=0.4, L_u/L_d=0.4, θ_B=2, LTS-101 Ch'ic.

3.29 Closed-Loop Stability for Compressor Exit Bleed with Inlet Total Pressure Sensor ($P^*_{O,2}$) as a Function of Controller Bandwidth (ω_C/ω_H) and Gain (K_N): β=0.4, L_u/L_d=0.4, θ_B=2, LTS-101 Ch'ic.

3.30 Maximum Stable Compressor Slope for Compressor Exit Bleed with Compressor Mass Flow Sensor as a Function of the Stability Parameter and Inertia Ratio: $(\omega_C/\omega_H)_{opt}$=0.5, -2.5<$K_N$<2.5, θ_B=2, LTS-101 Ch'ic.

3.31 Closed-Loop Stability for Fuel-Flow Modulation with Compressor Mass Flow Sensor (W_C) as a Function of Controller Bandwidth (ω_C/ω_H) and Gain (K_N): β=0.4, L_u/L_d=0.4, θ_B=2, LTS-101 Ch'ic.

3.32 Closed-Loop Stability for Fuel-Flow Modulation with Burner Pressure Sensor (P^*_B) as a Function of Controller Bandwidth (ω_C/ω_H) and Gain (K_N): β=0.4, L_u/L_d=0.4, θ_B=2, LTS-101 Ch'ic.

3.33 Closed-Loop Stability for Fuel-Flow Modulation with Inlet Total Pressure Sensor ($P^*_{O,2}$) as a Function of Controller Bandwidth (ω_C/ω_H) and Gain (K_N): β=0.4, L_u/L_d=0.4, θ_B=2, LTS-101 Ch'ic.

3.34 Maximum Stable Compressor Slope for Fuel-Flow Modulation with Compressor Mass Flow Sensor as a Function of the Stability Parameter and Inertia Ratio: $(\omega_C/\omega_H)_{opt}$=0.4, -2.5<$K_N$<2.5, θ_B=2, LTS-101 Ch'ic.

Appendix A

Nomenclature

Symbols:

a	Speed of Sound
A	Flow Area
A	Jacobian Matrix
B	Stability Parameter (defined in Eqn. 1.1)
BL_{th}	Blockage at Diffuser Throat
ch'ic	Characteristic
c_P	Specific Heat of Air at Constant Pressure
c_V	Specific Heat of Air at Constant Volume
C_P	Diffuser Static Pressure Coefficient
$C_{P,i}$	Ideal (Inviscid) Diffuser Static Pressure Coefficient
$F(\gamma)$	Function of Specific Heat Ratio defined in Eqn. 2.20
F( )	Function
G(s)	Laplace Transfer Function
G( )	Implicit Function
h_O	Total Enthalpy
HV	Lower Heating Value of Fuel
I	Engine-to-Damper Inertia Ratio (defined in Eqn. 3.20)
J	Polar Moment of Inertia of Compressor/Turbine Spool
K	Burner-to-Damper Compliance Ratio (defined in Eqn. 3.22)
K_N	Normalized Controller Gain
L	Length
$\overline{m}_C$	Slope of Compressor Pressure Ratio Characteristic ($\equiv \left(\frac{\partial \pi_C}{\partial W_{C,COR}}\right)$)

$m_{C,\theta}$		Slope of Compressor Temperature Ratio Characteristic ($\equiv \left(\overline{\frac{\partial \theta_C}{\partial W_{C,COR}}}\right)$)
$\overline{m}_{C,NS}$		Slope of Compressor Pressure Ratio Characteristic at Neutral Stability
$\overline{m}_{C,MAX}$		Maximum Stable Slope of Compressor Pressure Ratio Characteristic
$\dot{m}$		Mass Flow
M		Mach Number
P		Static Pressure
P_O		Total Pressure
$\dot{Q}$		Heat-Release Rate
R	or	Ideal Gas Constant for Air Radius
s	or	Arc Length Laplace Transform Variable
t		Time
T		Static Temperature
T_O		Total Temperature
TR		Burner-to-Damper Temperature Ratio (defined in Eqn. 3.24)
U		Velocity
V		Volume
VR		Burner-to-Damper Volume Ratio (defined in Eqn. 3.23)
W		Non-Dimensional Mass Flow (defined in Eqn. 2.23)
$W_{C,COR}$		Compressor Corrected Mass Flow (defined in Eqn. 2.15)
x		Axial Distance
X_{fp}		Normalized Flow-Fence Position
β		Stability Parameter (defined in Eqn. 2.33)
γ		Specific Heat Ratio for Air
Γ		Torque

η	Efficiency
θ	Temperature Ratio (total-to-total)
μ_C	Compressor Work Coeficient (defined as $\Delta h_{O,C}/U_{tip}^2$)
π	Pressure Ratio (total-to-total)
ρ	Density
τ	Non-Dimensional Time (defined in Eqn. 2.27)
ω_C	Natural Frequency of Controller Dynamics
ω_H	Helmholtz Resonator Frequency (defined in Eqn. 2.28)
ω_{NS}^*	Normalized Surge Frequency at Neutral Stability (defined as ω_{NS}/ω_H)
ω_R^*	Reduced Frequency (defined in Eqn. 2.2)
Ω	Rotor Speed
ζ_C	Damping Ratio of Controller Dynamics

Subscripts:

1-6	Engine Stations (defined in Fig. 2.1)
a	Ambient Conditions
AD	Aerodynamic Damper
bl	Bleed
B	Burner/Combustor/Plenum Chamber
C	Compressor
C-VD	Compressor minus Vaned-Diffuser
cd	Entire Compressor Duct
d	Downstream Compressor Duct
eff	Effective
ex	Diffuser Exit
F	Fuel
fs	Freestream

inj	Injector
opt	Optimum Value
peak	Peak of Compressor Characteristic
P	Plenum/Burner/Combustor
tip	Rotor Tip
T or	Turbine Throttle
u	Upstream Compressor Duct
US	Unsteady
VD	Vaned-Diffuser

Superscripts:

*	Non-Dimensional Quantity

Operators:

$(\hat{})$	Perturbation Quantity
$(\bar{})$	Value at Steady-State Operating Point
$(\tilde{})$	Volumetrically Averaged
$\Delta( )$	Difference

Chapter 1
Introduction

1.1 Background

It is well known that the lower useful operating range of both axial and centrifugal compressors in aero gas turbine engines (as well as many other turbomachine pumping systems) is limited by the onset of either surge or rotating stall. Surge and rotating stall are two distinctly different, but not unrelated, types of *self-excited* aerodynamic instabilities which are usually encountered as the compressor is throttled slightly past the peak of its pressure rise verses mass flow performance curve. Surge is a global *system* instability characterized by large amplitude, essentially one-dimensional, oscillations in engine mass flow and pressure as shown schematically in Fig. 1.1. Surge depends not only upon the local compressor performance but also the ducting, volumes and throttling elements in the system. Rotating stall is a *localized* instability characterized by two-dimensional (or three-dimensional) regions of low mass flow (stall cells) that rotate about the compressor annulus at some fraction of the rotor speed. In fully developed rotating stall the annulus averaged mass flow and pressure rise are essentially constant at much reduced values from the unstalled state (see Fig 1.1). Both types of instabilities are undesirable for performance and safety reasons and there is thus a strong desire to avoid their occurance at all times.

Conventional practice in the aero engine industry is to use a safety margin, referred to as *surge margin*, so the compressor always operates a safe distance from the stability limit line or *surge line*. These surge margins can be up to 25 percent to allow for variations in the surge and operating lines due to inlet distortion, engine transients, manufacturing tolerances and deterioration. The necessity for this substantial surge

margin may restrict the compressor from operating in regions of higher pressure rise and efficiency.

In recent years much interest has been expressed in the development of methods to relax or control the constraints placed on engine performance and operating range by compressor aerodynamic instabilities. One approach which has received considerable interest is the use of closed-loop feedback control to *dynamically* suppress these instabilities, shifting the surge line to lower flow rates as illustrated schematically in Fig. 1.2. The conceptual basis for dynamic control is based on the observation that the large amplitude limit cycle phenomena of surge and rotating stall initially begin as small amplitude disturbances. Epstein et al. [1] first proposed the idea of stabilizing the compressor by suppressing the unsteady disturbances while they are small, thus requiring little control power. In this approach a sensor detects the fluid disturbances and a signal is fedback (modified via an appropriate control law) to an actuator which creates the appropriate perturbations. The closed-loop combination of the compressor and controller behaves as a different system with new dynamic properties that can be designed to enhance the stability of the system. The advantage of this method is that by only actuating on the unsteady disturbances the steady-state compressor performance should remain virtually unaltered.

To date both active and aeromechanical feedback methods have been studied to stabilize compression systems under the single title of dynamic control. Active control generally refers to the use of external electromechanical actuators, plus sensors and processors to provide feedback in the system. Aeromechanical control, on the other hand, refers to the use of a tailored structure, or an external aerodynamic device, to provide feedback through unsteady interaction with the compression system aerodynamics. The two different methods of providing feedback are similar in physical mechanism, however,

because both act to increase the unsteady energy dissipation (i.e. damping) by modifying the system dynamics.

Dynamic control of surge and rotating stall has been demonstrated in university laboratories on small centrifugal turbochargers [2,3,4,5] and low speed single and three stage axial compressors [6,7,8], respectively. Both active and aeromechanical feedback methods have been used. Although the results of these initial proof of concept demonstrations are promising (increases in the stable flow range of 25 percent for surge and 20 percent for rotating stall), the feasibility or effectiveness of using dynamic control in actual engine operating environments has yet to be resolved. Recently several university, industry and government research programs have been launched to address issues related to the implementation of dynamic surge and rotating stall control in high performance aero engines. One such project at the MIT Gas Turbine Lab involves the dynamic control of a helicopter engine [9,10,11]. This thesis is concerned with issues related to the implementation of dynamic surge control in a high performance helicopter engine.

1.2 Problem Definition

Previous demonstrations of dynamic surge control have shown that an accurate surge model is necessary for the design of successful control strategies [2,3,4,5]. There are several *lumped parameter* surge models essentially based on that proposed by Emmons, et al. [12] and further developed by Greitzer [13]. This relatively simple model has been shown to capture the surge dynamics of the laboratory compressor rigs that have been tested, but its utility for a helicopter gas turbine engine has yet to be resolved. For instance, it is unclear how the surge dynamics are affected by compressibility, high pressure ratios, heat-release in the combustor and compressor/turbine shaft dynamics. Therefore, there is a need to assess the validity of the lumped parameter modelling

assumptions for a gas turbine engine, and to assess the importance of some of the additional phenomena present in these engines.

A goal of dynamic surge control is to achieve maximum flow range extension, which essentially means to stabilize the system to maximum compressor slopes. The latter is a more appropriate figure of merit because it affects stability directly; stability is more difficult to achieve as the slope of the pressure rise verses flow characteristic is increased. This creates a challenge to dynamic surge control because high pressure ratio compressors tend to have steeply sloped characteristics, and the compression system must therefore be stabilized to large slopes to achieve significant flow range extension. In other words, more effective actuators are needed for successful surge control in high performance gas turbine engines.

Another issue is the restricted accessibility available for actuators. Most of the actuation approaches used to stabilize surge in the laboratory compressor rigs (e.g. movable plenum wall) are not practical for implementation in existing gas turbine engines. Thus new actuation approaches must be developed which do have a possibility for successful implementation in a gas turbine engine.

1.3 Previous Work

1.3.1 Surge Modelling

In 1955 Emmons, et al. [12] first proposed the analogy between surge oscillations in a compression system and the acoustic oscillations of a Helmholtz resonator. In this pioneering work the fluid in the compressor ducting is modelled as the (incompressible) system inertia, the fluid in the plenum chamber as the (compressible) system compliance, and the compressor and throttle as damping elements (modelled as quasi-steady actuator disks). The stability of the compression system to small perturbations was examined by linearizing the resulting lumped parameter equations.

In 1976 Greitzer [13] extended this model to the non-linear regime to study the post-stall transients of a low speed 3-stage axial compressor rig. His numerical simulations of the limit cycle behavior of this compression system showed good agreement with experiment. A non-dimensional parameter was developed as the dominant similarity parameter upon which the surge dynamics depends. This parameter, B, is defined as

$$B \equiv \frac{U_T}{2 \cdot a_P} \sqrt{\frac{V_P}{L_{cd} \cdot A_C}} = \frac{U_T}{2 \cdot \omega_H \cdot L_{cd}} \qquad (1.1)$$

The physical mechanism responsible for surge was also identified as a self-excited dynamic instability that occurs when the compressor, while operating at positive slopes, feeds more unsteady mechanical energy into the flow disturbances than the throttle can dissipate.

Fink [14] used the same basic lumped parameter surge model to study the linear and non-linear surge dynamics of a small centrifugal turbocharger rig. He included the rotor speed variations (i.e. shaft dynamics) due to torque imbalances between the compressor and the drive turbine. Non-linear simulations of both "mild" and "deep" surge cycles showed good agreement with the measured data. Fink also presented a linear stability analysis to assess the importance of turbospool shaft dynamics and a (first-order) time lag in compressor response. Both phenomena had a slight stabilizing influence on linear stability (i.e. surge inception) for practical values of rotor inertia and compressor time lag, but a much greater impact on the non-linear surge dynamics.

Simon [5] experimentally measured the transfer function of a small centrifugal turbocharger to assess the validity of the simple actuator disk compressor model. His comparisons of measured and analytically predicted transfer functions using various modelling assumptions allowed the following conclusions to be made: (1) an actuator disk model gives good quantitative agreement with measured data, (2) the quasi-steady assumption is appropriate for control design purposes and (3) a first-order time lag is a

valid model of the unsteady compressor response at reduced frequencies of order unity, as defined in Chapter 2.

Several researchers [2,3,4,5] have used this basic model in the design of dynamic surge control strategies for small centrifugal turbocharger rigs. The linearized lumped parameter surge equations were modified to include the effects of the actuators, sensors and control laws and parametric studies were performed to the find the optimum control parameters that maximized system stability . Comparison of the measured control effectiveness with the theoretically predicted performance indicated that the lumped parameter model adequately captured the surge dynamics as well as showed its usefulness as a tool for the design of dynamic control strategies.

More complex surge models have also been developed to include additional phenomena believed to be important for high performance gas turbine engine compression systems. Several surge models have been developed which relax the isentropic process assumption in the plenum [15] and allow a finite heat-release [16]. However, no clear criteria were identified which must be violated for the isentropic plenum assumption to become invalid.

Other researchers [17,18] have developed multi-volume blade-row by blade-row models of multi-stage axial flow compressors . In these models the single compressor actuator disk is replaced by multiple blade-row actuator disks with inertia and compliance between each stage. It is not clear from this work when the compressor internal stage dynamics are important and when they are not. The recent push to demonstrate dynamic control in high performance compressors has made this an important research topic. In one such project [19, 20] a compressible (distributed parameter) linearized model was developed to study the affect of compressibility on surge, rotating stall and acoustic instabilities in high speed multi-stage axial compressors. In another project [37] a subsonic compressible model was used to study the active control of rotating stall, not

surge, in a low speed centrifugal compressor. No research to date has addressed the different stalling behavior observed in high and low pressure ratio centrifugal machines.

1.3.2 Dynamic Control of Surge

As mentioned above, there have been several successful demonstrations of dynamic surge control using both active and aeromechanical feedback techniques. Huang [2] first demonstrated active surge control using a movable plenum wall sensing plenum pressure; Pinsley [3] actively modulated a variable area throttle valve at the plenum exit also sensing plenum pressure. Both of these approaches used proportional control laws. Gysling [4] demonstrated the feasibility of an aeromechanical feedback approach using a structurally tailored plenum wall, driven by pressure perturbations, to achieve dynamic surge control. These approaches achieved flow range extensions on the order of 25 percent by actuating and sensing in the plenum chamber downstream of the compressor.

Simon [5] studied a variety of active surge control strategies using proportional (constant gain) control. In this study combinations of 1-D actuator and sensor pairs were modelled and analyzed as shown in Fig. 1.3. Several important conclusions were drawn from the results:

- The proper pairing of the actuator and sensor is crucial for successful control (in other words, no actuator is effective independent of the sensor)
- Control is more difficult as the B parameter and compressor slope are increased
- The most promising actuators are close-coupled to the compressor to alter the flow momentum, while sensing compressor mass flow
- The source of the disturbance driving the system has a strong influence on control effectiveness

Simon also experimentally demonstrated active control using a *close-coupled*, variable area throttle valve with a velocity (mass flow) sensor in the compressor duct. As

predicted, the close-coupled valve achieved a greater flow range extension than previous control strategies which actuated in the downstream plenum, although a steady-state loss across the valve was measured in the actively stabilized flow region. Simon attempted to minimize the performance penalty associated with close-coupled valve control and demonstrated an approximate 35 percent flow range extension with reduced losses.

There are several common features of the proof of concept demonstrations discussed above. The experiments were all done on small centrifugal turbocharger rigs with pressure ratios of roughly 2 and Helmholtz frequencies (roughly the time scale of the small amplitude surge inception oscillations) in the range of 10 to 30 Hertz. Thus steep compressor slopes and high actuator bandwidths were not required to achieve significant flow range extension in these systems. The work also does not address issues associated with the influence of the different stalling behavior observed in high and low pressure ratio centrifugal compressors (discussed in Ref. 21) on the effectiveness of dynamic control.

As mentioned earlier, several research projects have begun to address issues related to extending dynamic surge control into the high performance gas turbine engine regime. In one experiment [22,23], a 2.6 percent flow range extension was achieved in a 60 horsepower auxiliary power unit using air injection into the impeller and diffuser pressure sensing to stabilize surge. The authors stated that axisymmetric (one-dimensional) control was not effective and that it was necessary to stabilize the non-axisymmetric (two-dimensional) disturbance believed to be the "triggering" mechanism for surge. This work demonstrates the feasibility of active control in a noisy, high Helmholtz frequency (75 Hz) environment. However, issues related to the effect of high pressure ratio compressors on active surge control (this compressor had a pressure ratio of only three) and the validity of the lumped parameter surge model were not examined. In another active surge control project, a compressor rig has been specially developed to

simulate a gas turbine engine [24]. This rig uses a small centrifugal compressor with a pressure ratio of roughly three and a large plenum chamber that gives a Helmholtz frequency on the order of 10 Hz.

As alluded to earlier, the MIT Gas Turbine Lab has acquired two helicopter gas turbine engines, an Allison 250-C30 and a Lycoming LTS-101, for dynamic surge control experiments. Both engines are in the 650 horsepower class and have high performance centrifugal compressors with pressure ratios of roughly 8 to 10, transonic vaned-diffusers, and system Helmholtz frequencies above 100 Hz. As observed by Bell [9], these engines appear to exhibit much different surge inception behavior than the small centrifugal turbocharger rigs and work is currently underway to understand the engine surge dynamics as well as demonstrate dynamic control.

There are also efforts on the dynamic control of surge in multi-stage axial flow compressors. Several researchers [25,26] have analytically studied the use of 1-D actuators and sensors to dynamically control surge in axial compressors. In a different approach, Day [27] demonstrated dynamic surge control in a low speed, 4-stage axial compressor rig using 2-D actuation and sensing to stabilize the rotating stall which in these, and in other experiments by Day, was observed to precipitate the surge. Control of the machine was lost, and the compressor surged, when the rotating stall could no longer be stabilized.

1.4 Research Objectives

The following research objectives were identified as a step towards the ultimate goal of demonstrating dynamic surge control in a helicopter gas turbine engine:

- Develop and determine the validity of a lumped parameter surge model for a gas turbine engine
- Assess the importance of the following effects on engine stability:

- High compressor pressure ratios
- The effect of density fluctuations at the compressor face, due to upstream flow inertia, on compressor performance
- Non-isentropic processes, specifically, combustor heat-release and energy dynamics
- Rotor speed fluctuations due to compressor/turbine shaft dynamics

• Model and evaluate 1-D actuator/sensor pairs which have a possibility for effective implementation in a gas turbine engine

• Estimate surge model parameters for an actual helicopter engine geometry (LTS-101) and use these values in the evaluation of dynamic surge control strategies

1.5 Scope and Organization

This thesis is centered on issues related to the dynamic control of surge in high performance helicopter engines. Unfortunately, the stalling behavior of high pressure ratio centrifugal compressors is not well understood and the issue of whether rotating stall is the "triggering" mechanism for surge has not been resolved. The initial observations of Bell [9] did not find rotating disturbances, but more detailed experiments are required. Therefore to avoid possibly unnecessary complications, surge is assumed to be the dominant form of instability for the analyses of this thesis. This is an significant simplification because it allows the use of one-dimensional fluid dynamic models, actuators, and sensors to suppress the instability. The analyses in this thesis are primarily directed toward centrifugal compression systems, although the modelling may be applicable in certain axial compressor applications.

The main interest is in system stability, so only small perturbation linear stability analyses are performed. Both active and aeromechanical surge control strategies are

evaluated. Due to time limitations only proportional control laws are considered for the active control strategies.

The thesis is organized as follows. Chapter 2 presents the development of a lumped parameter surge model of a helicopter gas turbine engine. The governing equations are derived in some detail to determine the criteria that must be satisfied for the lumped parameter approximations to hold. A linear stability analysis is performed to examine the importance of features such as compressor pressure ratio, density fluctuations at the compressor face, non-isentropic processes in the burner, and rotor speed fluctuations due to compressor/turbine shaft dynamics.

Chapter 3 presents the modelling, numerical results and interpretation of the behavior of a number of feedback control strategies applied to the gas turbine engine of Chapter 2. These include: diffuser throat injection, a close-coupled valve, compressor inlet injection, compressor exit bleed, fuel-flow modulation and an aerodynamic damper (an external damped Helmholtz resonator). Chapter 4 presents the summary and conclusions of this research and makes recommendations for future work.

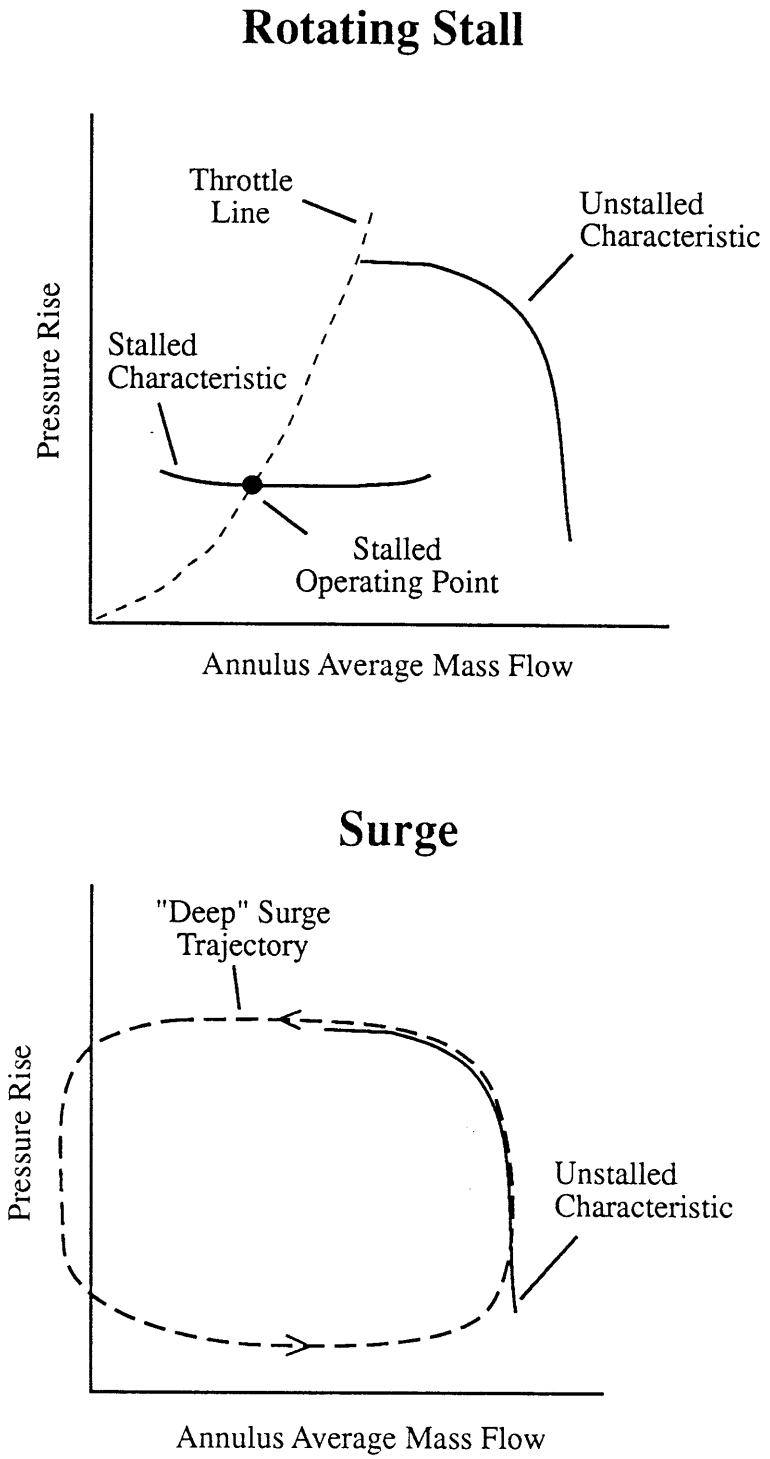

Figure 1.1: Types of Compression System Instabilities.

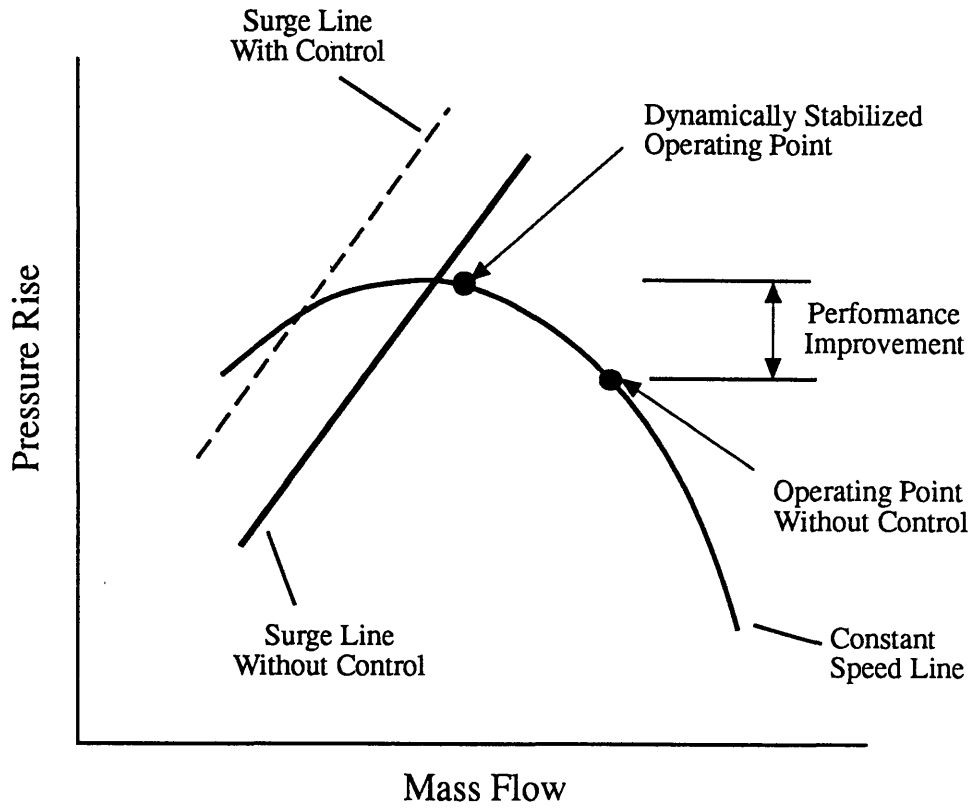

Figure 1.2: Schematic of Dynamically Stabilized Compressor.

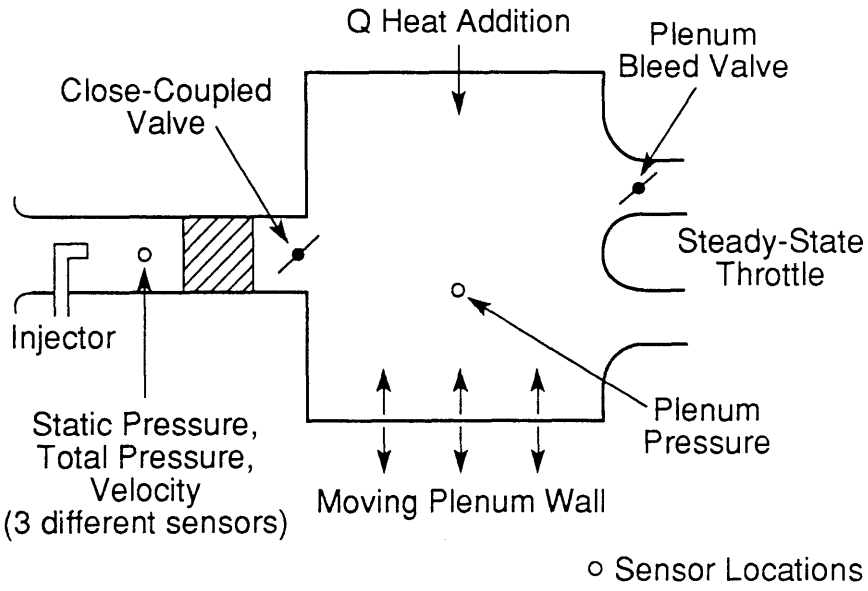

Figure 1.3: Actuators and Sensors Evaluated by Simon [5].

Chapter 2
Gas Turbine Engine Surge Model (No Control)

2.1 Introduction

This chapter presents the development of a lumped parameter surge model of a gas turbine engine. The objective is to include those phenomena which have a strong influence on the surge dynamics to provide a basic framework for the evaluation of dynamic surge control strategies for a gas turbine engine.

2.1.1 Scope of the Chapter

To examine the validity of this approach, a detailed derivation of the fluid dynamic model is given along with the criteria which must be satisfied for the lumped parameter assumptions to hold. To assess the importance of different phenomena present in a gas turbine engine several modelling assumptions are examined, namely an isentropic burner process and constant rotor speed, to determine how much the results are affected.

The system of non-linear equations governing the surge dynamics are derived and non-dimensionalized to reveal some important similarity parameters. In the non-dimensionalization, the compressor performance is specified as pressure ratio (total-to-total) versus corrected flow characteristics at constant corrected speed. The equations are linearized to study the stability of equilibrium operating points to small perturbations.

2.1.2 Organization of the Chapter

This chapter is organized as follows. First, the basic gas turbine engine surge model is developed including, a listing of the assumptions, the derivation of the governing equations for each component, and the non-dimensionalization of the

equations. Next, the linear stability analysis is presented with the method, numerical results and a discussion of the results being given. Two additional subsections examine the isentropic burner process and contant rotor speed assumptions.

2.2 Development of the Model

The compression system to be analyzed is shown schematically in Fig. 2.1. The main components of this system are: a compressor, compressor duct, combustion chamber (also called a *burner* or *plenum*), and turbine and exhaust nozzle. Heat-release, due to the combustion of fuel, is allowed in the plenum and the rotor speed is initially assumed constant.

2.2.1 Modelling Assumptions

The main modelling assumptions used are:

- 1-D, unsteady, inviscid flow of a perfect gas (thermally and calorically)
- Compressor and turbine are modelled as quasi-steady actuator disks with negligible internal inertia and compliance
- Flow in compressor ducts has negligible compliance, so that:
  - density variations are small (except across compressor)
  - mass flow is uniform throughout duct
  - acoustic disturbances are not important
- Fluid in combustor is compressible, has negligible velocity, and negligible flow inertia
- Combustion of fuel is represented as a simple heat addition process
- Total pressure is constant from combustor inlet to turbine inlet
- Turbine and exhaust nozzle are choked
- Rotor speed is constant (no shaft dynamics)
- Flow inertia downstream of combustor is negligible

- Engine inlet flow is distortion free so that inlet total pressure and temperature are constant
- Engine is at static conditions so that inlet "total" quantities are equal to ambient "static" values

2.2.2 Derivation of the Governing Equations

Compressor Duct:

The compressor duct is the inertia element of the lumped parameter compression system. As shown in Figure 2.1, the compressor is modelled as operating at an arbitrary location (i.e. not just the inlet or exit) within the constant area compressor duct. This allows the effect of the compressor placement in the duct to be assessed.

The flow in the compressor duct is assumed to be one-dimensional. This is a good approximation provided that fluid properties are essentially uniform over the cross-sectional area (specifically, if boundary-layers are thin, area changes are gradual, and radii of curvature of the passages are large). The essence of this assumption is that gradients in the flow direction are large compared to those gradients normal to the flow direction. Along this line of reasoning, velocity components normal to the bulk flow direction are assumed small enough to be ignored.

Another basic assumption is that the flow in the compressor duct is inviscid. For large Reynold number flows the pressure forces acting on the fluid are much greater than the viscous forces. In many practical situations the viscous forces are negligible, with the exception being systems with long compressor ducts where the integrated affect of viscous forces can become important.

A major assumption in the compressor duct modelling is that the dynamics are dominated by inertial effects and that compliance effects are negligible. Compliance is essentially fluid compressibility. On a global scale, if the compliance is negligible then the mass flow in the duct is uniform because the fluid has no mass storage capacity. On a

local scale, compliance is important if acoustic disturbances are significant (then both inertia and compliance must be considered). The compressibility of an unsteady flow can be neglected provided the product of the *reduced frequency*, ω_R^*, and Mach number is small, that is

$$\omega_R^* \cdot M << 1 \tag{2.1}$$

The reduced frequency is defined as [28]

$$\omega_R^* \equiv \frac{\omega_{US} \cdot L}{U} \tag{2.2}$$

where, ω_{US} is a characteristic frequency of the unsteadiness

L is a characteristic length (i.e. duct length)

U is a characteristic velocity (i.e. mean flow velocity in the duct)

Provided the inequality in Eqn. 2.1 is satisfied, the incompressible form of the momentum equation is an adequate model of the fluid dynamics in the duct. We should mention that eventhough compressibility effects are neglected in the duct fluid dynamics, density fluctuations at the compressor face (calculated from the pressure given by the incompressible momentum equation) are allowed to affect the compressor performance. As discussed in a later section, density perturbations are amplified through the compressor and this effect can become significant for the large pressure ratios considered in this study.

For the upstream duct the conservation of momentum equation in differential form is written (for an unsteady, 1-D, inviscid flow) as

$$\rho_u \cdot \frac{\partial U_u}{\partial t} + \rho_u \cdot U_u \cdot \frac{\partial U_u}{\partial x} = -\frac{\partial P_u}{\partial x} \tag{2.3}$$

This equation can be written in the following approximate form provided Mach numbers in the duct are small (say, less than 0.5)

$$\rho_u \cdot \frac{\partial U_u}{\partial t} = -\frac{\partial P_u}{\partial x} - \frac{\partial(\frac{1}{2} \cdot \rho_u \cdot U_u^2)}{\partial x} = -\frac{\partial P_{O,u}}{\partial x} \tag{2.4}$$

The total pressure in the upstream duct, $P_{O,u}$, has been approximated by the incompressible relation,

$$P_{O,u} \equiv P_u + \tfrac{1}{2} \cdot \rho_u \cdot U_u^2 \tag{2.5}$$

Neglecting Mach number effects (density gradients) in the momentum equation is justified only if $0.5 \cdot M^2 << 1$, and for a Mach number of 0.5 the error is less than 14 percent. With some manipulation, Eqn. 2.4 is integrated over the upstream duct to yield

$$\frac{d\dot{m}_u}{dt} \cdot \frac{L_u}{A_C} = P_{O,1} - P_{O,2} \tag{2.6}$$

where, the equivalent length-to-area ratio, L_u/A_C, of the upstream duct is calculated from the actual duct geometry using Eqn. 2.7 below.

$$\frac{L_u}{A_C} = \int_0^{L_u} \frac{ds}{A_u(s)} \tag{2.7}$$

Appendix A discusses in more detail the method used to estimate the equivalent model parameters from an engine geometry.

The same approximations are made in modelling the downstream duct. The conservation of momentum equation for the downstream duct is given as

$$\frac{d\dot{m}_d}{dt} \cdot \frac{L_d}{A_C} = P_{O,3} - P_{O,4} \tag{2.8}$$

where, it can be shown (see Appendix A) that the equilvalent length-to-area ratio for the downstream duct is given by

$$\frac{L_d}{A_C} = \int_{L_u}^{L_u+L_d} \frac{ds}{A_d(s)} \tag{2.9}$$

Note that the finite density rise across the compressor does not enter into the estimation of the downstream length-to-area ratio (see Appendix A for more details).

The use of the conservation of energy equation for the combustor requires that the total temperature fluctuations in the compressor duct be modelled. The total temperature at the compressor inlet, $T_{O,2}$, is estimated from the inlet total pressure (calculated using Eqn. 2.6) assuming isentropic flow from station 1 to 2. This allows $T_{O,2}$ to be calculated using the isentropic relationship

$$\frac{T_{O,2}}{T_{O,1}} = \left(\frac{P_{O,2}}{P_{O,1}} \right)^{\frac{\gamma-1}{\gamma}} \tag{2.10}$$

The total temperature at the compressor exit, $T_{O,3}$, can be calculated once the compressor temperature ratio is specified. The total temperature at the compressor duct exit, $T_{O,4}$, is estimated assuming isentropic flow from station 3 to 4. This allows $T_{O,4}$ to be calculated from the isentropic relation

$$\frac{T_{O,4}}{T_{O,3}} = \left(\frac{P_{O,4}}{P_{O,3}}\right)^{\frac{\gamma-1}{\gamma}} \tag{2.11}$$

Compressor:

The compressor is the component that provides the energy that drives the flow disturbances unstable. It would seem that compressor modelling is made difficult by the complex aerodynamic phenomena that exist within it (for example, unsteadiness, compressibility, 3-D flow), but other researchers have demonstrated that complex compressor models are not required for the system phenomena of surge. It is adequate in many situations to represent the compressor as a actuator disk which creates a finite pressure, density and temperature rise in the duct. For small perturbations, the compressor is typically assumed to behave quasi-steadily and follow its steady-state performance characteristic during unsteady flow. The quasi-steady approximation is valid provided that the reduced frequency based on characteristic compressor conditions is much less than unity (see Eqn. 2.2).

A single quasi-steady actuator disk model of the compressor is used in this study since the primary interest is in centrifugal compressor systems. The mass flow is assumed constant across the compressor,

$$\dot{m}_u(t) = \dot{m}_d(t) = \dot{m}_C(t) \tag{2.12}$$

The compressor performance is represented using its empirical steady-state performance maps. To adopt the conventional method of presenting compressor performance in gas turbine engines, the pressure ratio, π_C, and temperature ratio, θ_C, are given as functions of corrected mass flow, $W_{C,COR}$, and wheel tip Mach number, $M_{tip,2}$. This is written in functional form as:

$$\pi_C \equiv \frac{P_{O,3}}{P_{O,2}} = \pi_C(W_{C,COR}, M_{tip,2}) \qquad (2.13)$$

$$\theta_C \equiv \frac{T_{O,3}}{T_{O,2}} = \theta_C(W_{C,COR}, M_{tip,2}) \qquad (2.14)$$

where, the corrected flow and tip Mach number are defined as

$$W_{C,COR} \equiv \frac{\dot{m}_C \cdot \sqrt{R \cdot T_{O,2}}}{P_{O,2} \cdot A_C} \quad (2.15) \qquad \text{and} \qquad M_{tip,2} \equiv \frac{U_{tip}}{\sqrt{\gamma \cdot R \cdot T_{O,2}}} \quad (2.16)$$

This definition of corrected flow is slightly different than the conventional usage of the term in the gas turbine industry (the A_C and R terms in Eqn. 2.15 are retained to form a truly non-dimensional mass flow which is sometimes referred to as the *flow function*). Similarly, the wheel tip Mach number, $M_{tip,2}$, is used instead of the corrected speed since $M_{tip,2}$ is a truly non-dimensional speed (related to the corrected speed by a constant).

Combustor:

The combustor is the component that behaves as an aerodynamic spring providing the restoring force necessary to sustain an oscillation. To account for non-isentropic effects in the combustor, the conservation of energy equation along with the continuity equation is used to model the thermodynamic process. A finite heat-release is also allowed. A later section of the chapter examines the isentropic assumption to determine the importance of non-isentropic processes on engine stability.

An assumption in the modelling of the combustor is that the dynamics are dominated by compliance effects and that inertial effects are negligible. Pressure changes due to inertial effects scale with the product of the reduced frequency and the square of the Mach number (i.e. $\Delta P/P \; \alpha \; \omega_R^* \cdot M^2$). For the low Mach number flow in a gas turbine combustor (say, less than 0.1), pressure changes due to inertial effects should be small compared to those due to compliance effects ("global" mass storage). Furthermore, acoustic disturbances should not be important provided the reduced frequency based on relevant combustor dimensions is small.

Another assumption is that the total pressure through the combustor is uniform from compressor duct exit to the turbine inlet. Burner total pressure losses due to both frictional and heat addition effects scale with the square of the Mach number and thus should be small. Other relevant assumptions made in the modelling of the combustor dynamics are:

- The volumetric averaged burner temperature is well approximated by the turbine inlet temperature (similarly, for the burner density)
- The thermodynamic properties of the combustion products are approximately the same as those of air (at the same conditions)
- The mass of fuel injected is negligible ($\dot{m}_F \approx \frac{1}{50} \cdot \dot{m}_C$)

Provided the modelling assumptions are valid, the combustor dynamics should be governed by global compliance effects. Both the mass and energy conservation equations are required to model the combustor dynamics . The control volume form of the mass conservation equation for the combustor is given as

$$\frac{d\tilde{\rho}_B}{dt} \cdot V_B = \dot{m}_C - \dot{m}_T \qquad (2.17)$$

where, $\tilde{\rho}_B$ is the volumetric average burner density. The conservation of energy equation is given as

$$\frac{d(c_V \cdot \tilde{\rho}_B \cdot \tilde{T}_B)}{dt} \cdot V_B = \dot{m}_C \cdot c_P T_{O,4} - \dot{m}_T \cdot c_P T_{O,5} + \dot{Q} \qquad (2.18)$$

where, $\dot{Q}$ is the instantaneous heat-release rate due to the combustion of fuel.

In practice, the instantaneous heat-release rate is a function of many variables: pressure, temperature, air flow rate, geometry, etc. In this analysis, $\dot{Q}$ is expressed as a function of the fuel-flow rate, $\dot{m}_F$, the lower heating value of the fuel, HV, and the combustion efficiency, η_B, as

$$\dot{Q} = \eta_B \cdot \dot{m}_F \cdot HV \qquad (2.19)$$

The time scales associated with the fuel control dynamics are long, compared to the linear surge inception oscillations, which means that the fuel-flow rate is essentially constant.

Also since the combustion efficiency is near unity, the effect of perturbations in $\dot{Q}$, due to fluctuations in η_B, on the combustor dynamics are assumed small compared to the effects of global mass and enthalpy imbalances. Thus the analysis presented in this chapter only assesses the effect of steady-state heat addition on open-loop engine stability. The effect of unsteady heat-release is considered in Chapter 3 when fuel-flow modulation is evaluated as an active surge control strategy.

Due to the heat-release in the combustor, assumptions about the distribution of temperature (and density) must be made. Herein the volumetric averaged temperature, $\tilde{T}_B$, is approximated by the turbine inlet temperature; however it is noted that this is not a critical assumption of the analysis and is rationalized by typical combustor temperature distributions.

Turbine/Exhaust Nozzle:

The high pressure fluid in the combustion chamber discharges to atmosphere by first passing through a gas generator turbine and then an exhaust nozzle or power turbine. The approach taken in this study is to model the turbine as a quasi-steady choked nozzle. This is a simplication of the complex flowfield in the turbine and nozzle which, if valid, offers several advantages. First, the choking of the turbine decouples the downstream dynamics from the rest of the compression system. Second, the one-dimensional nozzle flow assumption allows the use of algebraic equations instead of turbine performance maps.

The quasi-steady assumption is valid provided that the reduced frequency based on characteristic turbine conditions is much less than unity (see Eqn. 2.2). The other major assumption is that the turbine performance is well represented by one-dimensional compressible nozzle flow, independent of rotor speed. This approximation is common to steady-state engine matching calculations [29, 30] and is equivalent to assuming that the turbine's first-stage guide vanes choke before the downstream vanes or rotors. This is

illustrated in Fig. 2.2 which shows turbine performance maps for a NASA single-stage turbine [31]. Figure 2.2(a) is a turbine with choked first-stage guide vanes and illustrates three relevant points: (1) the performance resembles that of a one-dimensional compressible nozzle flow, (2) the performance is nearly independent of speed and (3) the turbine is choked for pressure ratios above two. Figure 2.2(b) illustrates that this simple model is not valid if a downstream blade-row chokes instead of the first-stage vanes. Fortunately many high performance turbines do have choked first-stage vanes which allows this modelling approach to be used.

From a system viewpoint, the turbine affects the dynamics through fluctuations in mass flow out of the combustion chamber. From the continuity equation for a steady, one-dimensional, compressible flow [32], the turbine mass flow can be expressed as a function of inlet total pressure, total temperature, nozzle throat area and Mach number. For a choked turbine the continuity equation reduces to

$$\frac{\dot{m}_T \cdot \sqrt{R \cdot T_B}}{P_B \cdot A_T} = \sqrt{\gamma} \cdot \left(\frac{2}{\gamma+1}\right)^{\frac{\gamma+1}{2(\gamma-1)}} = F(\gamma) \qquad (2.20)$$

where, $F(\gamma)$ is the function of specific heat ratio on the right hand side of the equation.

Simplification of the Equations for Negligible Internal Compressor Compliance:

The earlier assumption that the compressor internal compliance is negligible (Eqn. 2.12) allows the compressor duct momentum equations (Eqns. 2.6 and 2.8) to be combined into a single equation. In this situation not only are the upstream and downstream mass flows equivalent ($\dot{m}_u = \dot{m}_d = \dot{m}_C$), but also the rates of change of mass flow (similarly, $\frac{d\dot{m}_u}{dt} = \frac{d\dot{m}_d}{dt} = \frac{d\dot{m}_C}{dt}$). This allows the two momentum equations to be combined by first solving Eqn. 2.6 for the total pressure at the compressor face, $P_{O,2}$, (using $P_{O,1} \cong P_a$)

$$P_{O,2} = P_a - \left(\frac{L_u}{A_C}\right) \cdot \frac{d\dot{m}_C}{dt} \qquad (2.21)$$

and then substituting this expression into Eqn. 2.8 to yield a single conservation of momentum equation for the entire compressor duct (using $P_{0,4} \cong P_B$)

$$\left(\frac{L_d}{A_C} + \pi_C \cdot \frac{L_u}{A_C}\right) \cdot \frac{d\dot{m}_C}{dt} = \pi_C \cdot P_a - P_B \qquad (2.22)$$

Equation 2.22 along with the burner mass and energy conservation equations (Eqns. 2.17 and 2.18) and the compressor and turbine characteristics (Eqns. 2.13 and 2.14) are used to model the surge dynamics of the gas turbine engine.

2.2.3 Non-Dimensionalization of the Governing Equations

Consistent with the pressure ratio respresentation of the compressor performance, mass flows are non-dimensionalized in a manner analogous to the corrected flow in Eqn. 2.15 using P_a, T_a and A_C as the reference quantities. The non-dimensional compressor and turbine mass flows, W_C and W_T, are thus defined as:

$$W_C \equiv \frac{\dot{m}_C \cdot \sqrt{R \cdot T_a}}{P_a \cdot A_C} \quad (2.23) \qquad \text{and} \qquad W_T \equiv \frac{\dot{m}_T \cdot \sqrt{R \cdot T_a}}{P_a \cdot A_C} \quad (2.24)$$

Pressure and temperature ratios, P^* and T^*, are formed using the ambient pressure and temperature as

$$P^* \equiv \frac{P}{P_a} \quad (2.25) \qquad \text{and} \qquad T^* \equiv \frac{T}{T_a} \quad (2.26)$$

A non-dimensional time, τ, is formed using the Helmholtz resonator frequency, ω_H,

$$\tau \equiv \omega_H \cdot t \qquad (2.27)$$

where, ω_H is a characteristic time scale of linear surge oscillations, defined as

$$\omega_H \equiv \bar{a}_B \sqrt{\frac{A_C}{(L_u + L_d) \cdot V_B}} \qquad (2.28)$$

The Helmholtz frequency is basically the resonant frequency of a lumped parameter duct/plenum system with no damping elements [33]. Lastly, the rotor tip speed is non-dimensionalized as in a manner analogous to the tip Mach number (Eqn. 2.16)

$$M_{tip,a} \equiv \frac{U_{tip}}{\sqrt{\gamma \cdot R \cdot T_a}} \qquad (2.29)$$

The resulting non-dimensional momentum, mass and energy conservation equations are:

(Momentum Conservation)
$$\frac{dW_C}{d\tau} = \beta \cdot \frac{\left(\frac{L_u}{L_d} + 1\right)}{\left(\pi_C \cdot \frac{L_u}{L_d} + 1\right)} \cdot \left(\pi_C - P_B^*\right) \qquad (2.30)$$

(Mass Conservation)
$$\frac{d\rho_B^*}{d\tau} = \frac{1}{\gamma \cdot \overline{T}_B^* \cdot \beta} \cdot \left(W_C - W_T\right) \qquad (2.31)$$

(Energy Conservation)
$$\frac{dP_B^*}{d\tau} = \frac{1}{\overline{T}_B^* \cdot \beta} \cdot \left(W_C \cdot T_{O,4}^* - W_T \cdot T_B^*\right) + \dot{Q}^* \qquad (2.32)$$

where, β and L_u/L_d are non-dimensional similarity parameters.

The *stability parameter*, β, is important because it has a strong influence on the system damping. It is defined as:

$$\beta \equiv \frac{1}{\sqrt{\gamma \cdot \overline{T}_B^*}} \cdot \sqrt{\frac{V_B}{(L_u + L_d) \cdot A_C}} \qquad (2.33)$$

It is analogous to the B parameter of Reference 13 and is related as follows

$$\beta = \frac{2 \cdot B}{\sqrt{\gamma} \cdot \overline{M}_{tip,a}} \qquad (2.34)$$

A useful interpretation of the stability parameter is that it is a measure of the degree of dynamic coupling between the compressor and turbine. For small β, the turbine (the unsteady energy sink) is close-coupled to the compressor (the unsteady energy source), yielding a more stable system which can tolerate some finite positive compressor slope. For large β, the turbine is dynamically decoupled from the compressor, yielding a less stable system which can not tolerate any positive value of compressor slope.

The *inertia ratio*, L_u/L_d, is a measure of the relative amount of flow inertia upstream of the compressor compared to the amount of inertia downstream. This parameter becomes important when upstream inertia is allowed to affect the compressor performance, as discussed later in the chapter. Equation 2.30 also shows that the compressor pressure ratio has a "weighting" effect on the inertia ratio, making it a more important parameter at large pressure ratios.

The non-dimensional compressor and turbine characteristics also must be specified. The compressor characteristics are given in functional form by Eqns. 2.13 and 2.14, which are rewritten here for convenience

$$\pi_C = \pi_C(W_{C,COR}, M_{tip,2}) \tag{2.13}$$

$$\theta_C = \theta_C(W_{C,COR}, M_{tip,2}) \tag{2.14}$$

The compressor corrected flow and tip Mach number can be expressed as functions of the system non-dimensional variables as

$$W_{C,COR} = \frac{W_C \cdot \sqrt{T^*_{O,2}}}{P^*_{O,2}} \quad (2.35) \qquad \text{and} \qquad M_{tip,2} \equiv \frac{M_{tip,a}}{\sqrt{T^*_{O,2}}} \quad (2.36)$$

Thus the compressor corrected flow, $W_{C,COR}$, is not only a function of the non-dimensional mass flow, W_C, but also the total pressure and total temperature at the compressor inlet. Similarly, the compressor tip Mach number, $M_{tip,2}$, is a function of both the non-dimensional rotor tip speed, $M_{tip,a}$ (which is initially assumed constant), and $T^*_{O,2}$. Perturbations in $P^*_{O,2}$ and $T^*_{O,2}$ due to upstream flow inertia can thus affect the compressor performance. The perturbations in $P^*_{O,2}$ caused by upstream inertial effects are estimated from the momentum equation for the flow in the upstream duct (Eqn. 2.21),

$$P^*_{O,2} = 1 - \frac{1}{\left(1 + \frac{L_d}{L_u}\right) \cdot \beta} \cdot \frac{dWc}{d\tau} \tag{2.37}$$

The perturbations in $T^*_{O,2}$ are estimated from the non-dimensional form of Eqn. 2.10,

$$T^*_{O,2} = \left(P^*_{O,2}\right)^{\frac{\gamma-1}{\gamma}} \tag{2.38}$$

The non-dimensional turbine mass flow is expressed, after some manipulation, as a function of the burner pressure and density as

$$W_T = \frac{\overline{W}_T \cdot \sqrt{\overline{T}^*_B}}{\overline{P}^*_B} \cdot \sqrt{P^*_B \cdot \rho^*_B} \tag{2.39}$$

The non-dimensional equations governing the engine surge dynamics can be assembled and written in the following functional form

(Conservation of Momentum) $$\frac{dW_C}{d\tau} = F_1\left(W_C, P^*_B, \frac{dW_C}{d\tau}\right) \tag{2.40}$$

(Conservation of Mass) $$\frac{d\rho_B^*}{d\tau} = F_2\left(W_C, \rho_B^*, P_B^*\right) \tag{2.41}$$

(Conservation of Energy) $$\frac{dP_B^*}{d\tau} = F_3\left(W_C, \rho_B^*, P_B^*, \frac{dW_C}{d\tau}\right) \tag{2.42}$$

These are three coupled, first order, non-linear ordinary differential equations which are not only non-linear functions of the state variables W_C, ρ_B^* and P_B^*, but also the time derivative, $\frac{dW_C}{d\tau}$ (due to upsteam inertial affects). The non-linear solution to these equations can be found by numerical integration techniques, but the emphasis here is system stability. Thus, Equations 2.40, 2.41 and 2.42 are linearized about an operating point to evaluate the stability of the system to small perturbations.

2.3 Linear Stability Analysis

2.3.1 Method

To study the stability of equilibrium operating points to small amplitude disturbances, the system of equations are linearized. The linearization is somewhat involved because of non-linearities in the time derivative of mass flow and the reader is referred to Appendix B for the details. Here we will only describe the method; it should suffice to show the general matrix form of the open-loop, 3rd-order linear system,

$$\frac{d}{d\tau}\begin{pmatrix}\hat{W}_C\\ \hat{\rho}_B^*\\ \hat{P}_B^*\end{pmatrix} = \begin{bmatrix}a_{11} & a_{12} & a_{13}\\ a_{21} & a_{22} & a_{23}\\ a_{31} & a_{32} & a_{33}\end{bmatrix}\cdot\begin{pmatrix}\hat{W}_C\\ \hat{\rho}_B^*\\ \hat{P}_B^*\end{pmatrix} = [A]\cdot\begin{pmatrix}\hat{W}_C\\ \hat{\rho}_B^*\\ \hat{P}_B^*\end{pmatrix} \tag{2.43}$$

and say that the stability of a given operating point is evaluated from the eigenvalues of the **A** matrix for the specified values of the compression system parameters.

System stability is dependent on the stability parameter, β, the inertia ratio, L_u/L_d, the slope of the compressor pressure ratio versus corrected flow characteristic,

$$\overline{m}_C \equiv \left(\overline{\frac{\partial(\pi_C)}{\partial(W_{C,COR})}}\right) = \overline{m}_C(\overline{W}_{C,COR}, \overline{M}_{tip,2})$$

as well as the following additional parameters: $\overline{\pi}_C$, $\overline{W}_{C,COR}$, $\overline{M}_{tip,2}$, $\left(\overline{\frac{\partial(\pi_C)}{\partial(M_{tip,2})}}\right)$, $\overline{\theta}_C$, $\left(\overline{\frac{\partial(\theta_C)}{\partial(W_{C,COR})}}\right)$, $\left(\overline{\frac{\partial(\theta_C)}{\partial(M_{tip,2})}}\right)$, $\left(\overline{\frac{\partial(W_T)}{\partial(\rho_B^*)}}\right)$, $\left(\overline{\frac{\partial(W_T)}{\partial(P_B^*)}}\right)$ and $\overline{T}_B^*$ which also must be specified at the

given operating point. Stability is assessed for a range of parameter values to model a variety of compressions systems in geometry and performance.

The values of β and L_u/L_d are basically set by the geometry of the compression system (in addition to $\overline{T}_B^*$). To model systems with a variety of plenum chamber-to-compressor duct volume ratios, values for β of 0.25, 0.5 and 1 are chosen. To assess the effect of fluid inertia upstream of the compressor, values of L_u/L_d ranging from 0.01 to 100 are examined.

Several compressor characteristics (speed lines) are used to cover a range of pressure ratios, temperature ratios, corrected flows, and tip Mach numbers. Table 2.1 presents the four cases that were chosen. The parameters $\pi_{C,peak}$, $\theta_{C,peak}$ and $(W_{C,COR})_{peak}$ are the pressure ratio, temperature ratio and corrected flow, respectively, at the peak of the constant speed characteristic. The peak pressure ratios selected were 2.5, 5, 7.5 and 10. The corresponding values of the peak temperature ratios were calculated using an assumed compressor efficiency of 0.80.

Speedline No.	1	2	3	4
$\pi_{C,peak}$	2.5	5	7.5	10
$\theta_{C,peak}$	1.37	1.73	1.97	2.16
$(W_{C,COR})_{peak}$	0.20	0.33	0.43	0.50
$M_{tip,2}$	0.97	1.35	1.56	1.71

Table 2.1: Compressor Performance Parameters for Stability Analysis

In the comparison of compressors operating at different pressure ratios, each of the four pressure ratio--corrected flow speed lines are generated by scaling from a single "scaled" compressor characteristic. The main purpose of the compressor speedline is to specify the slope, $\overline{m}_C$, as a function of the flow, $\overline{W}_{C,COR}$. Because linear stability is a

much stronger function of compressor slope than mean flow the shape of the compressor characteristic is not crucial . The "scaled" compressor characteristic used in this study, shown in Fig. 2.3, was derived from information on the engines of interest. The pressure ratio--flow characteristic is shown in Fig. 2.3(a) and and the slope--flow relationship in Fig. 2.3(b). The shape of the characteristic covers the full range of compressor slopes, from large positive values at the low flow end to large negative values at the high flow end.

The compressor temperature ratio characteristics (Eqn. 2.14) are specified as linear functions of corrected flow, at constant speed. The temperature slope, $m_{C,\theta}$, defined as $\left(\overline{\frac{\partial(\theta_C)}{\partial(W_{C,COR})}}\right)$ is given values ranging from 0 to -1 to represent compressors with different blade geometries ($m_{C,\theta}$ has negative values for both axial and radial or backward swept centrifugal impellers).

The sensitivity of the compressor pressure and temperature ratios to changes in rotor tip Mach number, $\left(\overline{\frac{\partial(\pi_C)}{\partial(M_{tip,2})}}\right)$ and $\left(\overline{\frac{\partial(\theta_C)}{\partial(M_{tip,2})}}\right)$ are specified using the following approach. First, the pressure and temperature ratio are expressed as functions of the rotor tip Mach number, adiabatic efficiency, η_C, and work coefficient, μ_C (defined as $\Delta h_{O,C}/U_{tip}^2$), as follows

$$\pi_C = \left[1+\eta_C\cdot(\gamma-1)\cdot\mu_C\cdot M_{tip,2}^2\right]^{\frac{\gamma}{\gamma-1}} \tag{2.44}$$

$$\theta_C = 1+(\gamma-1)\cdot\mu_C\cdot M_{tip,2}^2 \tag{2.45}$$

The sensitivities to changes in tip Mach number are then estimated by differentiating Eqns. 2.44 and 2.45 assuming that changes in η_C and μ_C are small compared to changes in π_C and θ_C, as:

$$\left(\overline{\frac{\partial(\pi_C)}{\partial(M_{tip,2})}}\right) \cong 2\gamma\cdot\overline{M}_{tip,2}\cdot\overline{\eta}_C\cdot\overline{\mu}_C\cdot\left[1+\overline{\eta}_C\cdot\overline{\mu}_C(\gamma-1)\cdot\overline{M}_{tip,2}^2\right]^{\frac{1}{\gamma-1}} \tag{2.46}$$

$$\left(\overline{\frac{\partial(\theta_C)}{\partial(M_{tip,2})}}\right) \cong 2\cdot(\gamma-1)\cdot\overline{M}_{tip,2}^2\cdot\overline{\mu}_C \tag{2.47}$$

Values for $\overline{\eta}_C$ of 0.80 and $\overline{\mu}_C$ of 1 are chosen to model a radial-bladed centrifugal compressor which is representative of the engines of interest.

The turbine mass flow sensitivities also must be specified. From the expression for the turbine mass flow (Eqn. 2.39), these parameters are estimated as

$$\left(\frac{\overline{\partial(W_T)}}{\partial(\rho_B^*)}\right) = \frac{\overline{W}_T \cdot \overline{T}_B^*}{2 \cdot \overline{P}_B^*} \quad (2.48) \qquad \text{and} \qquad \left(\frac{\overline{\partial(W_T)}}{\partial(P_B^*)}\right) = \frac{\overline{W}_T}{2 \cdot \overline{P}_B^*} \quad (2.49)$$

Lastly, the burner temperature, $\overline{T}_B^*$, is known once the burner temperature ratio, θ_B (defined as $\overline{T}_B/\overline{T}_{O,4}$), is specified. θ_B is a measure of the amount of steady-state heat addition in the burner. Values of θ_B ranging from 1 (no steady heat addition) to 2 are used.

The method used to arrive at the stability limit of the compression system is as follows. The compressor characteristic is discretized into equal increments in mass flow, giving $\overline{m}_C$ and $\overline{\pi}_C$ at each flow. The stability limit is found by checking the eigenvalues at each operating point, starting at the high flow end and marching toward the lower flows, until the first eigenvalue with zero real part is found. This operating point is the neutral stability point, any further reduction in flow results in system instability. The compressor slope, $\overline{m}_{C,NS}$, and normalized surge frequency, ω_{NS}^* (defined as ω_{NS}/ω_H) at neutral stability characterize the stability point of the system. The slope is a measure of the amount of compressor energy production the system can tolerate before it goes unstable, with higher values of $\overline{m}_{C,NS}$ indicating a more stable system. The frequency is a measure of the time scale of the oscillatory surge inception growth which is a relevant issue in the study of dynamic control strategies where actuator bandwidth is important.

2.3.2 Results

The results of the analysis are given in Figs. 2.4 through 2.9 for the compression system parameters specified in the previous section. The results are discussed as they are presented.

Results for a compression system with a stability parameter, β, of 0.25, a burner temperature ratio, θ_B, of 2, and a temperature slope, $m_{C,\theta}$, of -0.5 are given in Fig. 2.4. These values were chosen to represent an helicopter engine with a small burner-to-compressor duct volume ratio (i.e. small value of β). Figure 2.4(a) shows the dependence of the compressor slope at neutral stability, $\overline{m}_{C,NS}$, on the inertia ratio, L_u/L_d, plotted on a base 10 log scale, for the four curves representing the compressor speedlines in Table 2.1. From this figure the following trends are observed:

- For inertia ratios less than about 0.25, lower pressure ratio compression systems are more stable than those with higher pressure ratio
- For inertia ratios greater than about 0.35, the higher pressure ratio compression systems are more stable than those with lower pressure ratios
- For all the compression systems, increasing the inertia ratio has a stabilizing influence with the effect more prevalent for the higher pressure ratio systems

The first trend is explained from the method used to scale the individual compressor characteristics . If all the speedlines collapse onto a single curve when scaled as done in Fig. 2.3, the effective stability parameter, β_{eff}, is actually $\frac{\beta \cdot \pi_{C,peak}}{\left(W_{C,COR}\right)_{peak}}$ instead of β. In this situation the lower pressure ratio compression systems have smaller values of β_{eff}, which makes them more stable than the higher pressure ratio systems. This trend may or may not be observed for other compressor characteristics depending upon the degree of validity of the scaling relationship used in this study.

The second and third trends given above are related to the stabilizing influence of upstream inertia. A qualitative explanation of this phenomena is given based on total pressure perturbations due to flow inertia being 90° out of phase with mass flow perturbations. The perturbations in $P_{O,2}$ (due to upstream inertia effects) are approximately amplified, by a factor of the pressure ratio, across the compressor. Amplification at the compressor exit of the portion of total pressure that is 90° out of

phase with the mass flow effectively acts as an increase in fluid inertia, which has a stabilizing influence since the system is more resistant to accelerations. Effective inertia is thus increased by either placing more inertia upstream of the compressor (by moving the compressor toward the end of the duct) or increasing the compressor pressure ratio.

The stabilizing influence of upstream inertia is related to the effect that density perturbations at the compressor inlet have on unsteady compressor performance. A strictly incompressible surge model does not capture this effect.

Figure 2.4(b) shows the dependence of the normalized surge frequency at neutral stability, ω^*_{NS}, on the inertia ratio for the four curves representing the compressor speedlines in Table 2.1. Three trends are observed:

- Increasing the inertia ratio tends to decrease the surge frequency for all the compression systems
- The higher pressure ratio systems tend to have lower surge frequencies (at a given L_u/L_d) than the lower pressure ratio systems
- For all the compressor speedlines and inertia ratios the surge frequency is less than the system Helmholtz frequency

The first two trends are also explained by the increase in effective inertia discussed above. As the effective inertia of the system is increased, due to an increase in either the inertia ratio or compressor pressure ratio, the surge frequency decreases.

In Figures 2.5 and 2.6 the stability parameter, β, of the compression system is increased to values of 0.5 and 1.0, respectively, while holding the same values of θ_B and $m_{C,\theta}$. A comparison of Figs. 2.4(a), 2.5(a) and 2.6(a) reveals the strong decrease in system stability as β is increased. The trends in $\overline{m}_{C,NS}$ with L_u/L_d and compressor performance level are essentially unchanged. The reduction in stability occurs because the system damping decreases as β is increased. The system is more compliant at high β which acts to dynamically decouple the turbine and compressor. A comparison of Figs. 2.4(b), 2.5(b) and 2.6(b) shows that the normalized surge surge frequency is not affected

much by the increase in β. Eventhough the increase in β causes a strong reduction in system damping, this has a small affect on the normalized system frequency as would be expected.

Variations in the temperature slope, $m_{C,\theta}$, and burner temperature ratio, θ_B, are presented in Figs. 2.7 through 2.9 to determine their effect on engine stability. The results are given for a compression system with β=0.5 and the compressor speedline with $\pi_{C,peak}$=7.5. In Figure 2.7 parameter sweeps on the burner temperature ratio are performed while holding $m_{C,\theta}$ at -0.5 with the three curves corresponding to values of θ_B of 1, 1.5 and 2. Figure 2.7(a) clearly shows the destabilizing influence of steady heat addition. The slope at neutral stability is reduced by roughly 30 percent for all values of the inertia ratio as θ_B is increased from 1 to 2. Figure 2.7(b) shows the effect of steady heat addition on the surge frequency. As θ_B is increased from 1 to 2, ω^*_{NS} is decreased by approximately 30 percent for the entire range of inertia ratios.

Figures 2.8 and 2.9 show parameter sweeps on the compressor temperature slope while holding θ_B fixed at values of 1 and 2, respectively. Figure 2.8(a) shows the destabilizing influence of decreasing $m_{C,\theta}$ below 0 for no steady heat addition (θ_B =1). For values of L_u/L_d above 1, $\overline{m}_{C,NS}$ is reduced by over 30 percent as $m_{C,\theta}$ is decreased from 0 to -1. In Figure 2.8(b) the decrease in surge frequency with $m_{C,\theta}$ is observed with ω^*_{NS} being reduced by roughly 10 percent for all inertia ratios as $m_{C,\theta}$ is decreased from 0 to -1. Basically the same trends with $m_{C,\theta}$ are observed in Fig. 2.9 although the mean levels of $\overline{m}_{C,NS}$ and ω^*_{NS} are shifted due to the effect of the steady heat addition (θ_B =2).

2.3.3 Isentropic Plenum Process Assumption

The validity of the isentropic plenum process assumption typical of many previous compression system surge models is now examined for a gas turbine engine. Comparison of these results to those of the previous section allows the importance of non-isentropic processes in the burner to be assessed.

2.3.3 (a) Modelling

The essence of the isentropic process assumption is that combustor pressure is isentropically related to combustor density. For a perfect gas this is given as,

$$\frac{P_B}{\rho_B^\gamma} = \text{constant} \qquad (2.50) \qquad \text{or} \qquad \frac{dP_B}{dt} = \bar{a}_B^2 \cdot \frac{d\rho_B}{dt} \qquad (2.51)$$

The benefit of this approximation is that the conservation of energy equation is no longer needed to model the thermodynamic process in the burner. Equation 2.51 above is used to express the mass conservation equation in terms of the burner pressure (in non-dimensional form) as

$$\frac{dP_B^*}{d\tau} = \frac{1}{\beta} \cdot (W_C - W_T) \qquad (2.52)$$

The expression for the turbine mass flow (Eqn. 2.39) can also be simplified using Eqn. 2.50 to relate the burner pressure and temperature. After some manipulation, the non-dimensional turbine mass flow is written as a function of only burner pressure as

$$W_T = \overline{W}_T \cdot \left(\frac{P_B^*}{\overline{P}_B^*} \right)^{\frac{\gamma+1}{2\cdot\gamma}} \qquad (2.53)$$

An additional advantage of the isentropic plenum process assumption is that the compressor temperature ratio characteristic is no longer needed.

2.3.3 (b) Results

Figures 2.10 through 2.12 compare the results of the isentropic assumption (the solid lines in these three figures) to those previously presented in Figs. 2.7 through 2.9. In Figure 2.10 the effect of steady heat addition on the validity of the isentropic process approximation, for a representative value of $m_{C,\theta}$ (=-0.5), is examined. As expected, increasing θ_B causes the non-isentropic processes in the burner to become more important. The isentropic model captures the qualitative trends with inertia ratio, but for a burner temperature ratio of 2 the quantitative agreement is not good. For values of the surge model parameters representative of a helicopter engine, namely, β=0.5, $\pi_{C,peak}$=7.5,

$m_{C,\theta}$=-0.5 and θ_B=2, the isentropic model predicts a more stable system by upto 35 percent in $\overline{m}_{C,NS}$ and overpredicts the surge frequency by roughly 35 percent.

Figure 2.11 illustrates the effect of variations of the compressor temperature slope on the validity of the isentropic plenum process assumption for no steady heat addition (θ_B=1). In Figure 2.11(a) the isentropic process model shows good aggreement in the prediction of $\overline{m}_{C,NS}$ for values of $m_{C,\theta}$ between 0 and -0.5. However for $m_{C,\theta}$=-1 and inertia ratios greater than 1, the aggreement is not as good, with the isentropic model predicting a more stable system by almost 30 percent in $\overline{m}_{C,NS}$. Figure 2.11(b) shows that the isentropic model slightly overestimates the surge frequency by no more than 10 percent (for $m_{C,\theta}$=-1). Thus for no steady heat addition in the plenum, the isentropic assumption does a fairly good job for temperature slopes with values between 0 and -0.5.

The influence of parametric variations in $m_{C,\theta}$ for steady heat addition (θ_B=2) are illustrated in Figure 2.12. The isentropic model shows only fair quantiative agreement for all values of the temperature slope. As one might expect, the burner behaves less as an isentropic plenum as $m_{C,\theta}$ is decreased away from zero due to the increase in enthalpy fluctuations.

Several conclusions can be drawn from the above results. For compressor test rigs with no steady heat addition in the plenum and temperature slopes no less than -0.5, the isentropic process assumption shows good quantitative agreement with the gas turbine engine model with non-isentropic effects. For temperature slopes less than -0.5 the isentropic assumption becomes worse and captures only qualitative trends in $\overline{m}_{C,NS}$ and ω^*_{NS}. For gas turbine engines with steady heat addition corresponding to burner temperature ratios of roughly 2, the isentropic process assumption shows only fair quantitative agreement with the engine surge model, although it does capture qualitative trends. Thus the simpler isentropic burner process assumption provides rough estimates of the compressor slope and surge frequency for a gas turbine engine, but for detailed studies the extra effort should be expended to include the non-isentropic effects.

2.3.4 Constant Rotor Speed Assumption

The surge model with the isentropic plenum process assumption is now extended to include the rotor dynamics associated with the mechanical coupling of the compressor and turbine via a common shaft. As discussed in Chapter 1, the turbocharger surge analysis by Fink [14] showed that rotor speed fluctuations have a negligible effect on linear stability for practical values of the turbospool inertia. Due to the larger rotor inertias expected in a helicopter engine, rotor dynamics should not be important. However the model developed herein includes phenomena not dealt with by previous models, so rotor dynamics are examined to insure that they have a negligible effect on engine stability.

2.3.4 (a) Modelling

In steady operation the engine rotor speed is held constant by a balance of power (or torque) between the turbine and compressor. During surge this balance of power is upset and the rotor accelerates or decelerates. The following assumptions are made in modelling the rotor dynamics:

- The torques due to frictional forces are small
- No auxiliary power is drawn from the turbine
- The turbine temperature ratio, θ_T, (total-to-total) is constant during the surge inception process

Using the above assumptions, the conservation of angular momentum equation for the compressor/turbine spool, written in terms of torques, is

$$J \cdot \frac{d\Omega}{dt} = \Gamma_T - \Gamma_C \qquad (2.54)$$

This equation is written in a more convenient form by expressing the turbine and compressor torques in terms of power

$$J \cdot \frac{d\Omega}{dt} = \frac{1}{\Omega} \cdot \left[\dot{m}_T \cdot c_P T_{O,5} \cdot (1 - \theta_T) - \dot{m}_C \cdot c_P T_{O,2} \cdot (\theta_C - 1) \right] \qquad (2.55)$$

Provided the turbine and exhaust nozzle remain choked during surge inception, one can show that the turbine temperature ratio (total-to-total) remains constant at its steady-state value to a good approximation (see Ref. 34 for a discussion of this assumption for steady flow conditions). The non-dimensional form of the angular momentum equation is given as

$$\frac{dM_{tip,a}}{d\tau} = \frac{\beta}{M_{tip,a} \cdot J^*} \cdot \left[W_T \cdot T_B^* \cdot (1 - \bar{\theta}_T) - W_C \cdot T_{O,2}^* \cdot (\theta_C - 1) \right] \qquad (2.56)$$

where, J^* is the non-dimensional *rotor inertia parameter*, defined as

$$J^* \equiv \frac{J \cdot (\gamma - 1)}{R_{tip}^2 \cdot \rho_a \cdot (L_u + L_d) \cdot A_C} \qquad (2.57)$$

A representative value of J^* for a small helicopter gas turbine is on the order of 100; for larger turbofan engines the value of J^* would be higher.

2.3.4 (b) Results

The results of the linear stability analysis with compressor/turbine shaft dynamics are given in Figures 2.13 through 2.15 for values of J^* ranging from 1 to 1000. Figure 2.13 presents the results for a compression system with a stability parameter, β, of 0.5 an inertia ratio, L_u/L_d, of 1, a temperature slope, $m_{C,\theta}$, of -0.5 and a burner temperature ratio, θ_B, of 2. In Figure 2.13(a) the compressor slope at neutral stability, $\overline{m}_{C,NS}$, is given as a function of J^*(plotted on a base 10 log scale) for the four curves representing the compressor speedlines in Table 2.1. As expected, for large values of J^* (say, greater than about 30) the four curves asymptote to the constant rotor speed solution. For smaller values of J^* (on the order 10 or less), the shaft dynamics have a stabilizing influence with the affect becoming stronger for the higher pressure ratio compression systems.

Similar trends are observed in Figure 2.13(b) which is a plot of the normalized surge frequency at neutral stability, ω_{NS}^*, as a function of the rotor inertia parameter (on a base 10 log scale) for the 4 different compressor speedlines. Once again, for large values of J^* (greater than about 30) all four curves asymptote to their constant rotor speed

solution. For smaller values of J^* (again on the order of 10 or less), the shaft dynamics tend to increase the surge frequency with the effect becoming stronger for the high pressure ratio compression systems.

Figures 2.14 and 2.15 show the results for inertia ratios of 0.01 and 100, respectively, holding the same values of β, $m_{C,\theta}$ and θ_B. For these inertia ratios the same general trends are observed. Similar results were also found for values of β of 0.25 and 1 although not shown here.

Since the expected values of J^* are of the order of 100 or greater, rotor speed fluctuations should have a negligible influence on gas turbine engine stability. However for large amplitude post surge inception studies, Fink [14] has shown that rotor speed fluctuations are important and should be modelled.

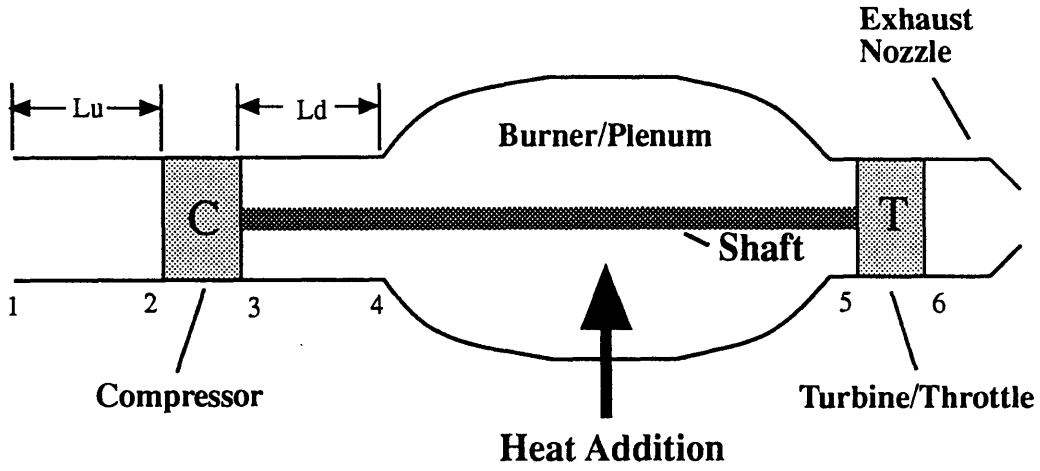

Figure 2.1: Schematic of Gas Turbine Engine Surge Model.

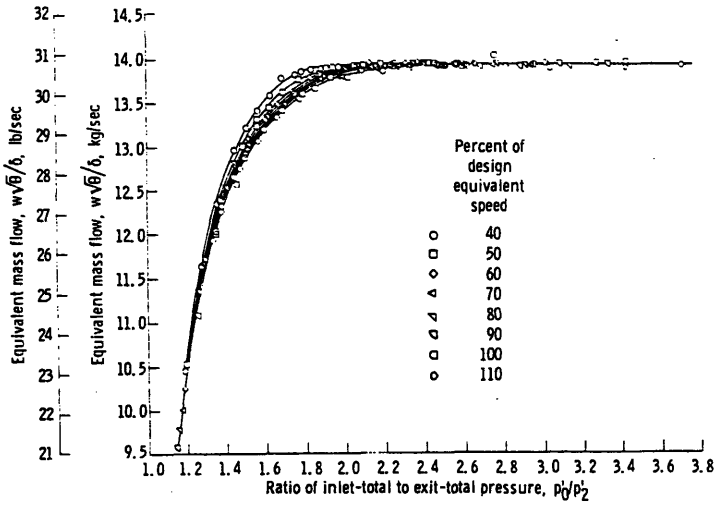

(a)

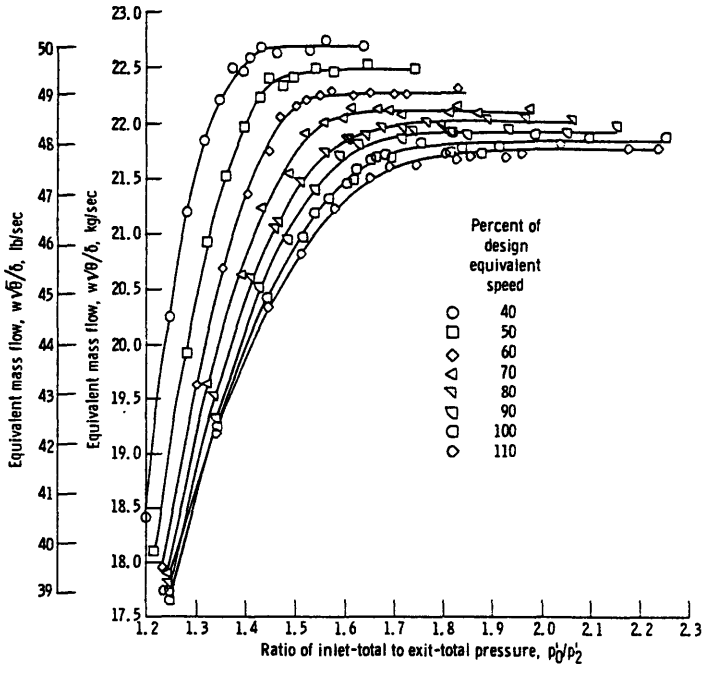

(b)

Figure 2.2: Single-Stage Turbine Performance Characteristics for (a) Choking in Nozzle Guide Vanes and (b) Choking in Rotor Blades (from [31]).

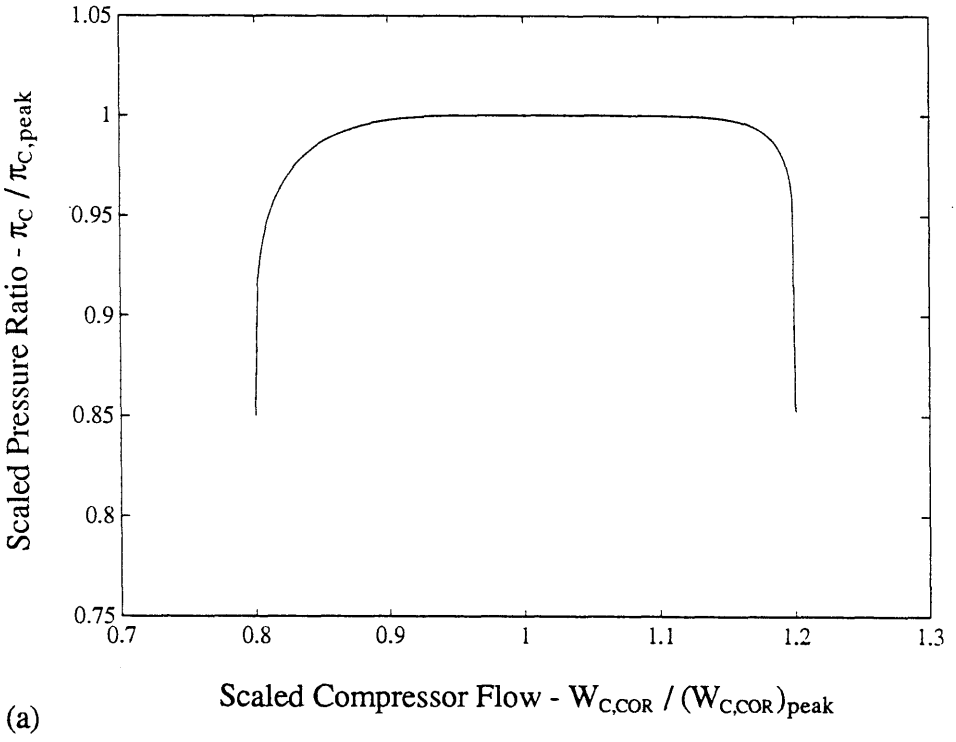

(a)

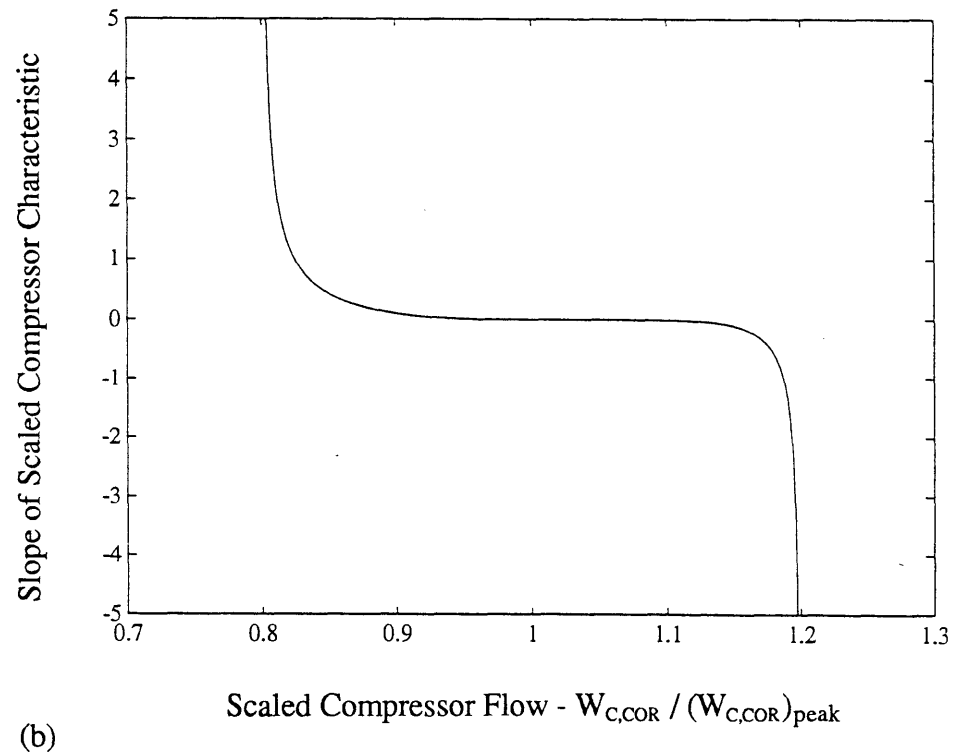

(b)

Figure 2.3: "Scaled" Compressor Characteristics used in Linear Stability Analysis: (a) Pressure Ratio verses Flow and (b) Slope verses Flow.

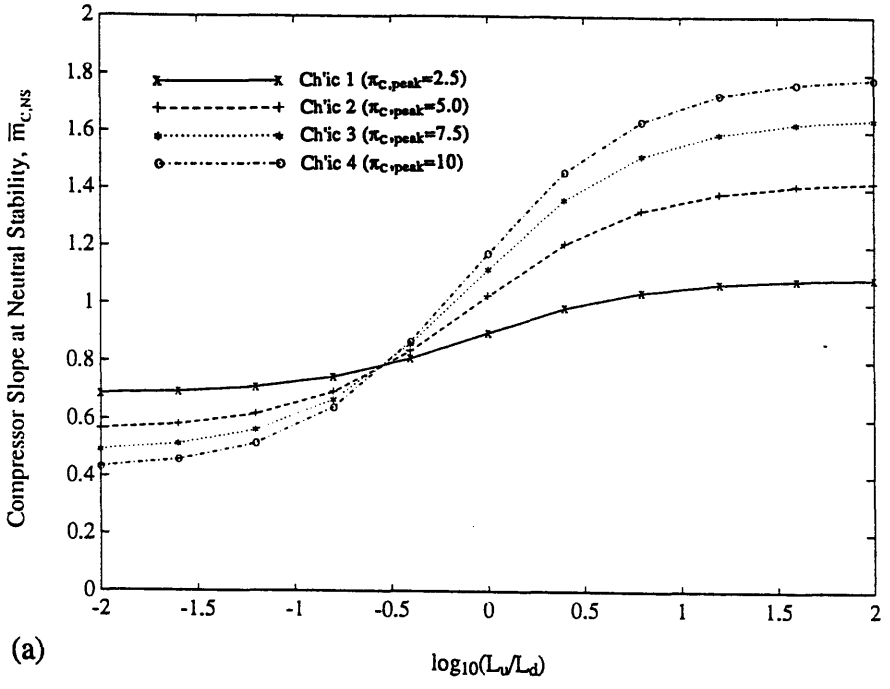

(a)

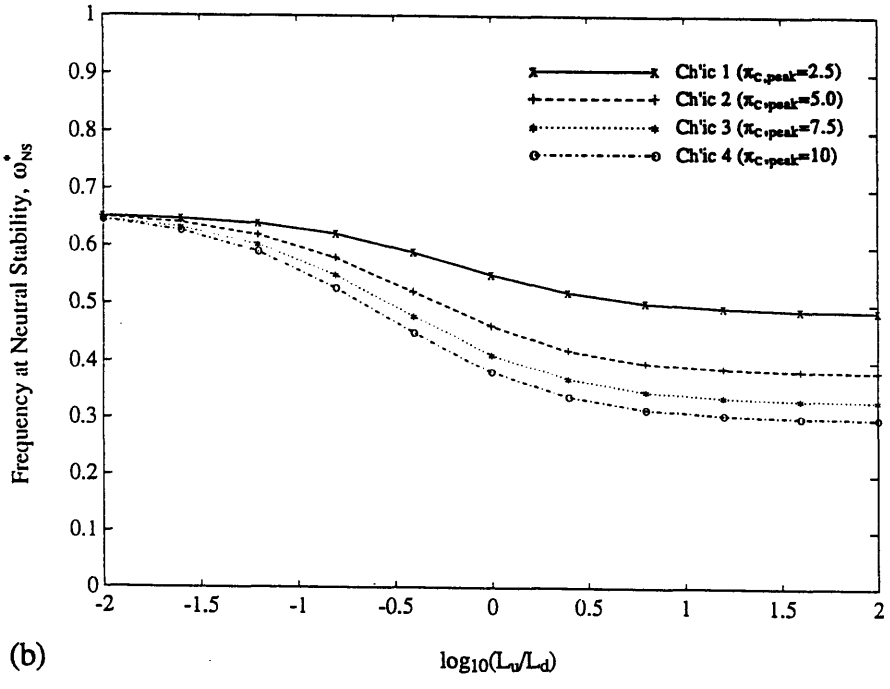

(b)

Figure 2.4: Effect of Inertia Ratio and Compressor Performance on (a) Slope and (b) Frequency at Neutral Stability for β=0.25, $m_{C,\theta}$=-0.5, θ_B=2.

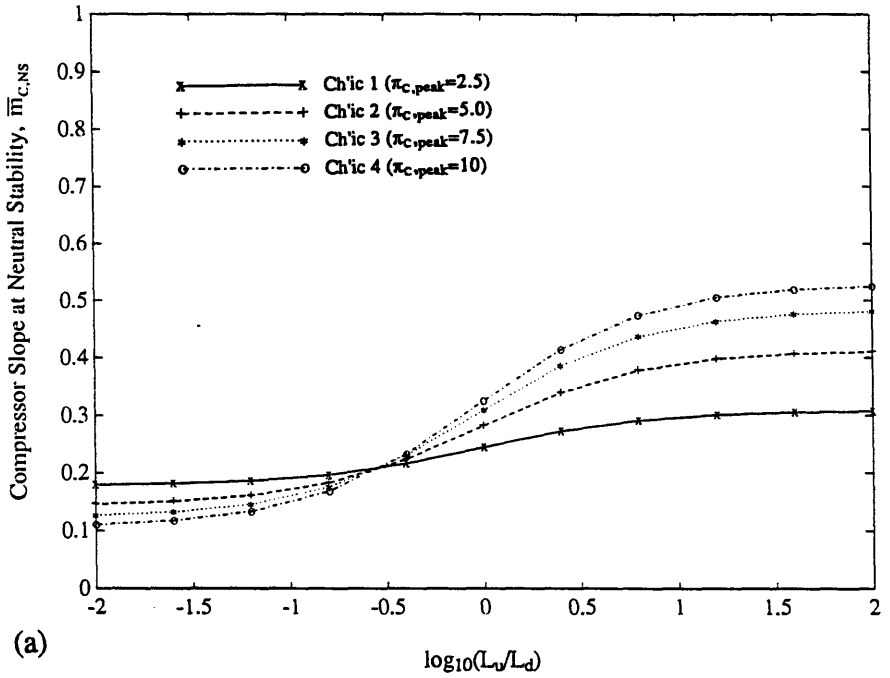

(a)

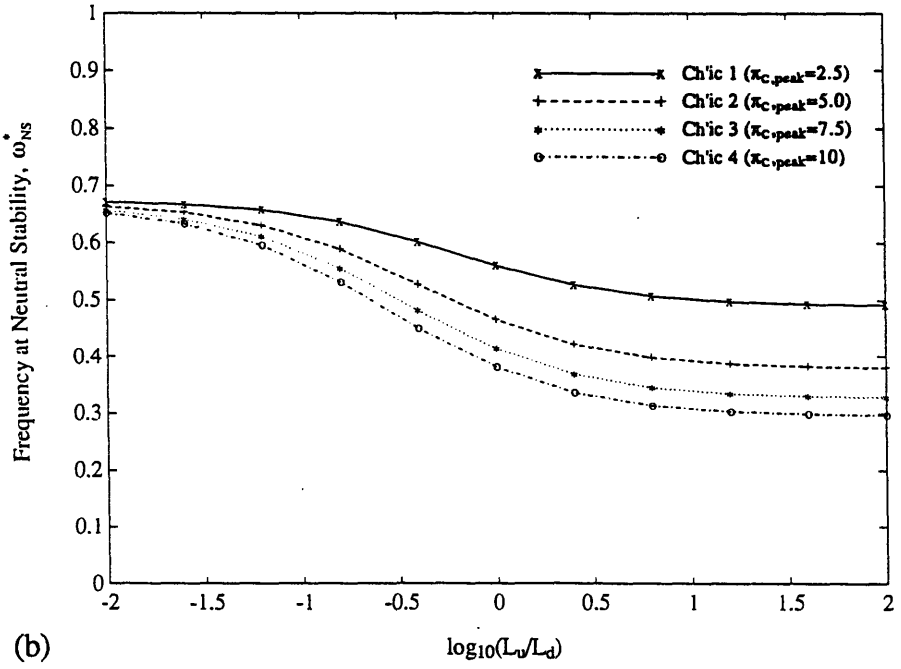

(b)

Figure 2.5: Effect of Inertia Ratio and Compressor Performance on (a) Slope and (b) Frequency at Neutral Stability for β=0.5, $m_{C,\theta}$=-0.5, θ_B=2.

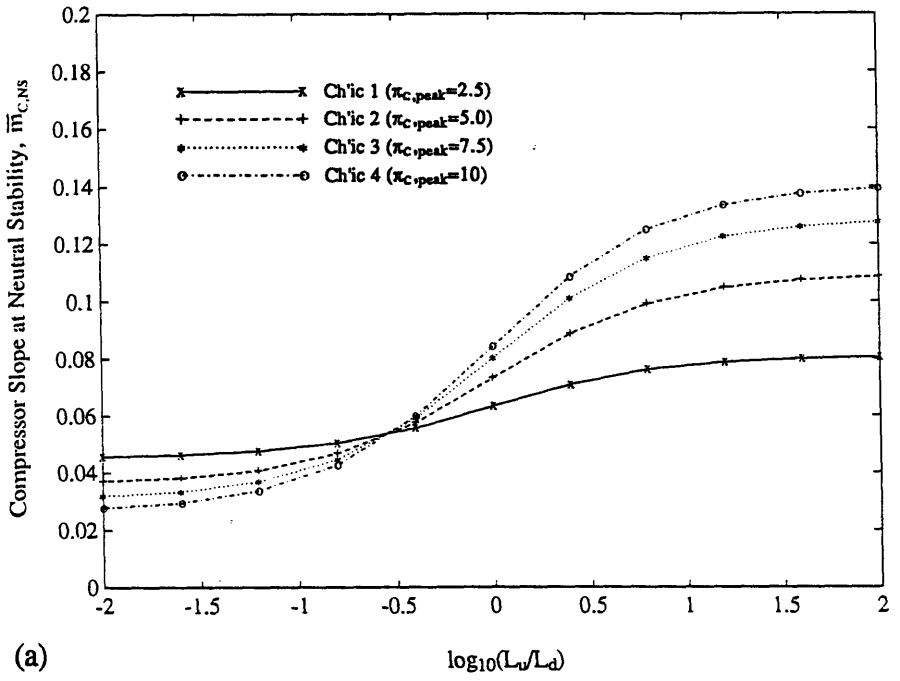

(a)

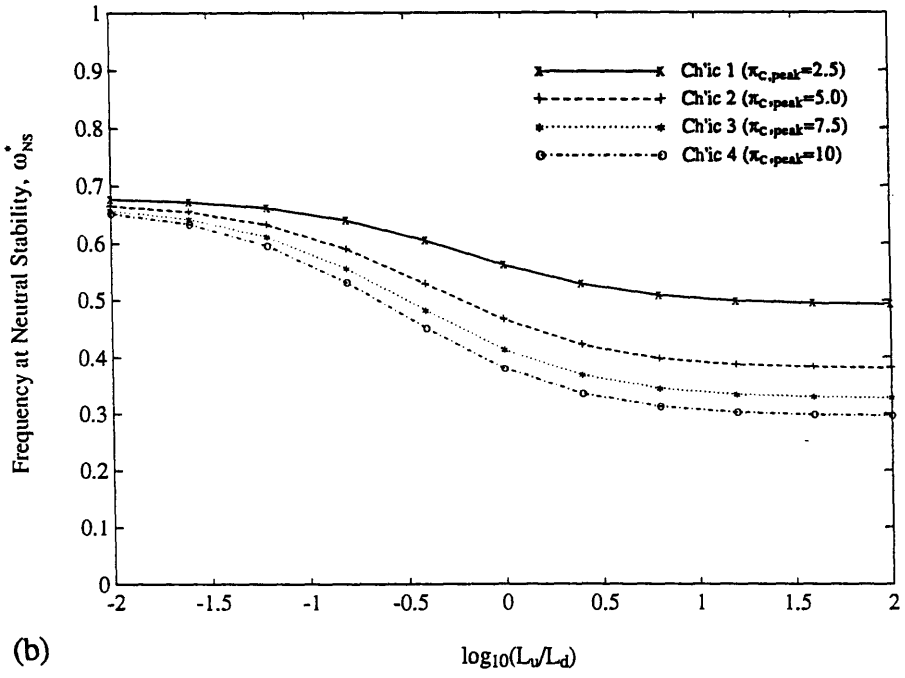

(b)

Figure 2.6: Effect of Inertia Ratio and Compressor Performance on (a) Slope and (b) Frequency at Neutral Stability for β=1, $m_{C,\theta}$=-0.5, θ_B=2.

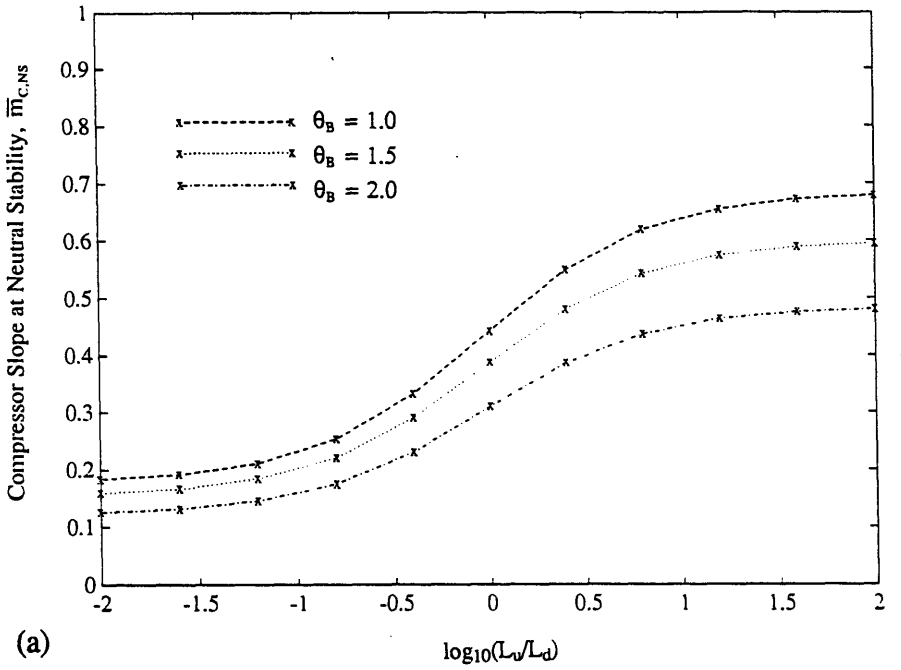

(a)

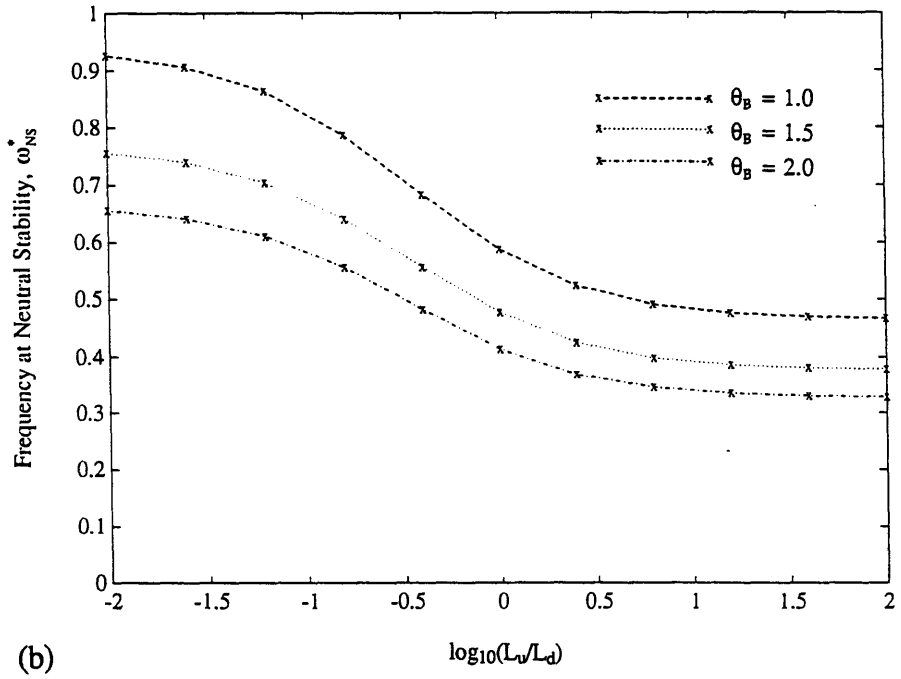

(b)

Figure 2.7: Effect of Burner Temperature Ratio and Inertia Ratio on (a) Slope and (b) Frequency at Neutral Stability for β=0.5, $m_{C,\theta}$=-0.5, Ch'ic 3 ($\pi_{C,peak}$=7.5).

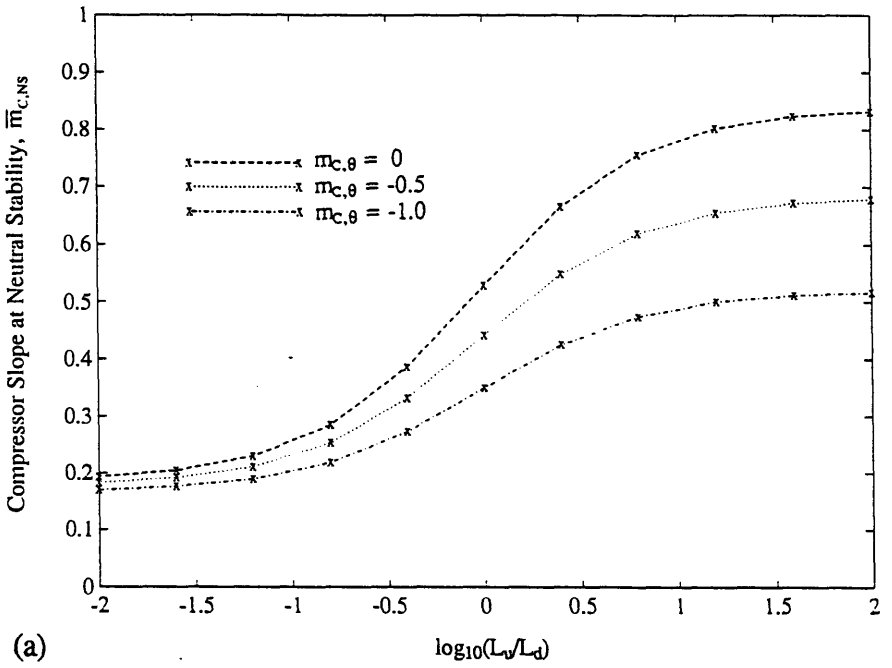

(a)

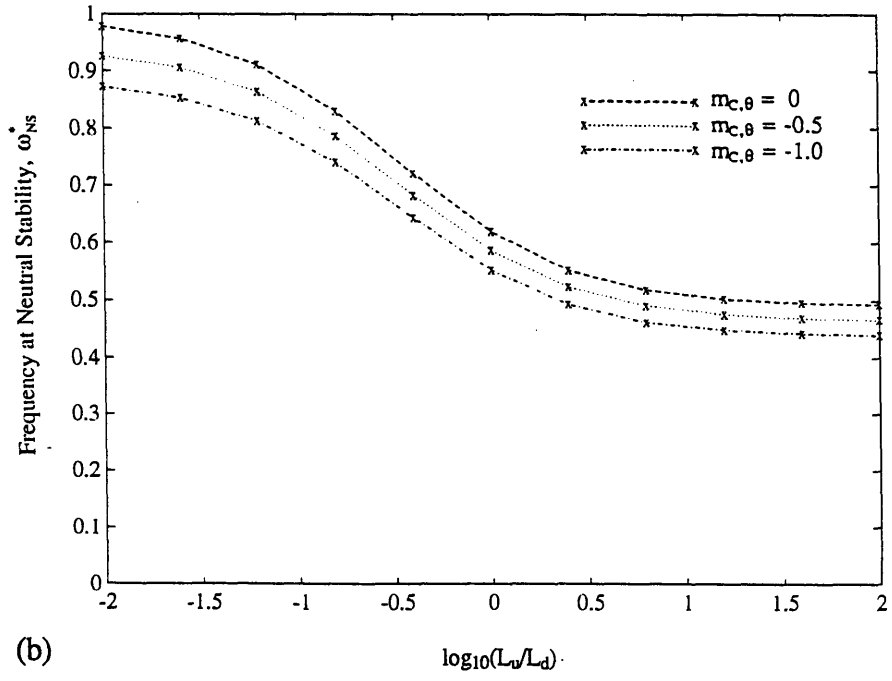

(b)

Figure 2.8: Effect of Compressor Temperature Slope and Inertia Ratio on (a) Slope and (b) Frequency at Neutral Stability for β=0.5, θ_B=1, Ch'ic 3 ($\pi_{C,peak}$=7.5).

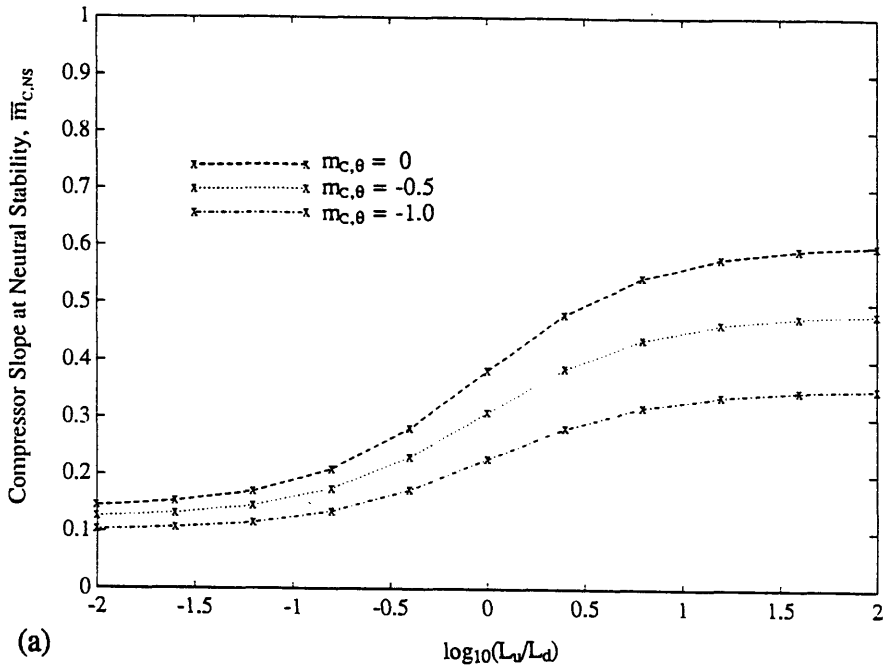

(a)

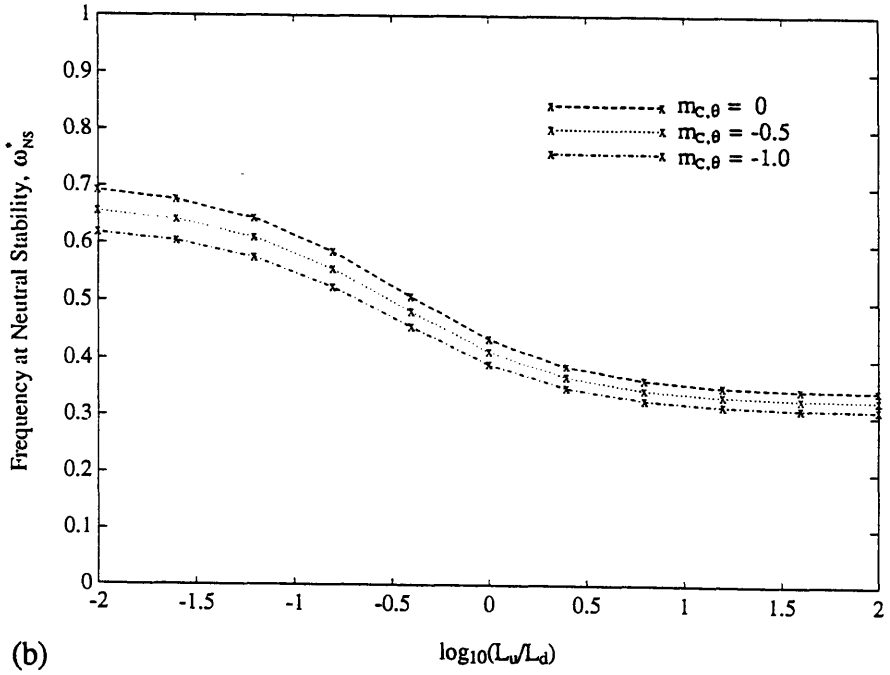

(b)

Figure 2.9: Effect of Compressor Temperature Slope and Inertia Ratio on (a) Slope and (b) Frequency at Neutral Stability for β=0.5, θ_B=2, Ch'ic 3 ($\pi_{C,peak}$=7.5).

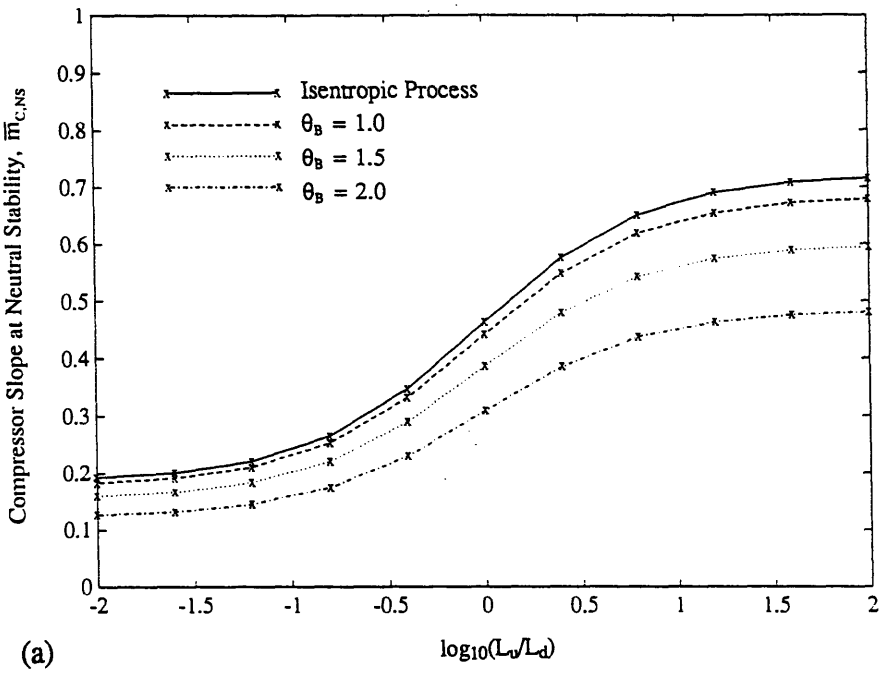

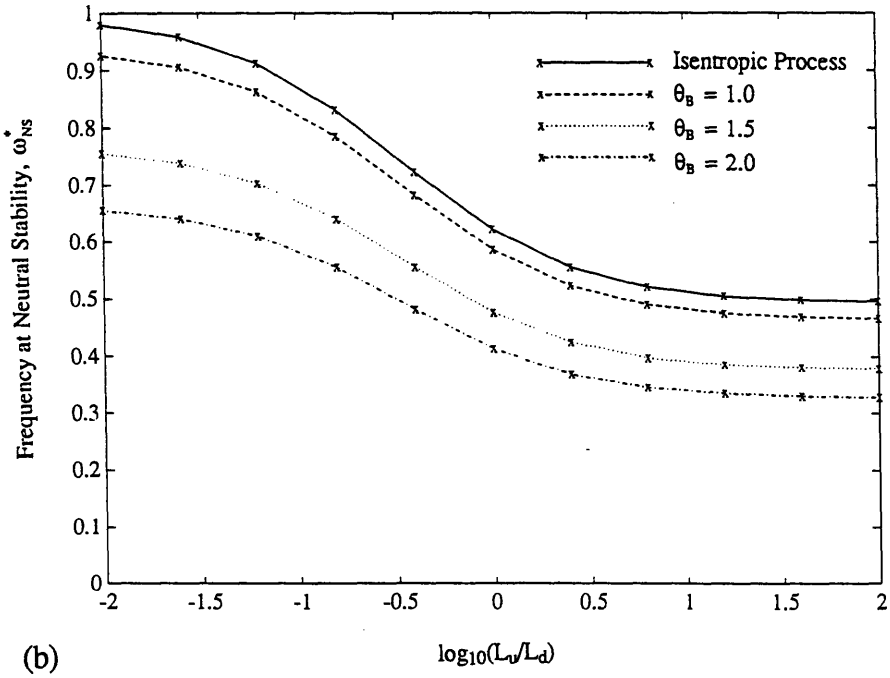

Figure 2.10: Assessment of Isentropic Process Assumption as a Function of Burner Temperature Ratio and Inertia Ratio for β=0.5, $m_{C,\theta}$=-0.5, Ch'ic 3.

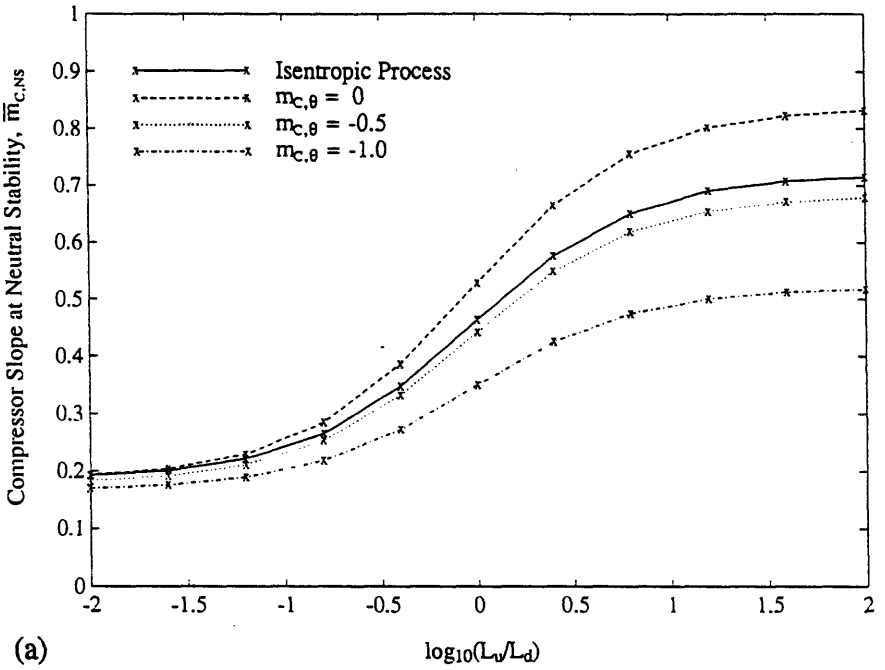

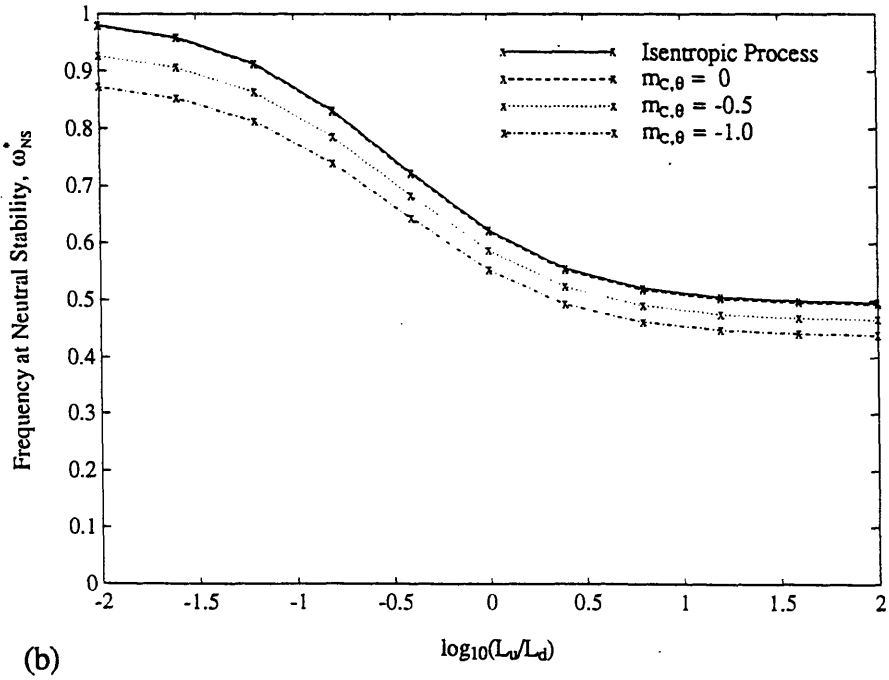

Figure 2.11: Assessment of Isentropic Process Assumption as a Function of Compressor Temperature Slope and Inertia Ratio for β=0.5,θ_B=1, Ch'ic 3.

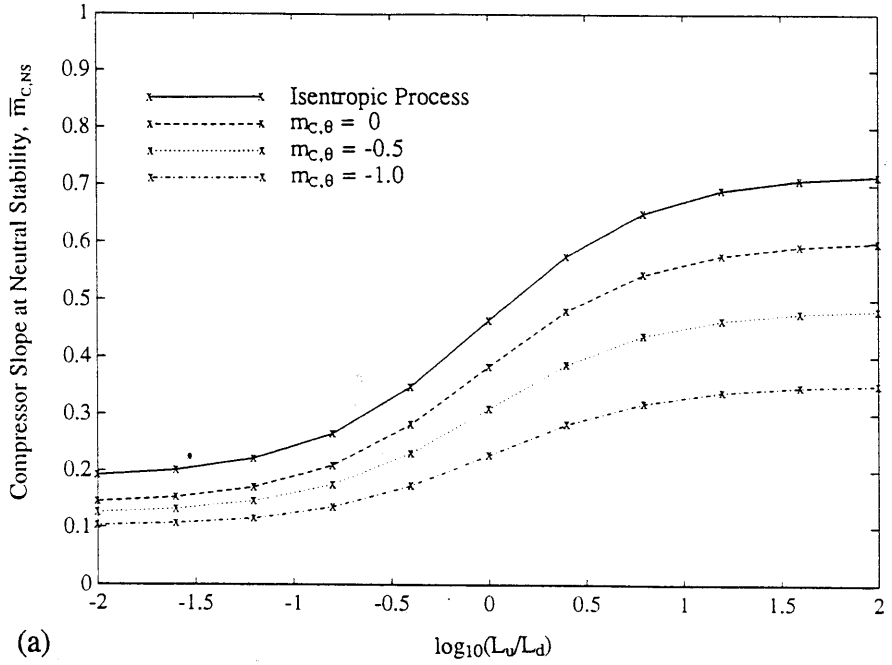

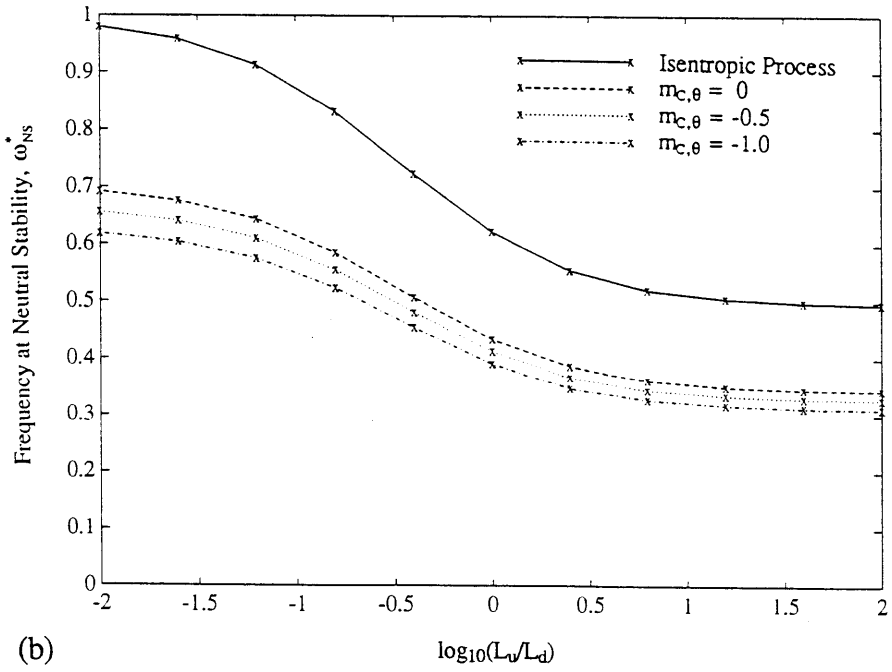

Figure 2.12: Assessment of Isentropic Process Assumption as a Function of Compressor Temperature Slope and Inertia Ratio for β=0.5,θ_B=2, Ch'ic 3.

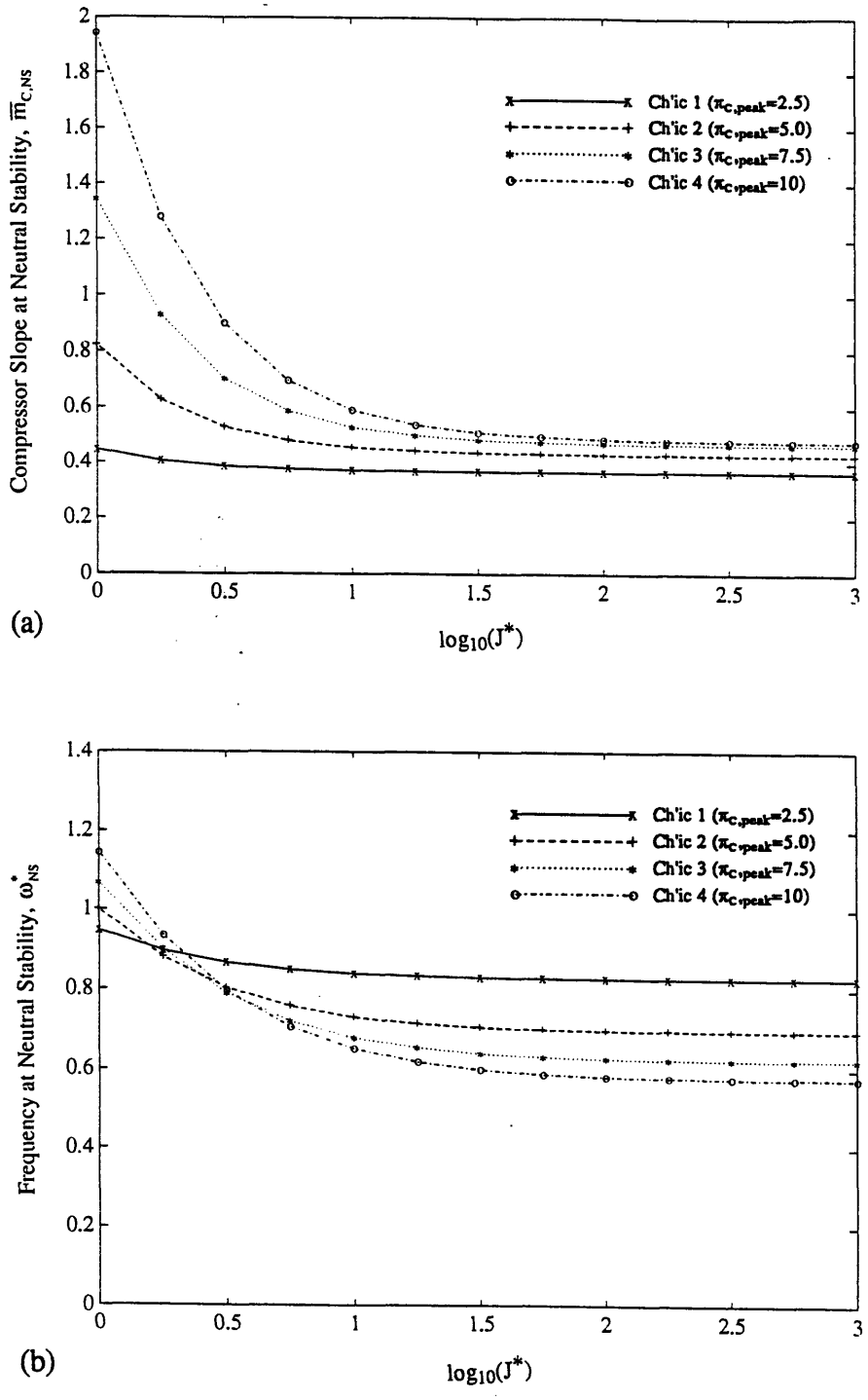

Figure 2.13: Assessment of Constant Rotor Speed Assumption as a Function of J^* and Compressor Performance for β=0.5, L_u/L_d=1, $m_{C,\theta}$=-0.5, θ_B=2.

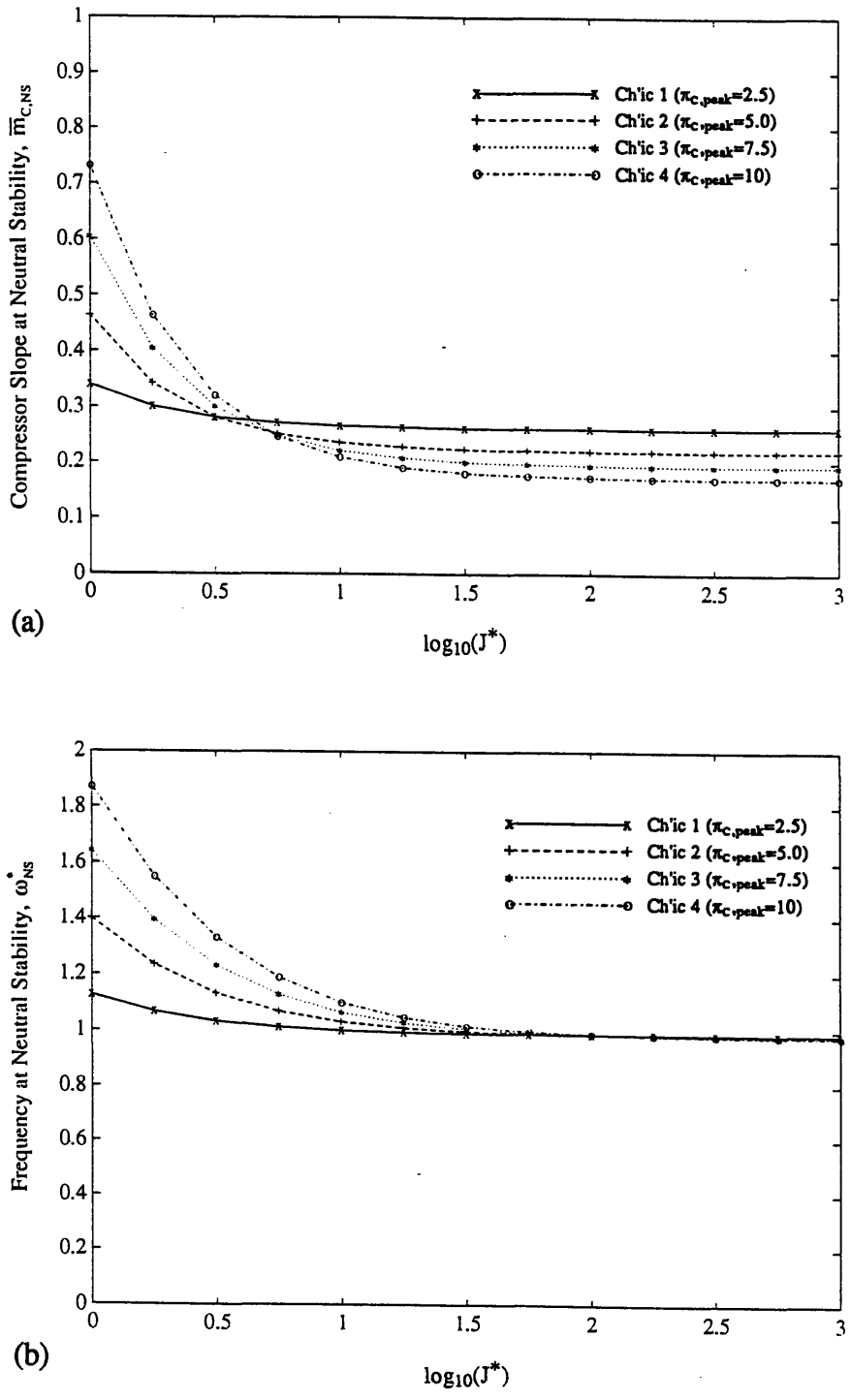

Figure 2.14: Assessment of Constant Rotor Speed Assumption as a Function of J^* and Compressor Performance for β=0.5, L_u/L_d=0.01, $m_{C,\theta}$=-0.5, θ_B=2.

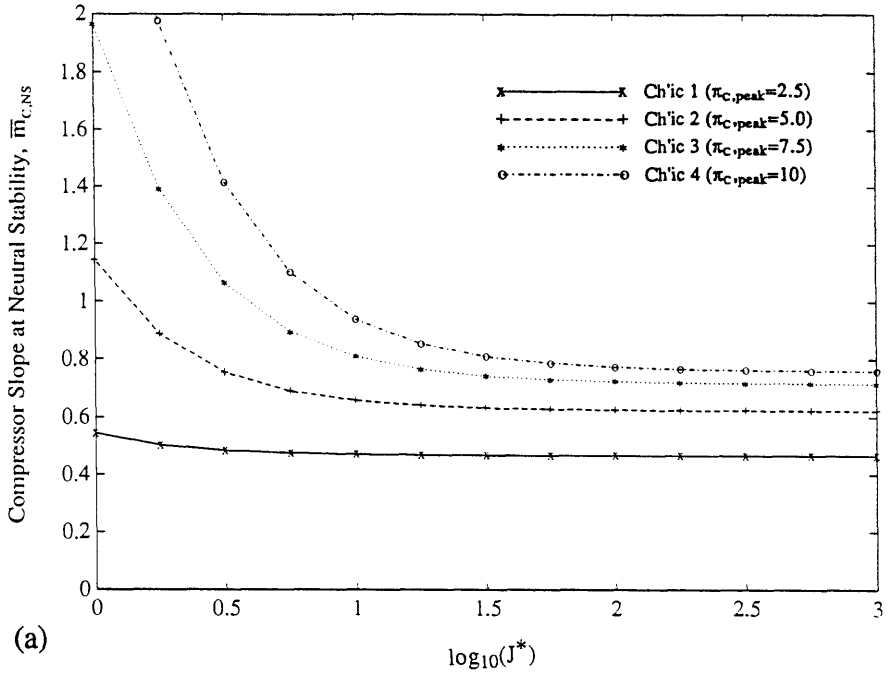

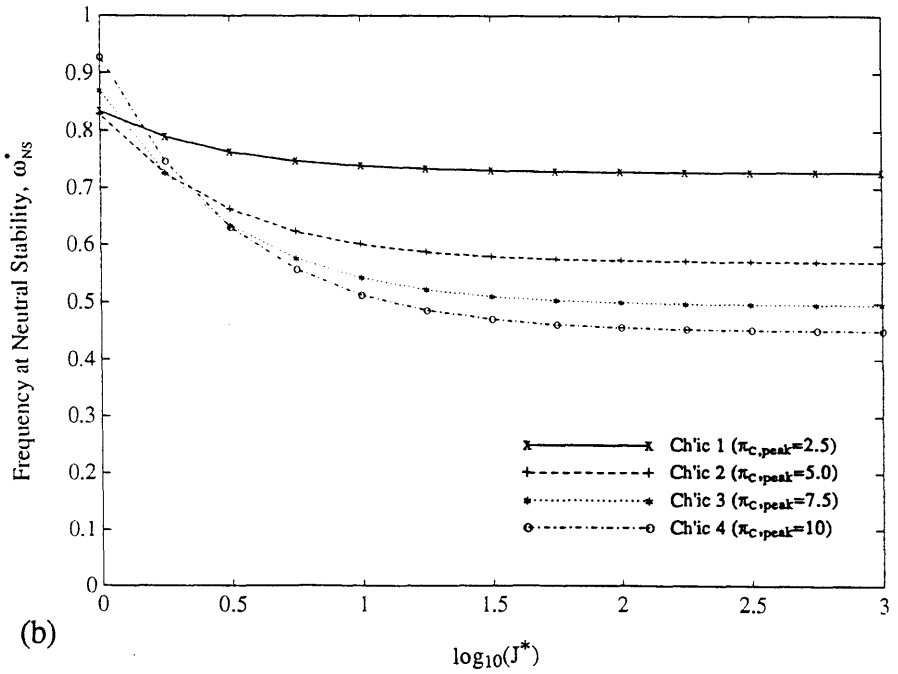

Figure 2.15: Assessment of Constant Rotor Speed Assumption as a Function of J^* and Compressor Performance for β=0.5, L_u/L_d=100, $m_{C,\theta}$=-0.5, θ_B=2.

Chapter 3
Evaluation of Dynamic Surge Control Strategies

3.1 Introduction

This chapter presents the modelling and evaluation of several actuator/sensor combinations as dynamic surge control strategies for a gas turbine engine. The actuation schemes to be studied are mass flow injection at the diffuser throat, a flow restriction close-coupled to the compressor, mass flow injection at the compressor inlet, mass flow bleed at the compressor exit, modulation of the fuel-flow and an auxiliary plenum which functions as an aerodynamic damper. The selection of actuators was limited to schemes felt to have reasonable opportunity for implementation in the helicopter engines acquired by the Gas Turbine Lab for active control experiments. The sensors examined were compressor duct mass flow, burner pressure and compressor inlet total pressure.

A further issue investigated in this chapter is the effect of controller bandwidth (the bandwidth of the combined actuator, processors and sensor) on the effectiveness of the various actuator/sensor pairs. Previous active surge control studies which modelled the effect of finite controller bandwidth (Simon [5]) were focused on compression systems with Helmholtz frequencies of roughly 10 Hz where the controller bandwidth was relatively much higher, say 10 times the system Helmholtz frequency. However, the estimated Helmholtz frequencies for helicopter engines are over 100 Hz and actuator bandwidths of 300 to 400 Hz are pushing the limits of current technology. These restrictions are therefore examined in more detail.

3.1.1 Scope of the Chapter

In this chapter the lumped parameter gas turbine engine surge model developed in Section 2.2 is used as the framework for the evaluation of the various actuator/sensor combinations. The assumptions and equations used to model the actuators are also discussed. Only linear stability is considered.

In this analysis the sensor output signals and actuator input signals are connected via proportional control laws. Control system dynamics are also included in the feedback path. The practical constraints placed on the control system, discussed in more detail below, are that the controller frequency, ω_C/ω_H, is limited to values less than 3 and that the magnitude of the gain is limited to a practical level.

3.1.2 Organization of the Chapter

The chapter begins with a section discussing the methodology used to evaluate the various actuator/sensor pairs. Each of the next six sections present one of the actuation schemes. The sections are arranged roughly from most to least effective: diffuser throat injection, close-coupled valve (flow-fence), compressor inlet injection, compressor exit bleed, fuel-flow modulation and the aerodynamic damper. In each of these sections the modelling and numerical results are given. The chapter concludes with a discussion section that compares and interpretes the various actuation approaches.

3.2 Method

The general approach used to evaluate the various surge control strategies is as follows. The actuator's influence on the engine fluid dynamics is modelled, the sensor is selected and the actuator input signal is connected to the sensor output signal by a proportional control law with controller dynamics in the feedback path. The resulting closed-loop, engine plus controller, system is illustrated in block diagram form in Fig.

3.1. The stability of the controlled system is evaluated from the eigenvalues of the closed-loop **A** matrix for the specified values of the compression system and control parameters. The slope of the curve of compressor pressure ratio versus corrected flow is the figure of merit used to assess the effectiveness of the control strategy in stabilizing the compression system. Figure 3.2 illustrates the flow range extension that would be obtained if the system is stabilized to the different values of compressor slope, for four characteristic shapes in the nominally unstable flow regime.

The approach for including control system dynamics is to model the controller dynamics as a second-order mass-spring-damper mechanical system. The non-dimensional parameters that characterize the controller dynamics are, ω_C/ω_H, loosely referred to as the controller bandwidth, and the damping ratio, ζ_C. To assess the influence of controller bandwidth, ω_C/ω_H is parametrically varied, but limited to values less than 3 to reflect practical constraints. The controller damping ratio is fixed at a value of 0.707.

A few words are in order regarding the role of controller bandwidth on system performance. The usual interpretation of controller bandwidth is that it accounts for undesirable time lags in the actuator response to a commanded input signal. However for the controller bandwidth range in this study, a more appropriate interpretation may be to consider the controller dynamics as a complex control law [41] (see Fig. 3.1). From this viewpoint, this analysis is a first step in the evaluation of dynamic compensators for active surge control, although no attempt is made to study other control laws which may be more effective.

An additional constraint imposed is an upper bound on actuation level. The actuator is sized based on practical considerations (for example, the compressor exit bleed actuator is sized for a maximum of 5 percent bleed flow) and nominally set halfway open for linear control. If the maximum perturbation in the sensed variable is known, the gain which saturates the actuator (i.e. moves it to a fully-open or fully-closed position) can be

estimated. Once the upper bound on the actuation level is determined, the maximum allowable gain is then estimated assuming a 1 percent maximum perturbation level for each of the sensed variables. The maximum gain is thus different for each actuator/sensor combination.

One interest in this study is to find actuator/sensor combinations that are effective in stabilizing the LTS-101 helicopter engine. Therefore the initial screening of actuators and sensors is done using the compression system parameters estimated for the LTS-101 engine operating at 95 percent speed (see Appendix A); namely, β=0.4, L_u/L_d=0.4, $M_{tip,a}$=1.57, θ_B=2 and the compressor pressure ratio ($\pi_{C,peak}$=7.4) and temperature ratio characteristics. For each actuation scheme the best sensor and optimum controller bandwidth, ω_C/ω_H, are selected. Parameter sweeps on β and L_u/L_d are then carried out to assess the control scheme performance for other engine geometries.

3.3 Diffuser Throat Injection

This approach involves the injection of air into the throat of the vaned-diffuser in the centrifugal compressor stage in response to a sensor signal of the system. The performance of a high pressure ratio centrifugal compressor stage depends strongly upon the flow conditions at the vaned-diffuser throat [35]. For steady-state injection into the throat, one would expect the diffuser performance to be affected as shown schematically in Fig. 3.3. Active modulation of the injection air into the diffuser throat thus creates unsteady pressure perturbations in response to some sensed variable.

3.3.1 Modelling

The flowfield existing in the vaned-diffuser of a high performance centrifugal compressor is extremely complex and offers little hope of a rigorous analysis of the effect of mass injection at the throat. The approach taken here is to develop a simple model of

the diffuser throat injection process that captures the dominant features of the flow to determine if further experimental study is warranted. As shown in Fig. 3.4, the compressor is split into two parts: the compressor minus the vaned-diffuser (C-VD) and the vaned-diffuser (VD). The mass injection is normal to the freestream at the inlet (throat) of the diffuser and is assumed to have a negligible influence on the components upstream of the throat. The (total-to-total) pressure ratio across the compressor is given as

$$\pi_C = \pi_{C-VD} \cdot \pi_{VD} \tag{3.1}$$

where,
$$\pi_{C-VD} = \pi_{C-VD}(W_{C,COR}, M_{tip,2}) \tag{3.2}$$

and
$$\pi_{VD} = \pi_{VD}(W_{C,COR}, M_{tip,2}, W_{inj}) \tag{3.3}$$

The following assumptions are made:

- The injection process is quasi-steady
- There is negligible flow inertia in the diffuser compared to the total flow inertia in the compressor duct (i.e. $L_{VD}/(L_u+L_d) << 1$)
- There is negligible compliance in the diffuser ($\omega_R^* \cdot M << 1$). The continuity equation is thus

$$W_d = W_C + W_{inj} \tag{3.4}$$

- The injection air total temperature is the same as the freestream total temperature
- The injector air is supplied from a constant pressure reservoir with the pressure high enough to choke the injector orifice
- The injector is modelled as a quasi-steady, one-dimensional, isentropic choked nozzle flow. The non-dimensional mass flow is given as

$$W_{inj} = \left(\frac{P^*_{o,inj} \cdot F(\gamma)}{\sqrt{T^*_{o,inj}}} \right) \cdot A^*_{inj} \tag{3.5}$$

For given values of $P^*_{o,inj}$ and $T^*_{o,inj}$, the injector flow is a function of only the non-dimensional injector area, A^*_{inj}, which is the control variable for this actuator.

The mass injection into the throat is assumed to affect the diffuser performance by two independent mechanisms: throat blockage and additional mixing. Values are estimated for the sensitivity of the vaned-diffuser pressure ratio, π_{VD}, to changes in the control variable, A^*_{inj}, for each of these two mechanisms; that is

$$\left(\overline{\frac{\partial \pi_{VD}}{\partial A^*_{inj}}}\right) = \left(\overline{\frac{\partial \pi_{VD}}{\partial BL_{th}}}\right)\left(\overline{\frac{\partial BL_{th}}{\partial W_{inj}}}\right)\left(\overline{\frac{\partial W_{inj}}{\partial A^*_{inj}}}\right) + \left(\overline{\frac{\partial \pi_{VD}}{\partial W_{inj}}}\right)_{mixing}\left(\overline{\frac{\partial W_{inj}}{\partial A^*_{inj}}}\right) \qquad (3.6)$$

The following method is used to estimate the sensitivity of diffuser performance to throat blockage, $\left(\overline{\frac{\partial \pi_{VD}}{\partial BL_{th}}}\right)$. The equation below (Eqn. 3.7) is derived (manipulating the results from Ref. 36) to give π_{VD} as a function of the actual and ideal (inviscid) diffuser static pressure coefficients, C_p and $C_{p,i}$, and the throat Mach number, M_{th}.

$$\pi_{VD} \equiv \frac{P_{O,ex}}{P_{O,th}} \cong \frac{\left(C_p + F(M_{th}) - 1\right)}{\left(C_{p,i} + F(M_{th}) - 1\right)} \qquad (3.7)$$

where,

$$C_p \equiv \frac{P_{ex} - P_{th}}{P_{O,ex} - P_{th}} = C_p(BL_{th}, M_{th}, geom, \ldots)$$

$$C_{p,i} \equiv \frac{P_{ex,i} - P_{th}}{P_{O,ex} - P_{th}} = C_{p,i}(A_{ex}/A_{th}, M_{th}, M_{ex})$$

$$F(M_{th}) = \frac{2 + (\gamma - 1)\cdot M_{th}^2}{\gamma \cdot M_{th}^2}$$

The injected mass flow will modify the throat blockage, BL_{th}, and the throat and exit Mach numbers, M_{th} and M_{ex}; the corresponding changes in C_p, $C_{p,i}$ and $F(M_{th})$ will affect the diffuser performance. However, the diffuser static pressure rise, C_p, is a strong function of the throat blockage and is assumed to dominate the other effects. This allows the diffuser sensitivity to throat blockage to be approximated as

$$\left(\overline{\frac{\partial \pi_{VD}}{\partial BL_{th}}}\right) \cong \frac{1}{\left(C_{p,i} + F(M_{th}) - 1\right)} \cdot \left(\overline{\frac{\partial C_p}{\partial BL_{th}}}\right) \qquad (3.8)$$

The value of $\left(\overline{\frac{\partial C_p}{\partial BL_{th}}}\right)$ is estimated from data for 2-D diffusers with near sonic throat Mach numbers [37] to be in the range: $-2 \le \left(\overline{\frac{\partial C_p}{\partial BL_{th}}}\right) \le -1$.

Next, the sensitivity of throat blockage to changes in W_{inj}, $\left(\overline{\frac{\partial BL_{th}}{\partial W_{inj}}}\right)$, is estimated. As illustrated in Fig. 3.5, the penetration of the injection jet into the freestream reduces the effective flow area; this is assumed to have the same effect as an increase in the blockage due to an increase in the boundary-layer thickness (mass flux defect). Thus for this model, the blockage due to the injection jet depends on how far the jet penetrates into the freestream. Empirical correlations for jet penetration into a subsonic, infinite freestream [32] were used to estimate the blockage increase as a function of the momentum ratio, q, defined as

$$q \equiv \frac{\rho_{inj} \cdot U_{inj}^2}{\rho_{fs} \cdot U_{fs}^2} = \left(\frac{P_{O,inj}}{P_{O,fs}}\right) \cdot \left(\frac{1+\frac{\gamma-1}{\gamma} \cdot M_{fs}^2}{1+\frac{\gamma-1}{\gamma} \cdot M_{inj}^2}\right)^{\frac{\gamma-1}{\gamma}} \cdot \left(\frac{M_{inj}^2}{M_{fs}^2}\right) \qquad (3.9)$$

For a momentum ratio slightly above 1 and a maximum injection mass flow of 5 percent, the maximum increase in blockage due to the injection jet was estimated to be roughly 25 percent. Therefore using Eqn. 3.8 a change in the diffuser pressure ratio between 11 and 23 percent is estimated.

An upper bound on the sensitivity of the diffuser performance to injection mass flow due to mixing affects, $\left(\overline{\frac{\partial \pi_{VD}}{\partial W_{inj}}}\right)_{mixing}$, is estimated assuming one-dimensional, completely mixed, compressible flow with normal mass injection. From compressible flow theory [32], the change in total pressure is estimated using the following equation

$$\left(\frac{P_{O,ex} - P_{O,th}}{P_{O,th}}\right)_{mixing} \equiv -\left(\gamma \cdot M_{th}^2\right) \cdot \frac{W_{inj}}{W_{fs}} \qquad (3.10)$$

For the maximum injection flow of 5 percent and a throat Mach number of 0.85, a 5 percent change in total pressure is estimated.

The sensitivity of the injector flow to changes in the injector area, $\left(\overline{\frac{\partial W_{inj}}{\partial A^{*}_{inj}}}\right)$, is found by differentiating Eqn. 3.5. The above estimates for the partial derivatives in Eqn. 3.6 were used to evaluate the effectiveness of the diffuser throat injection actuator.

The four sensors evaluated for this actuator are compressor duct upstream and downstream mass flow, W_C and W_d, burner pressure, P_B, and compressor inlet total pressure, $P_{O,2}$. The gains for each sensor are scaled so that a gain of unity means that a 1 percent perturbation in the sensed variable yields a 1 percent perturbation in the injected mass flow. The total injection mass flow allowed is 5 percent, so the maximum allowed perturbation in W_{inj} is ± 2.5 percent. Thus for the assumed maximum sensor output perturbation of 1 percent, the gain for each sensor is limited to magnitudes less than 2.5.

3.3.2 Results

Results for the diffuser throat injection actuator for the LTS-101 surge model parameters using the four different sensing options are presented in Figs. 3.6 through 3.9. Figure 3.6 shows the compressor slope at neutral stability as a function of the normalized gain, K_N, for upstream compressor duct mass flow, W_C, sensing. The three curves represent controller bandwidths, ω_C/ω_H, of 3, 2 and 1.

As can be observed in Fig. 3.6, increasing the controller bandwidth increases the effectiveness of this actuator/sensor pair. Also, for a fixed controller bandwidth there exists an optimum gain; if the magnitude of the gain is increased much beyond this optimum the controller can destabilize the system. Further, the magnitude of the optimum gain increases with controller bandwidth. The maximum compressor slope achieved with this actuator/sensor pair is roughly 6 (for ω_C/ω_H=3 and optimum gain setting).

Figure 3.7 presents a similar analysis for sensing downstream compressor duct mass flow, W_d. Basically the same trends are observed as with the W_C sensor (Fig. 3.6) except for a slight reduction in the maximum stable compressor slopes achieved.

The burner pressure sensor, P_B, is evaluated in Fig. 3.8. The three curves correspond to controller bandwidths of 3, 1 and 0.6. An interesting trend observed in this figure is that this actuator/sensor combination actually performs better as the controller bandwidth is decreased to value of ω_C/ω_H=0.6, which was the optimum bandwidth found (if ω_C/ω_H is decreased below 0.6 the controller's effectiveness begins to degrade). This illustrates the point that for proportional control feedback, certain actuator/sensor pairs do not necessarily perform better as controller bandwidth is increased. Another trend seen in the figure is that the ability to stabilize surge is increased as the gain is increased only up to a certain point. After that the performance drops-off rapidly. The maximum compressor slope achieved with this sensor is about 2.5.

The compressor inlet total pressure sensor, $P_{O,2}$, is examined in Fig. 3.9. The two curves are for values of ω_C/ω_H of 3 and 2 with the latter being the optimum bandwidth found. The performance of this actuator/sensor pair is not very sensitive to bandwidth. It improves monotonically as the gain is increased upto the limiting value of 2.5. The results for this sensor are promising, compared to the other sensors, with a maximum stable compressor slope above 12 for ω_C/ω_H =2 and K_N=2.5 but the gain is much larger.

In Figure 3.10 the $P_{O,2}$ sensor is further evaluated using the optimum controller bandwidth of ω_C/ω_H=2 (optimum for β=0.4 and L_u/L_d =0.4). In this figure the maximum stable compressor slope, $\overline{m}_{C,MAX}$, (with gains in the range $-2.5 \leq K_N \leq 2.5$) is given as a function of the inertia ratio, L_u/L_d, for the three curves representing stability parameters, β, of 0.25, 0.5 and 1. Control is less effective as β is increased as expected, for the same reason as with the open-loop. Also, for values of the inertia ratio less than 1, the controller is less effective than for values greater than 1.

3.4 Close-Coupled Valve (Flow-Fence)

The close-coupled valve actuation scheme evaluated in this section is shown schematically in Fig. 3.11. The type of valve under consideration is referred to as a "flow-fence". It is basically a metal ring around the annulus directly ahead of the compressor face. When extended into the freestream, the flow-fence affects the overall steady-state pressure rise as illustrated in Fig. 3.12. The interest in this device arises because the LTS-101 engine loaned to the Gas Turbine Laboratory is equiped with a flow-fence which is used to increase engine surge margin during starting. By modulating the flow-fence position, unsteady pressure perturbations can be created in the compressor duct.

3.4.1 Modelling

The flow-fence is modelled as being integral with the compressor; that is, no compliance or inertia is assumed between the fence and the compressor. The performance of the compressor plus fence combination is thus dependent upon the corrected mass flow, tip Mach number, and also the flow-fence position, X_{fp}. The normalized fence position, X_{fp}, is defined as 0 when fully retracted and 1 for maximum extension into the flow. This is expressed functionally as:

$$\pi_C \equiv \frac{P_{O,3}}{P_{O,2}} = \pi_C(W_{C,COR}, M_{tip,2}, X_{fp}) \qquad (3.11)$$

$$\theta_C \equiv \frac{T_{O,3}}{T_{O,2}} = \theta_C(W_{C,COR}, M_{tip,2}, X_{fp}) \qquad (3.12)$$

The experimental LTS-101 steady-state compressor performance maps were available for the complete range of flow-fence positions. These maps are used to model the effect of flow-fence actuation on the compression system. The three sensors evaluated are W_C, P_B and $P_{O,2}$. The gain for each sensor is normalized so that for a gain of 1, a 2.5

percent perturbation in the sensed variable yields a fully-open or fully-closed flow-fence. The maximum magnitude of the gain is thus 2.5.

3.4.2 Results

The results for flow-fence actuation, with the three different sensing options, are presented in Figs. 3.13 to 3.15. Figure 3.13 shows the compressor slope at neutral stability for W_C sensing. The three curves represent controller bandwidths of 3, 2 and 1. The trends are similar to those of Figs. 3.6 and 3.7 for diffuser throat injection. The maximum compressor slope achieved for this sensor is roughly 5 at the optimum gain setting and $\omega_C/\omega_H=3$.

Evaluation of burner pressure sensing is shown in Fig. 3.14. Similar trends are observed as those in Fig. 3.8 (diffuser throat injection with P_B sensing), with the optimum controller bandwidth also occuring at $\omega_C/\omega_H=0.6$. The maximum stable compressor slope found for this scheme is approximately 2.4.

In Figure 3.15 results are given for the inlet total pressure sensor. The three curves correspond to values of ω_C/ω_H of 3, 1 and 0.8 with the latter being the optimum value of the controller bandwidth found. For all three curves the control effectiveness increases as K_N is increased upto the maximum value of 2.5. The maximum compressor slope observed is 4.1 for $\omega_C/\omega_H=0.8$ and $K_N=2.5$.

The flow-fence actuator with W_C sensing yields the highest compressor slopes within the bandwidth and gain limitations imposed in this study. Figure 3.16 presents the maximum stable compressor slope as a function of the stability parameter, β, and the inertia ratio, L_u/L_d, for a controller bandwidth of $\omega_C/\omega_H=3$. As in the open-loop case, the maximum stable slope decreases as β is increased and L_u/L_d is decreased. Figure 3.17 illustrates the effect of controller bandwidth on the maximum stable slope for a nominal

value of β=0.5. For this actuator/sensor pair, bandwidth has a strong influence on the controller's effectiveness in stabilizing the compression system.

3.5 Compressor Inlet Injection

In this approach, as illustrated in Fig. 3.18, air is injected into the face of the compressor parallel to the freestream in response to a sensor signal of the system. The injection modulates the mass and momentum into the compressor which modifies the effective compressor unsteady performance.

3.5.1 Modelling

The inlet injection process is modelled as a quasi-steady, one-dimensional, compressible flow. The equation governing the change in total pressure assuming complete mixing of the mass injected parallel to the freestream is (from Ref. 32)

$$\frac{dP_O}{P_O} = -\gamma \cdot M^2 \cdot \left(1 - \frac{U_{inj}}{U_{fs}}\right) \cdot \frac{d\dot{m}_{inj}}{\dot{m}_{fs}} \tag{3.13}$$

Equation 3.13 is used to approximate the injector pressure ratio as a function of the relevant non-dimensional variables as,

$$\pi_{inj} \equiv \frac{P_{O,2}}{P_{O,2'}} \cong 1 - \gamma \cdot \overline{M}_{2'}^2 \cdot \left(1 - \frac{W_{inj}}{W_u} \cdot \frac{\overline{\rho_{2'}}}{\rho_{inj}} \cdot \frac{1}{A^*_{inj}}\right) \cdot \frac{W_{inj}}{W_u} \tag{3.14}$$

The perturbations in $M_{2'}$ and $\frac{\rho_{2'}}{\rho_{inj}}$ are assumed small compared to perturbations in W_u, W_{inj} and A^*_{inj}. The other relevant assumptions used in this analysis are:

- There is negligible flow inertia in the injection region (injector is close-coupled to the compressor and $L_{inj}/(L_u+L_d) << 1$)
- There is negligible mass storage in the injection region ($\omega^*_R \cdot M << 1$)
- The injection air total temperature is the same as freestream total temperature
- The injector air is supplied from a constant pressure reservoir
- The injection pressure is high enough to choke the injector orifice

- Flow in the injector is quasi-steady, one-dimensional, compressible and isentropic

The non-dimensional injector mass flow is given as a function of the injection pressure, temperature and area (for a quasi-steady, one-dimensional, isentropic, choked nozzle) as

$$W_{inj} = \left(\frac{P^*_{o,inj} \cdot F(\gamma)}{\sqrt{T^*_{o,inj}}} \right) \cdot A^*_{inj} \qquad (3.15)$$

Since $P^*_{o,inj}$ and $T^*_{o,inj}$ are constant, the injector flow is a function of only the non-dimensional injector area, A^*_{inj}, which is the control variable for this actuator.

The four sensors to be evaluated in this study are W_C, W_u, P_B and $P_{O,2'}$. The controller gain for each sensor is normalized so that a 1 percent perturbation in the sensed variable yields a 1 percent perturbation in the injection flow. No more than 5 percent injection mass flow is allowed. Thus for the assumed maximum perturbation in the sensor output signal of 1 percent, the normalized gain magnitude is limited to values less than 2.5.

3.5.2 Results

The results for the four different sensing options are given in Figs 3.19 through 3.22. The controller performance using the compressor mass flow sensor is shown in Fig. 3.19 where the compressor slope at neutral stability is plotted versus the normalized gain. The three curves are for controller bandwidths, ω_C/ω_H, of 3, 2 and 1. Similar trends are observed as those obtained with the diffuser throat injection and close-coupled valve actuators (Figs. 3.6, 3.7, 3.13). For the maximum controller bandwidth of ω_C/ω_H=3, a compressor slope slightly above 4 is achieved. Similar trends are also observed in Fig. 3.20 for a mass flow sensor upstream of the injector. The maximum stable compressor slope for the W_u sensor is roughly 3.25.

Figure 3.21 presents the results using the burner pressure sensor. The three curves are for bandwidths of ω_C/ω_H = 3, 2 and 0.6, with the latter being the optimum value found. The slope at neutral stability increases as the magnitude of the gain is increased to the limit of 2.5 with the maximum slope achieved slightly above 1.8 for ω_C/ω_H=0.6 and K_N=-2.5. Essentially the same trends are observed in Fig. 3.22 for the $P_{O,2'}$ sensor, with ω_C/ω_H=0.6 also the optimum controller bandwidth observed. The maximum stable slope attained was slightly above 1.7.

The results of Figs. 3.19 through 3.22 reveal that compressor mass flow is the most effective sensor for this actuator. In Figure 3.23 the effect of the stability parameter and inertia ratio on the maximum stable compressor slope is examined for a controller bandwidth of 3. In general as β is increased the controller's ability to stabilize the compression system is reduced, although this is less pronounced for inertia ratios above 1.

In Figure 3.24 the effect of controller bandwidth on the the maximum stable compressor slope is shown for a nominal value of β=0.5. For this actuator/sensor combination, bandwidth strongly influences the controller's ability to stabilize the system.

3.6 Compressor Exit Bleed

This approach, as illustrated in Fig. 3.25, consists of a variable area valve located at the exit of the compressor which is used to modulate the amount of mass flow bled from the compressor duct. The idea is to modulate the bleed valve area in proportion to a measured flow variable.

3.6.1 Modelling

The equations and assumptions used to model the effect of compressor exit bleed on the surge dynamics of a high pressure ratio compression system are:

- There is negligible flow inertia in the bleed region (bleed valve is close-coupled to the compressor and $L_{bl}/(L_u+L_d) << 1$)
- There is negligible mass storage in the bleed region ($\omega_R^* \cdot M << 1$)
- No viscous losses are incurred on the freestream due to the bleed flow
- Flow through the bleed valve is quasi-steady, one-dimensional and isentropic

Conservation of mass for the bleed region downstream of the compressor is given as

$$W_d = W_C - W_{bl} \tag{3.16}$$

The non-dimensional bleed mass flow is expressed as,

$$W_{bl} = \left(\frac{P^*_{O,3} \cdot F(\gamma)}{\sqrt{T^*_{O,3}}} \right) \cdot A^*_{bl} \tag{3.17}$$

Equations 3.16 and 3.17 are implemented within the framework of the open-loop engine surge model. The four sensors examined in this analysis are W_C, W_d, P_B and $P_{O,2}$. The gain for each sensor is normalized so that a 1 percent perturbation in the sensed variable yields an approximate 1 percent perturbation the the bleed mass flow. The maximum bleed flow is limited to 5 percent and thus the magnitude of the controller gain is limited to less than 2.5.

3.6.2 Results

The results for compressor exit bleed actuation are presented in Figs. 3.26 to 3.30. In Figure 3.26 the compressor slope at neutral stability is given as a function of controller gain and bandwidth for the W_C sensor. The figure shows that the ability to stabilize surge is increased as the bandwidth is decreased to the optimum value of ω_C/ω_H=0.5. A fall-off in control effectiveness is observed as the magnitude of the gain increases beyond a certain level. The maximum stable slope observed is approximately 2.4. Figure 3.27 shows similar trends for the downstream mass flow sensor. The maximum compressor slope obtained for this sensor is roughly 1.9 at the optimum bandwidth of ω_C/ω_H=0.3.

Results for the burner pressure sensor are given in Fig. 3.28. Decreasing the bandwidth has a slight stabilizing influence until the optimum value of ω_C/ω_H=1.2 is reached. The maximum slope realized with this sensor is roughly 1.2 (at K_N=-2.5 and ω_C/ω_H=1.2).

Figure 3.29 shows the results for the compressor inlet total pressure sensor. The three curves for ω_C/ω_H = 3, 2 and 1 illustrate the slight destabilizing effect of decreasing the controller bandwidth. A compressor slope of approximately 1 is attained for K_N=-2.5 and ω_C/ω_H=3.

Figures 3.26 through 3.29 indicate that the compressor mass flow sensor is the most effective for the compressor exit bleed actuator. Figure 3.30 presents the results of parametric variations in β and L_u/L_d for the W_C sensor. This actuator/sensor pair is sensitive to variations in β and L_u/L_d. There is a decrease in control effectiveness with increasing β and decreasing L_u/L_d.

3.7 Fuel-Flow Modulation

In this approach the fuel-flow rate into the combustor is modulated in response to a system output variable. The main advantage of this actuator is the relative ease of implementation.

3.7.1 Modelling

The equations used to model the effect of fuel-flow modulation were previously developed in Chapter 2. The conservation of energy equation is rewritten below for reference.

$$\frac{dP_B^*}{d\tau} = \frac{1}{\overline{T}_B^* \cdot \beta} \cdot \left(W_C \cdot T_{O,4}^* - W_T \cdot T_B^* \right) + \dot{Q}^* \qquad (2.32)$$

The non-dimensional heat-release rate is given as a function of the non-dimensional fuel-flow rate, W_F, as

$$\dot{Q}^* \equiv \left(\frac{\bar{\eta}_B \cdot HV \cdot (\gamma - 1)}{\bar{a}_B^2 \cdot \beta} \right) \cdot W_F \qquad (3.18)$$

The fuel-flow modulation affects the system dynamics through the heat-release term in the combustor energy balance.

The flow variables W_C, P_B and $P_{O,2}$ are assessed as possible sensing options. The gain for each sensor is scaled so that a 1 percent perturbation in the sensor signal results in an approximate 1 percent fuel-flow perturbation. As a practical constraint the maximum fuel-flow perturbation allowed is set at ± 2.5 percent. The magnitude of the normalized gain for each sensor is restricted to values less than 2.5.

3.7.2 Results

Figures 3.31 through 3.34 present the results of the fuel-flow modulation analysis. The three sensors are evaluated in Figs. 3.31, 3.32 and 3.33 for the nominal LTS-101 surge model parameters. In Figure 3.31, compressor slope at neutral stability is given as a function of the normalized gain for the three curves of ω_C/ω_H = 3, 1 and 0.4. From this figure it is observed that the compression system is destabilized by the controller for the maximum bandwidth of ω_C/ω_H=3. However, as the bandwidth is reduced to the optimum value of ω_C/ω_H=0.4, the performance noticeably improves, with a compressor slope of 1.8 being achieved.

Figure 3.32 presents the results for the burner pressure sensor. Decreasing the controller bandwidth has a slight stabilizing effect until the optimum of ω_C/ω_H=1 is reached. The maximum compressor slope achieved is 1.6 (at K_N=2.5 and ω_C/ω_H=1).

The results for the inlet total pressure sensor are given in Fig. 3.33. For this sensor controller performance is slightly degraded as the bandwidth is decreased. The maximum stable slope is roughly 1.4.

The above results indicate that the W_C sensor with a bandwidth of ω_C/ω_H=0.4 is the most effective for the fuel-flow modulation actuator. The affect of β and L_u/L_d on stability for this actuator/sensor pair is shown in Fig. 3.34. As β is increased the maximum stable compressor slope that can be achieved is reduced. It is also apparent that control is more difficult for inertia ratios less than 1.

3.8 Aerodynamic Damper

The aerodynamic damper is a passive surge control strategy, as opposed to the previous active control strategies, which extends the stable operating range through aerodynamic feedback in the compression system. The feedback is used to enhance the system's ability to dissipate unsteady fluid energy. The aerodynamic damper, as illustrated in Fig. 3.35, is essentially a damped Helmholtz resonator driven by unsteady pressure perturbations at the combustor inlet. The damper has its own fluid inertia, compliance and damping which can be tuned to achieve maximum unsteady energy damping.

3.8.1 Modelling

The aerodynamic damper is modelled using the following approximations:

- One-dimensional, unsteady, inviscid flow of a perfect gas in the inertia duct
- Flow in the inertia duct has negligible compliance
- Fluid in plenum volume is compressible, has negligible velocity, uniform flow properties and negligible flow inertia
- Plenum pressure is isentropically related to the plenum density
- All viscous losses are modelled using a quasi-steady throttle actuator disk

The conservation of momentum equation for the fluid in the damper inertia duct is given in the following non-dimensional, linearized form

$$\frac{d(\hat{W}_{AD})}{d\tau} = \beta \cdot I \cdot (\hat{P}^*_B - m_{AD} \cdot \hat{W}_{AD} - \hat{P}^*_{AD}) \qquad (3.19)$$

where, $m_{AD}\left(\equiv \frac{d(\Delta P^*_{O,AD})}{d(W_{AD})} \right)$ is the slope of the aerodynamic damper non-dimensional throttle characteristic and I is the Engine-to-Damper Inertia Ratio, defined as

$$I \equiv \frac{(L_u + L_d)/A_C}{L_{AD}/A_{AD}} \qquad (3.20)$$

The conservation of mass equation for the fluid in the damper plenum is

$$\frac{d(\hat{P}^*_{AD})}{d\tau} = \frac{1}{\beta} \cdot K \cdot \hat{W}_{AD} \qquad (3.21)$$

The Burner-to-Damper Compliance Ratio, K, is defined as

$$K \equiv \frac{\overline{T}^*_{AD}}{\overline{T}^*_B} \cdot \frac{V_B}{V_{AD}} = \frac{VR}{TR} \qquad (3.22)$$

where, the Burner-to-Damper Volume and Temperature Ratios, VR and TR, are defined as

$$VR \equiv \frac{V_B}{V_{AD}} \qquad (3.23) \qquad \text{and} \qquad TR \equiv \frac{\overline{T}^*_B}{\overline{T}^*_{AD}} \qquad (3.24)$$

The parameters I, VR and TR affect the degree of interaction between the compression system and the aerodynamic damper.

3.8.2 Results

The ojective is to find values of the aerodynamic damper parameters I, VR and m_{AD} that achieve maximum energy dissipation for the LTS-101 engine. The method used is to fix the value of I and search the remaining VR and m_{AD} parameter space. The nominal value of I chosen for this study was 0.15, which was selected based on accessibility constraints for the LTS-101 engine test stand (i.e. to get a long enough damper inertia duct).

The results of the parameter search are presented in Figs. 3.36 and 3.37. The maximum stable compressor slope attained is slightly above 1.7 for the optimum damper parameters of $m_{AD,opt}$=4.6 and VR_{opt}=1.35. These values are only local maximums. If

the nominal value of I (or any of the compression system parameters) is changed, different optimum values of m_{AD} and VR, as well as $m_{C,MAX}$, will be found.

In Figures 3.38, 3.39 and 3.40 the affect of "off-design" values of the stability parameter, β, and inertia ratio, L_u/L_d, are examined. Each figure corresponds to a different value of β, 0.25, 0.5 and 1, respectively. In each figure the damper geometry is fixed at I=0.15 and VR=1.35, the optimum values for β=0.4, L_u/L_d=0.4. The compressor slope at neutral stability is plotted as a function of m_{AD} for values of L_u/L_d of 0.1, 1 and 10. All three figures show the same general trends. The maximum stable compressor slope is increased as L_u/L_d is increased from 0.1 to 1 or higher, but there is little difference as L_u/L_d is increased from 1 to 10. The optimum value of the damper throttle slope tends to increase as L_u/L_d is increased and the maximum stable compressor slope is strongly reduced by increases in β.

3.9 Discussion of the Results

The results are summarized in Fig. 3.41 which is a plot of the maximum stable compressor slope achieved for each actuator/sensor pair examined. The most effective actuation approaches are diffuser throat injection, a close-coupled valve (flow-fence) and compressor inlet injection. All three actuators are close-coupled to the compressor and modulate the flow momentum in the duct. These approaches have a large influence on stability because they directly alter the compressor's ability to feed unsteady energy into the flow disturbances. For example, if a close-coupled actuator is used to create pressure perturbations 180° out of phase with compressor mass flow perturbations (the sensor), the effective slope of the equivalent compressor (compressor plus controller) can be made negative, even though the quasi-steady slope of the uncontrolled compressor is positive [39,41]. This is illustrated schematically in Fig. 3.42; it is analogous to the equivalent resistance of two resistors in series.

The most effective actuator/sensor combination was diffuser throat injection with inlet total pressure sensing, achieving a stabilized compressor slope of roughly 12. Diffuser throat injection with compressor mass flow sensing was also effective, achieving a slope of approximately 6. The close-coupled valve and inlet injection actuators with compressor mass flow sensing stabilized the system to slopes of roughly 4 to 5.

Some common features are observed for the close-coupled control schemes that actuate on the duct flow momentum while sensing compressor mass flow. The controller's ability to stabilize the system significantly improves as controller bandwidth is increased. In this approach, time lags between the pressure perturbations created by the actuator in reponse to the sensed compressor mass flow perturbations are undesirable because the controller is less effective in modifying the unsteady compressor slope. Therefore if higher actuator bandwidths can be achieved (ω_C/ω_H=3 was the highest value considered in this study), steeper compressor slopes can be obtained. Close-coupled control is also less sensitive to increases in the system compliance-to-inertia ratio, β. As illustrated in Fig. 3.43 [39], the damping provided by flow momentum actuation with compressor flow sensing is not decoupled from the compressor (the energy source) as β is increased, as is the case for other downstream actuation/sensing approaches. For engines with large values of the stability parameter, β, this type of control strategy is desirable.

The compressor exit bleed actuator is also close-coupled to the compressor but only modulates the mass flow, not momentum. The maximum compressor slope obtained was roughly 2.5 using a mass flow sensor. This actuator/sensor pair performed better at a "low" controller bandwidth of ω_C/ω_H=0.5; this scheme could possibly be improved through better control law design. This control strategy is sensitive to increases in β.

Fuel-flow modulation and the aerodynamic damper control strategies, both of which actuate in the downstream plenum, are the least effective. As expected, both

approaches are sensitive to increases in β. The maximum compressor slope achieved with these schemes were roughly 2. Fuel-flow modulation performed best, with a compressor mass flow sensor, at a controller frequency ratio of $\omega_C/\omega_H=0.4$. Although the passive aerodynamic damper was not the most effective control strategy, it is an interesting approach because it does not require any electromechanical actuators, sensors or processors; no external power or mass flow is required and no steady-state pressure drop is associated with its use.

The mass flow range extension that will be obtained for each of these control strategies is not known because the compressor characteristic in the nominally unstable flow regime is unknown (illustrated in Fig. 3.2). If the compressor performance falls-off steeply past the peak of the speedline then the more effective close-coupled actuators must be used to gain a noticable improvement in stability. However, if the compressor performance is smoothly extended past the peak of the speedline, the less effective strategies might also yield significant increases in the stable flow range.

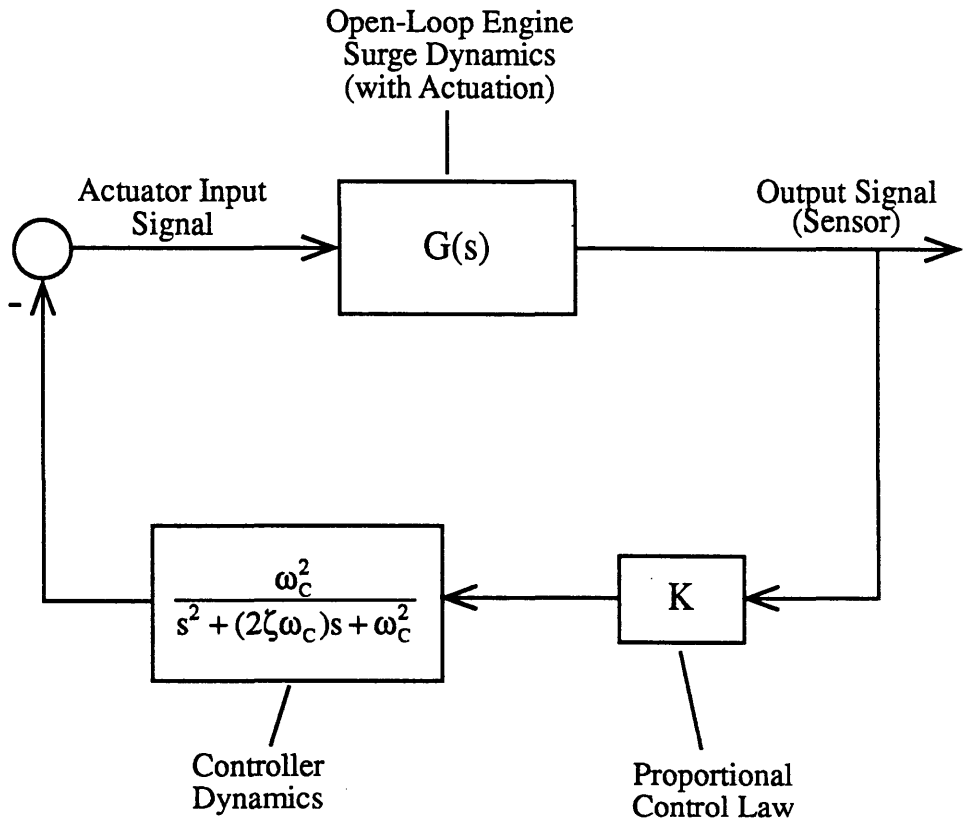

Figure 3.1: Block Diagram of Closed-Loop, Engine plus Controller, System.

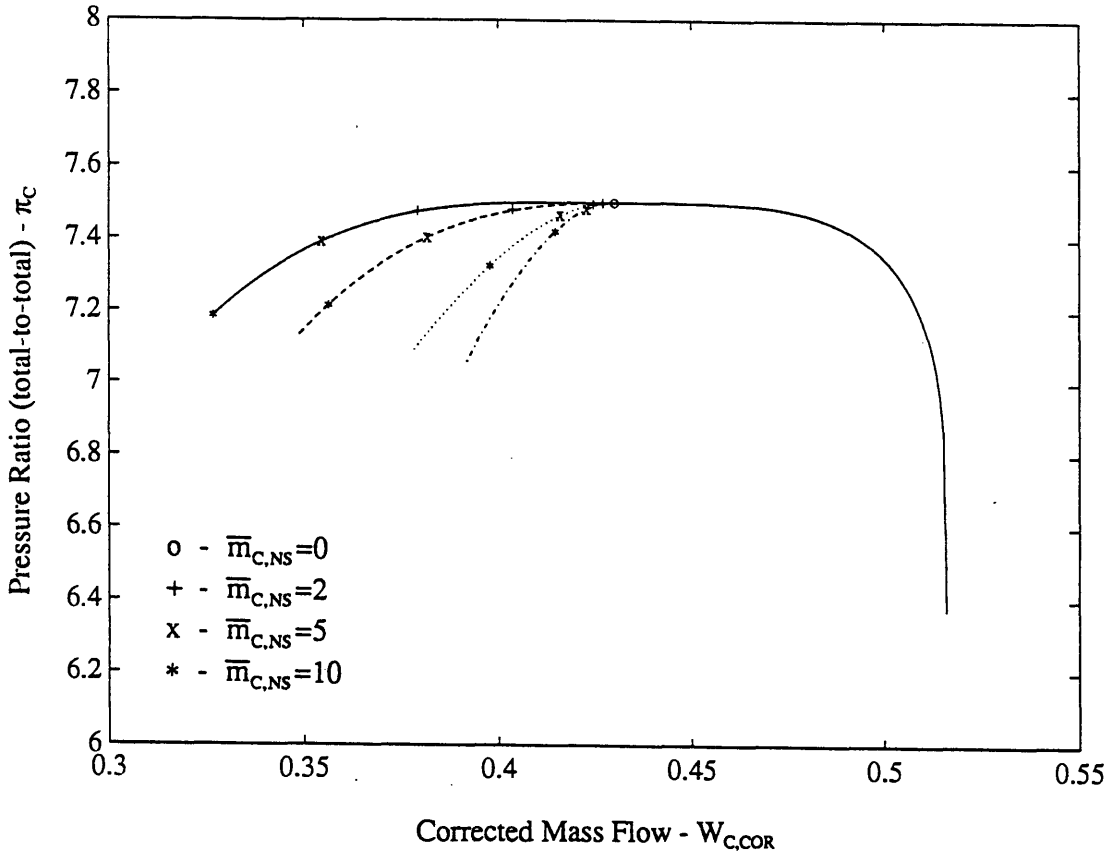

Figure 3.2: Compressor Characteristic Illustrating the Dependence of Flow Range Extension with Compressor Slope and Stalling Behavior.

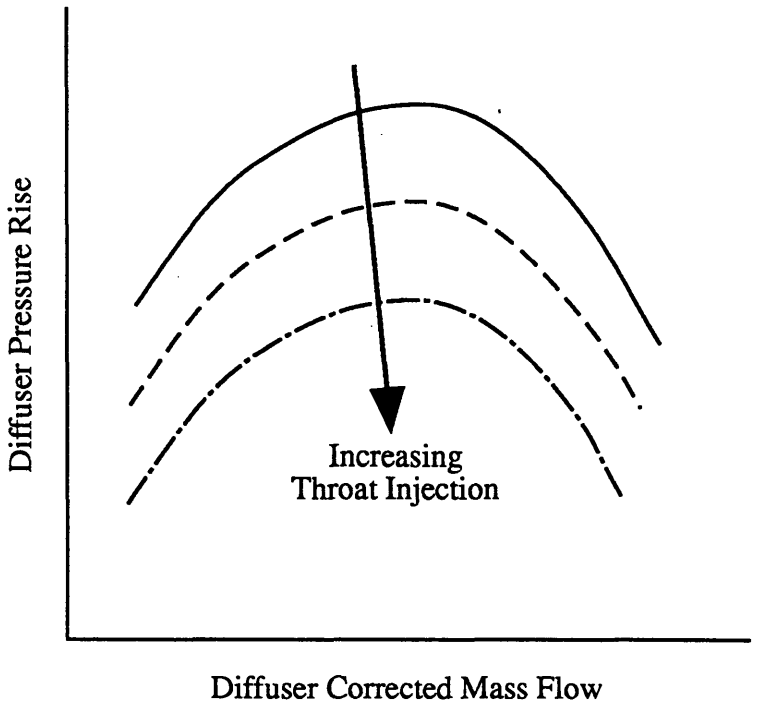

Figure 3.3: Schematic Representation of the Effect of Steady-State Mass Injection into the Diffuser Throat.

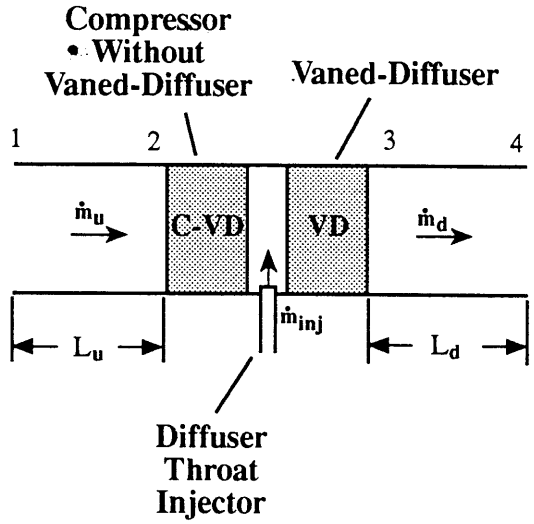

Figure 3.4: Schematic of Diffuser Throat Injection Actuator.

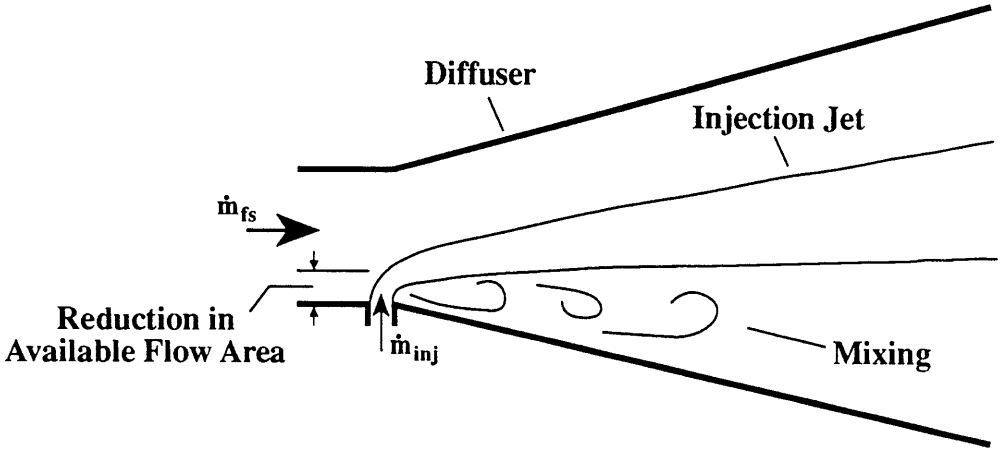

Figure 3.5: Schematic of Flowfield in Diffuser Passage with Mass Injection at the Throat.

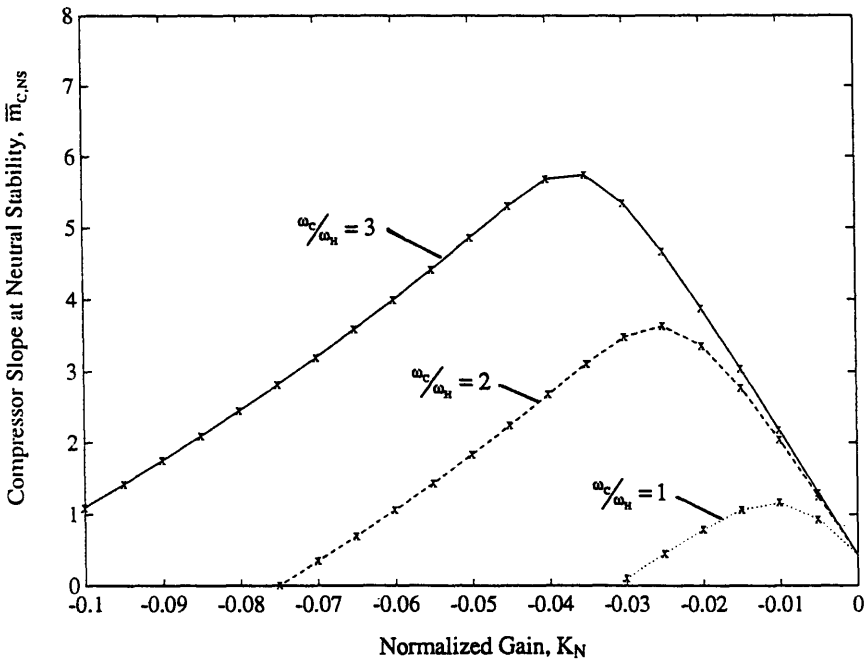

Figure 3.6: Closed-Loop Stability for Diffuser Throat Injection with Compressor Mass Flow Sensor (W_C) as a Function of Controller Bandwidth (ω_C/ω_H) and Gain (K_N): β=0.4, L_u/L_d=0.4, θ_B=2, LTS-101 Ch'ic.

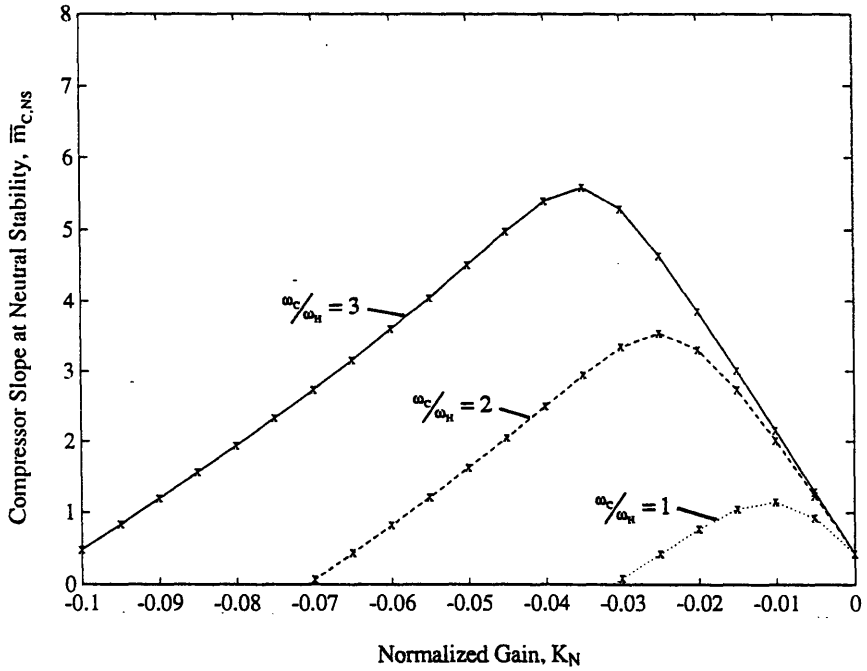

Figure 3.7: Closed-Loop Stability for Diffuser Throat Injection with Downstream Duct Mass Flow Sensor (W_d) as a Function of Controller Bandwidth (ω_C/ω_H) and Gain (K_N): β=0.4, L_u/L_d=0.4, θ_B=2, LTS-101 Ch'ic.

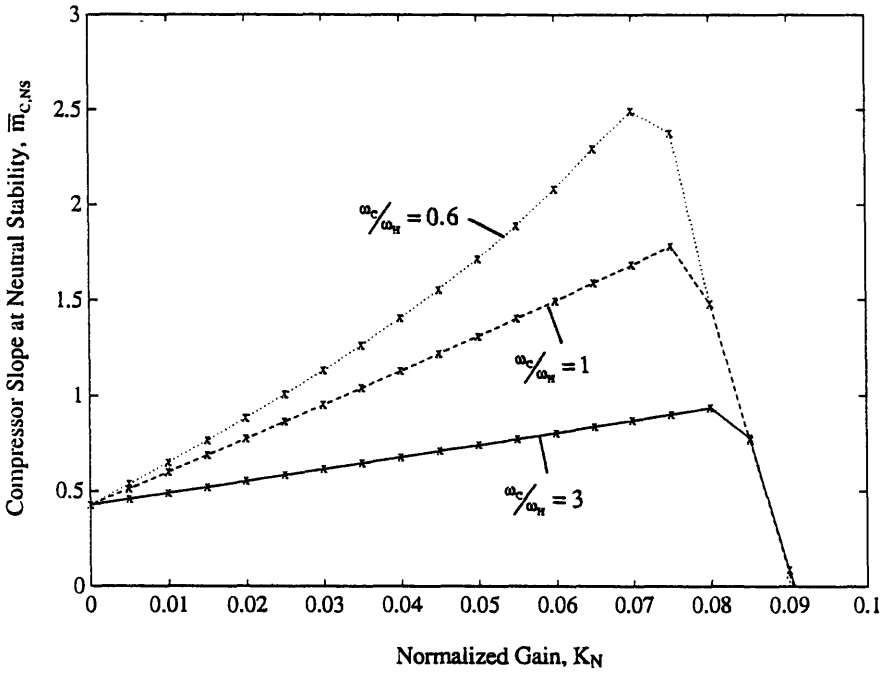

Figure 3.8: Closed-Loop Stability for Diffuser Throat Injection with Burner Pressure Sensor (P^*_B) as a Function of Controller Bandwidth (ω_C/ω_H) and Gain (K_N): β=0.4, L_u/L_d=0.4, θ_B=2, LTS-101 Ch'ic.

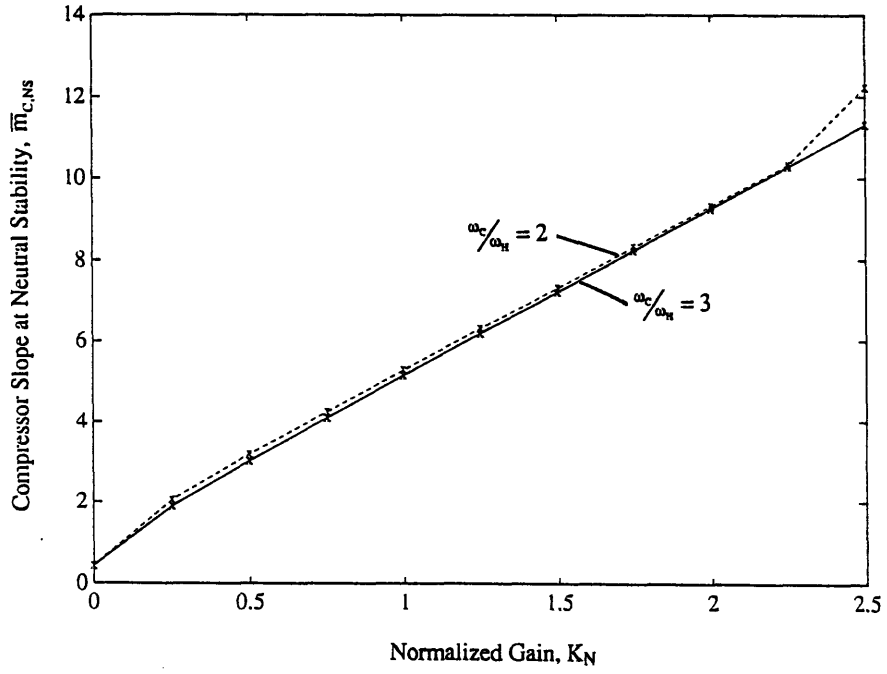

Figure 3.9: Closed-Loop Stability for Diffuser Throat Injection with Inlet Total Pressure Sensor ($P^*_{O,2}$) as a Function of Controller Bandwidth (ω_C/ω_H) and Gain (K_N): β=0.4, L_u/L_d=0.4, θ_B=2, LTS-101 Ch'ic.

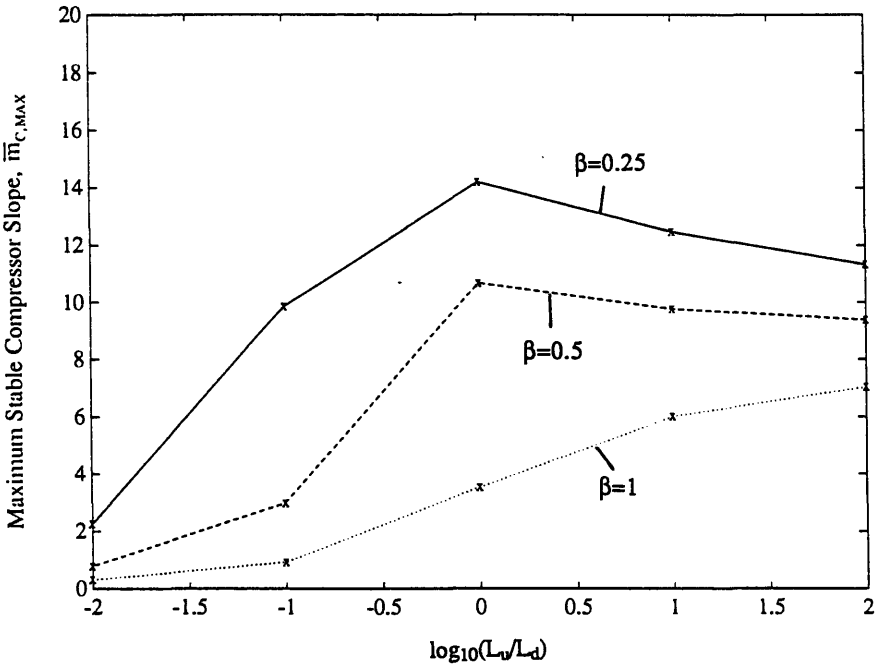

Figure 3.10: Maximum Stable Compressor Slope for Diffuser Throat Injection with Inlet Total Pressure Sensor as a Function of the Stability Parameter and Inertia Ratio: $(\omega_C/\omega_H)_{opt}=2$, $-2.5<K_N<2.5$, $\theta_B=2$, LTS-101 Ch'ic.

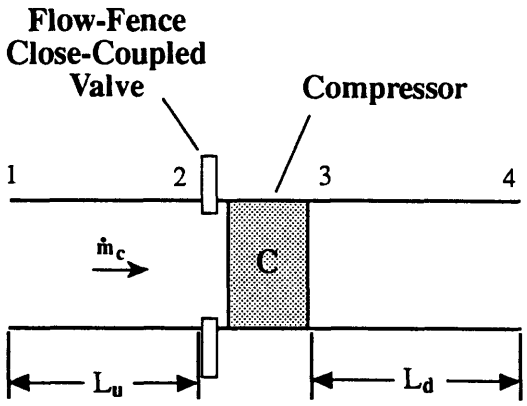

Figure 3.11: Schematic of Flow-Fence Close-Coupled Valve Actuator.

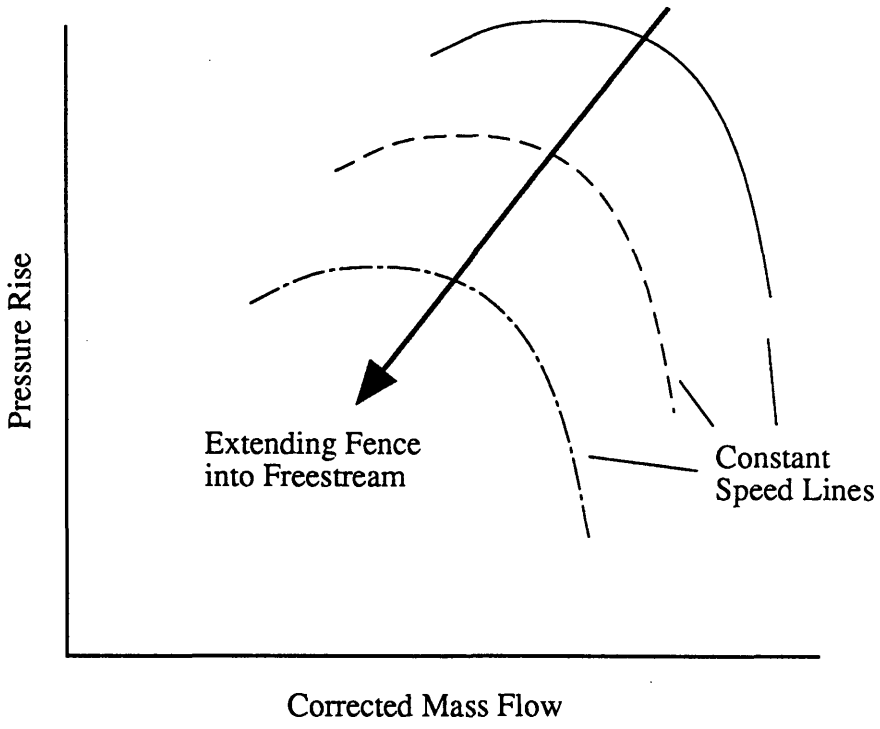

Figure 3.12: Schematic Representation of the Effect of Steady Flow-Fence Extension into the Freestream on Compressor plus Flow-Fence Performance.

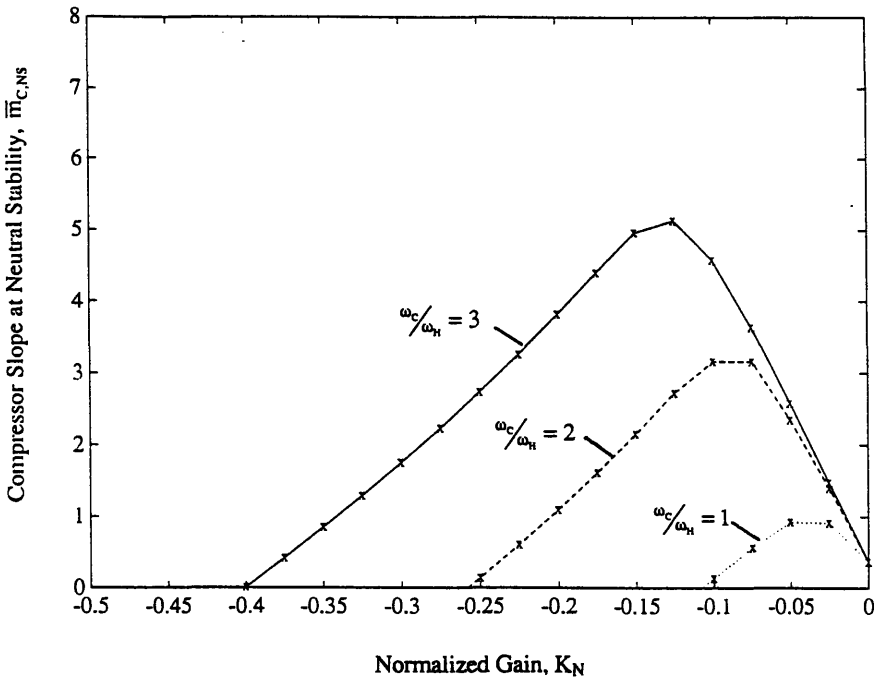

Figure 3.13: Closed-Loop Stability for the Flow-Fence Valve with Compressor Mass Flow Sensor (W_C) as a Function of Controller Bandwidth (ω_C/ω_H) and Gain (K_N): β=0.4, L_u/L_d=0.4, θ_B=2, LTS-101 Ch'ic.

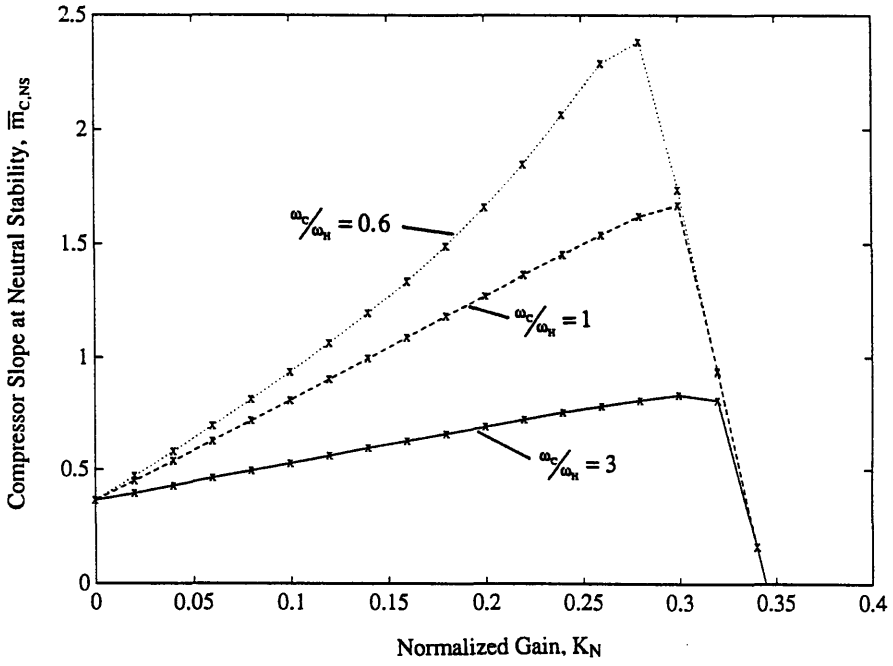

Figure 3.14: Closed-Loop Stability for the Flow-Fence Valve with Burner Pressure Sensor (P_B^*) as a Function of Controller Bandwidth (ω_C/ω_H) and Gain (K_N): β=0.4, L_u/L_d=0.4, θ_B=2, LTS-101 Ch'ic.

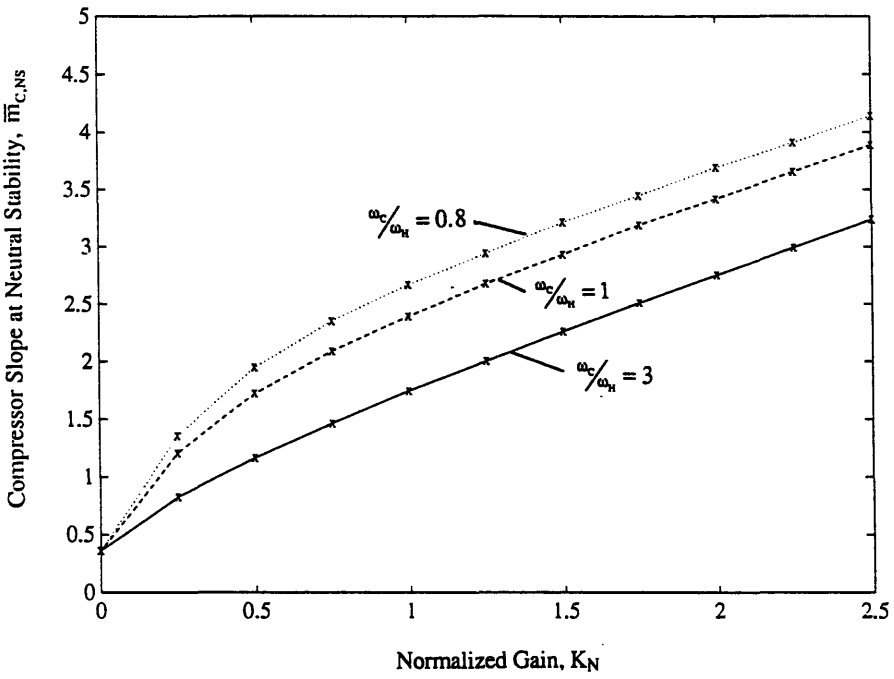

Figure 3.15: Closed-Loop Stability for the Flow-Fence Valve with Inlet Total Pressure Sensor ($P^*_{O,2}$) as a Function of Controller Bandwidth (ω_C/ω_H) and Gain (K_N): β=0.4, L_u/L_d=0.4, θ_B=2, LTS-101 Ch'ic.

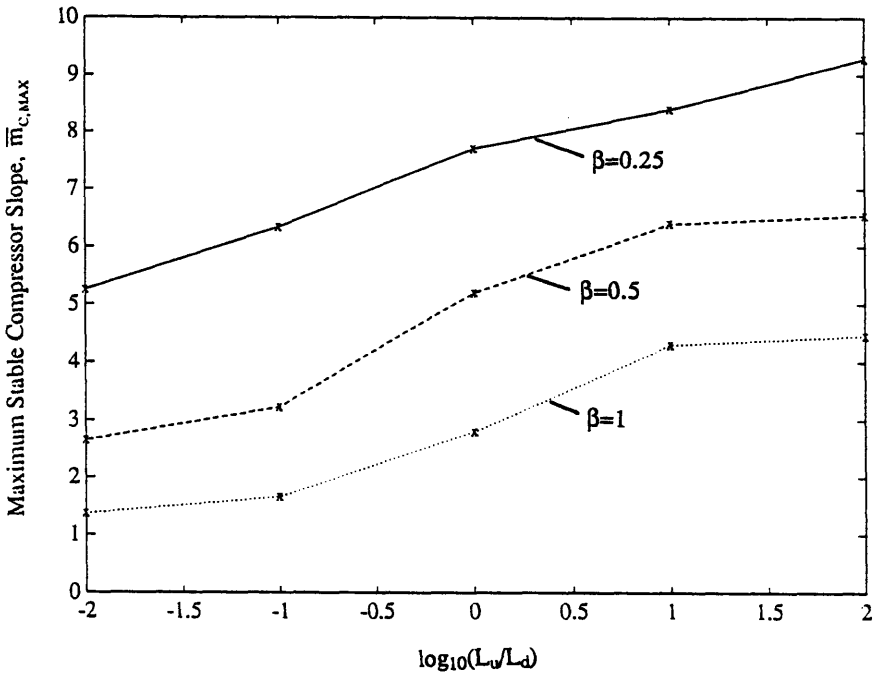

Figure 3.16: Maximum Stable Compressor Slope for the Flow-Fence Valve with Compressor Mass Flow Sensor as a Function of the Stability Parameter and Inertia Ratio: $\omega_C/\omega_H=3$, $-2.5<K_N<2.5$, $\theta_B=2$, LTS-101 Ch'ic.

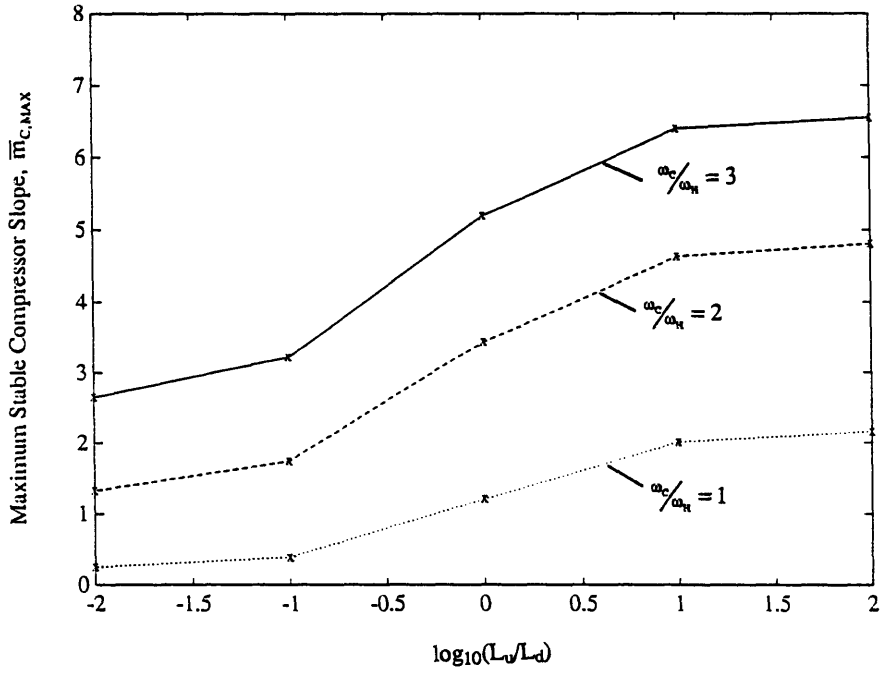

Figure 3.17: Maximum Stable Compressor Slope for the Flow-Fence Valve with Compressor Mass Flow Sensor as a Function of the Controller Bandwidth and Inertia Ratio: $\beta=0.5$, $-2.5<K_N<2.5$, $\theta_B=2$, LTS-101 Ch'ic.

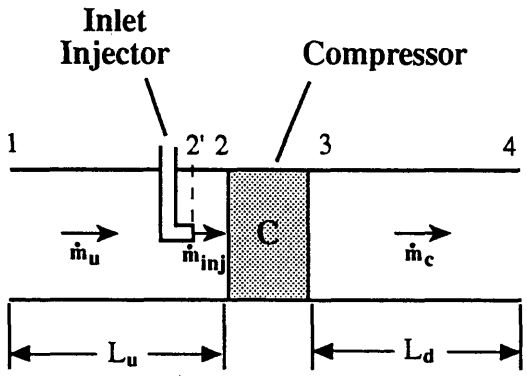

Figure 3.18: Schematic of Compressor Inlet Injection Actuator.

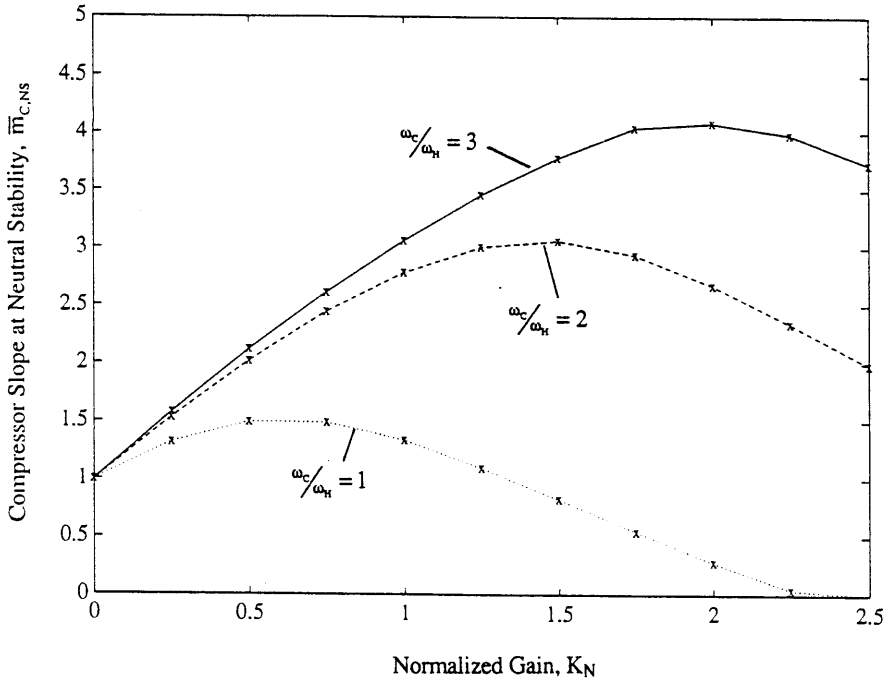

Figure 3.19: Closed-Loop Stability for Compressor Inlet Injection with Compressor Mass Flow Sensor (W_C) as a Function of Controller Bandwidth (ω_C/ω_H) and Gain (K_N): β=0.4, L_u/L_d=0.4, θ_B=2, LTS-101 Ch'ic, $P^*_{O,inj}$=2.

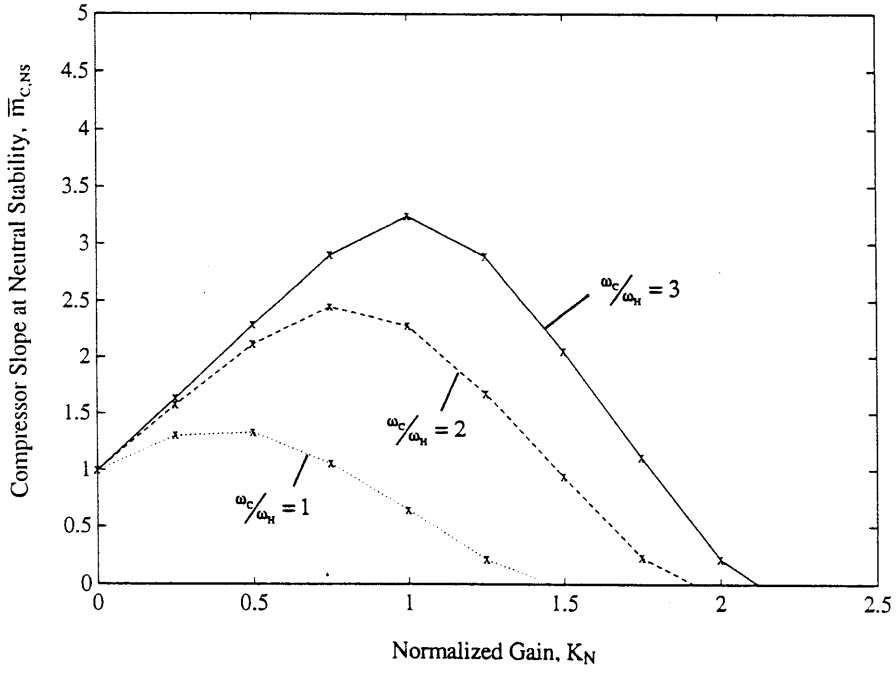

Figure 3.20: Closed-Loop Stability for Compressor Inlet Injection with Upstream Duct Mass Flow Sensor (W_u) as a Function of Controller Bandwidth (ω_C/ω_H) and Gain (K_N): β=0.4, L_u/L_d=0.4, θ_B=2, LTS-101 Ch'ic, $P^*_{O,inj}$=2.

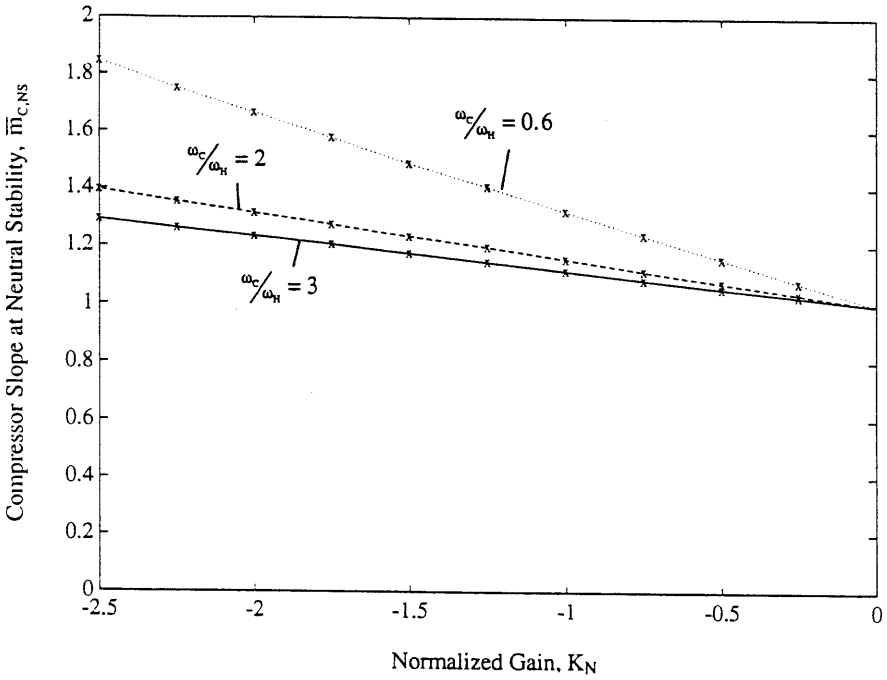

Figure 3.21: Closed-Loop Stability for Compressor Inlet Injection with Burner Pressure Sensor (P^*_B) as a Function of Controller Bandwidth (ω_C/ω_H) and Gain (K_N): β=0.4, L_u/L_d=0.4, θ_B=2, LTS-101 Ch'ic, $P^*_{O,inj}$=2.

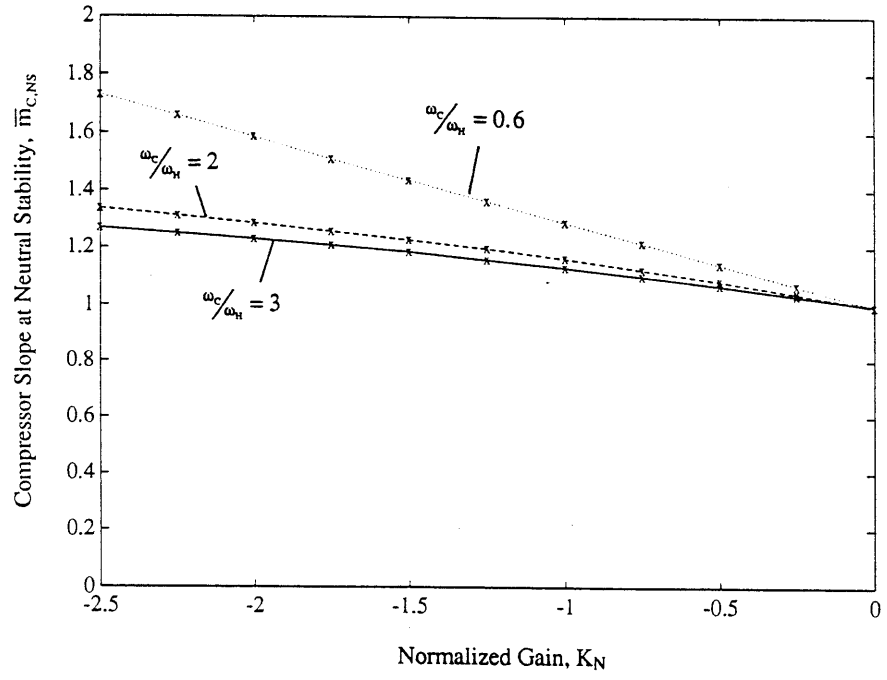

Figure 3.22: Closed-Loop Stability for Compressor Inlet Injection with Inlet Total Pressure Sensor ($P^*_{O,2'}$) as a Function of Controller Bandwidth (ω_C/ω_H) and Gain (K_N): β=0.4, L_u/L_d=0.4, θ_B=2, LTS-101 Ch'ic, $P^*_{O,inj}$=2.

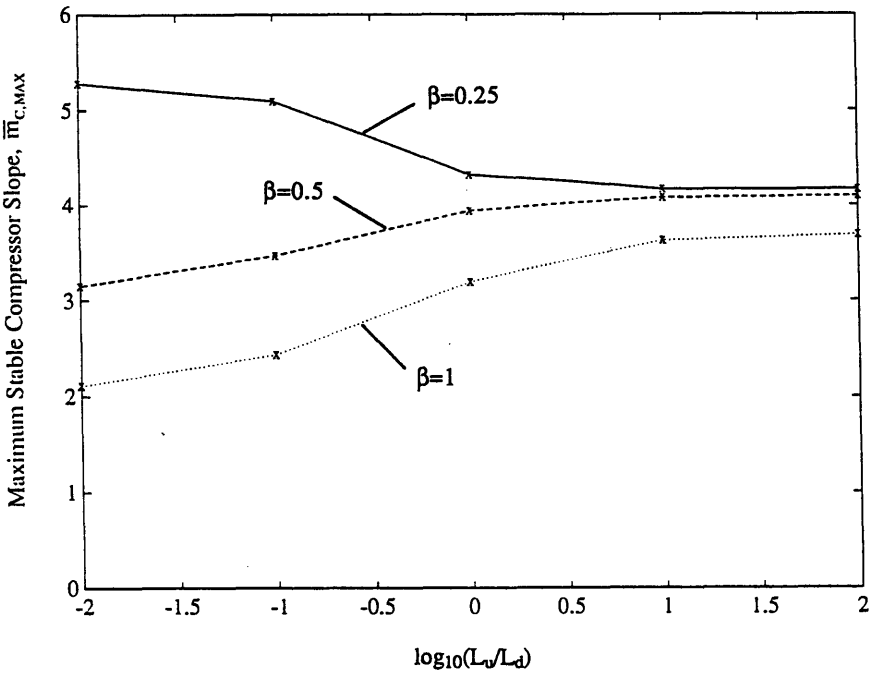

Figure 3.23: Maximum Stable Compressor Slope for Compressor Inlet Injection with Compressor Mass Flow Sensor as a Function of the Stability Parameter and Inertia Ratio: ω_C/ω_H=3, -2.5<K_N<2.5, θ_B=2, LTS-101 Ch'ic, $P^*_{O,inj}$=2.

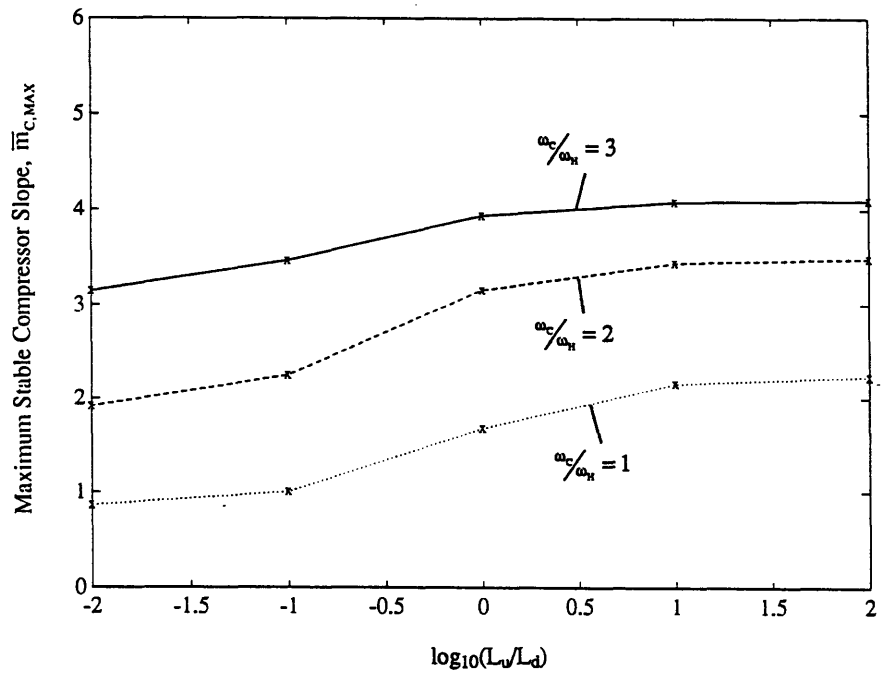

Figure 3.24: Maximum Stable Compressor Slope for Compressor Inlet Injection with Compressor Mass Flow Sensor as a Function of the Controller Bandwidth and Inertia Ratio: β=0.5, -2.5<K_N<2.5, θ_B=2, LTS-101 Ch'ic, $P^*_{O,inj}$=2.

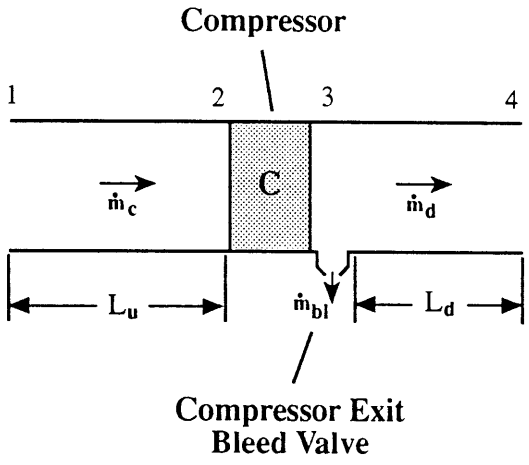

Figure 3.25: Schematic of Compressor Exit Bleed Actuator.

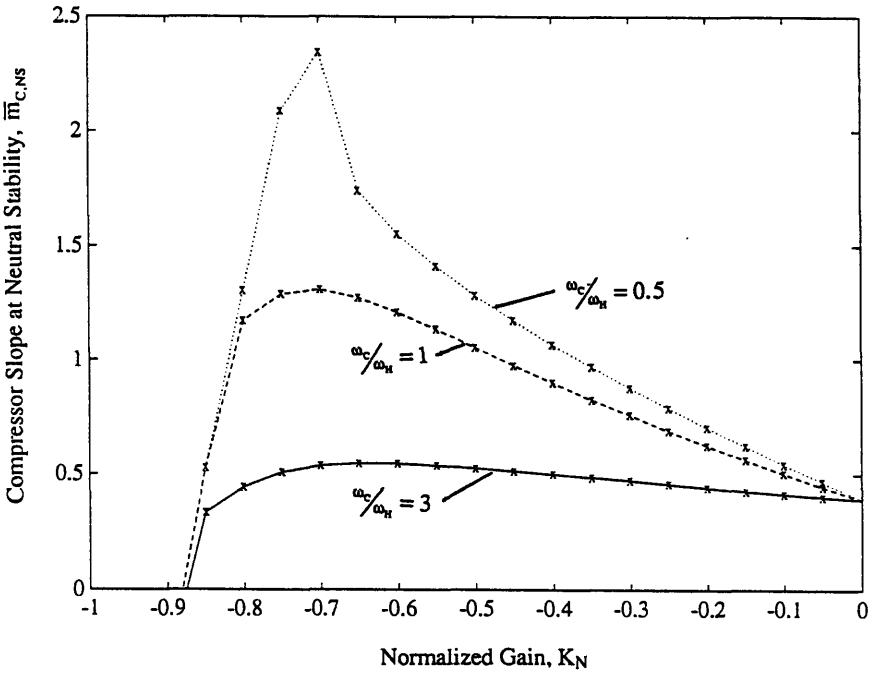

Figure 3.26: Closed-Loop Stability for Compressor Exit Bleed with Compressor Mass Flow Sensor (W_C) as a Function of Controller Bandwidth (ω_C/ω_H) and Gain (K_N): β=0.4, L_u/L_d=0.4, θ_B=2, LTS-101 Ch'ic.

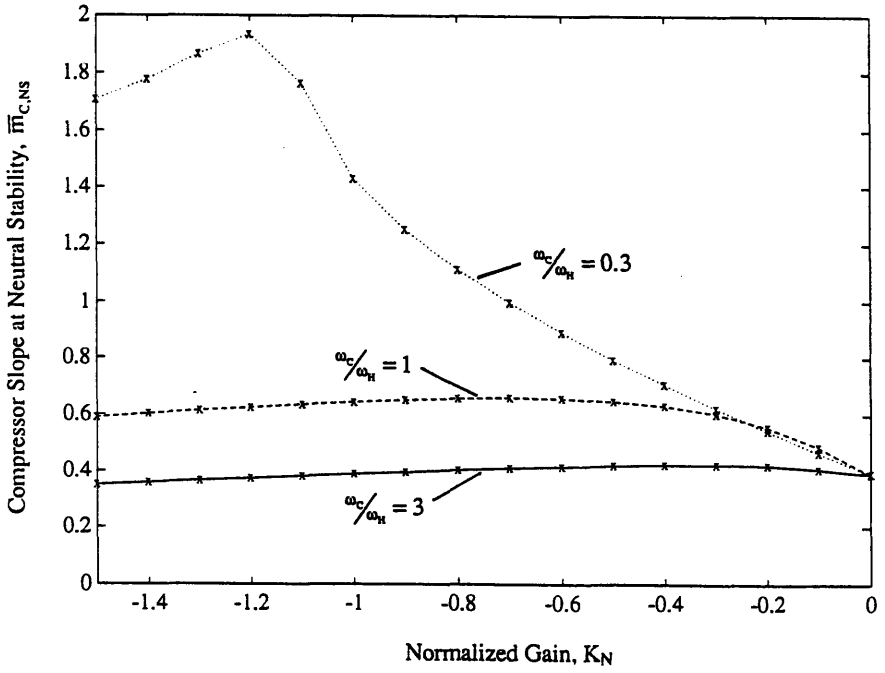

Figure 3.27: Closed-Loop Stability for Compressor Exit Bleed with Downstream Duct Mass Flow Sensor (W_d) as a Function of Controller Bandwidth (ω_C/ω_H) and Gain (K_N): β=0.4, L_u/L_d=0.4, θ_B=2, LTS-101 Ch'ic.

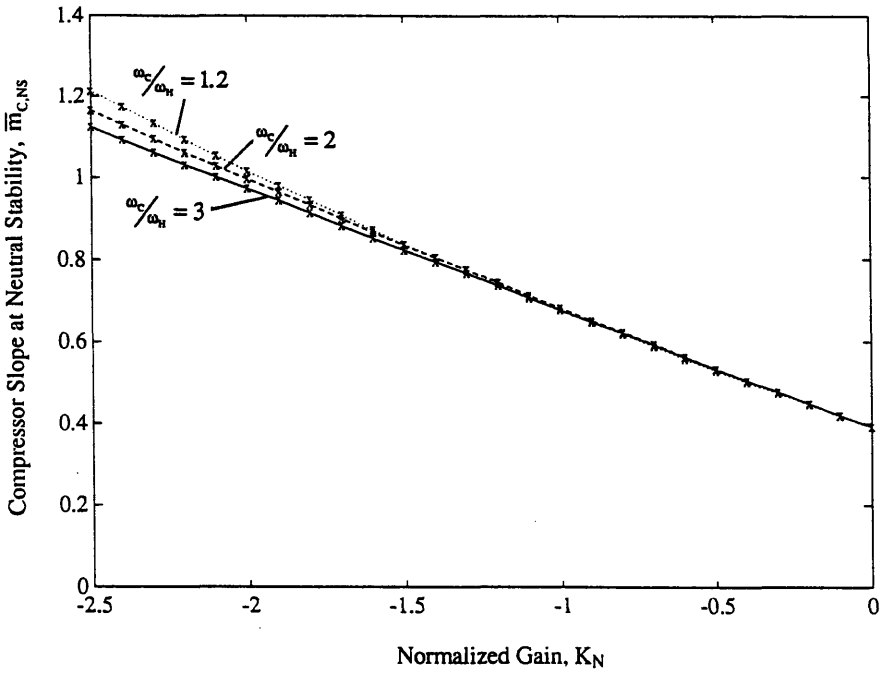

Figure 3.28: Closed-Loop Stability for Compressor Exit Bleed with Burner Pressure Sensor (P^*_B) as a Function of Controller Bandwidth (ω_C/ω_H) and Gain (K_N): β=0.4, L_u/L_d=0.4, θ_B=2, LTS-101 Ch'ic.

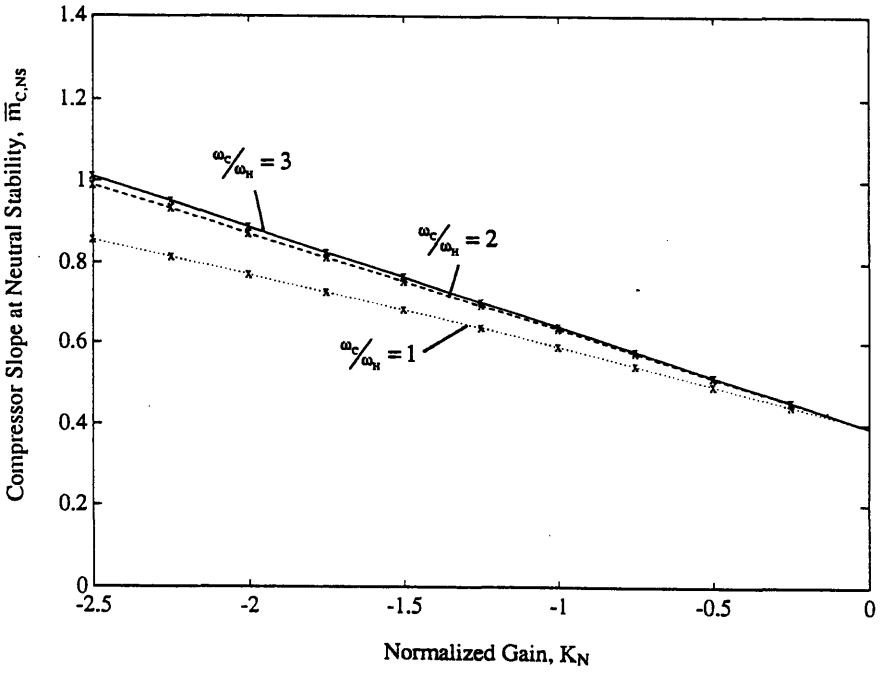

Figure 3.29: Closed-Loop Stability for Compressor Exit Bleed with Inlet Total Pressure Sensor ($P^*_{O,2}$) as a Function of Controller Bandwidth (ω_C/ω_H) and Gain (K_N): β=0.4, L_u/L_d=0.4, θ_B=2, LTS-101 Ch'ic.

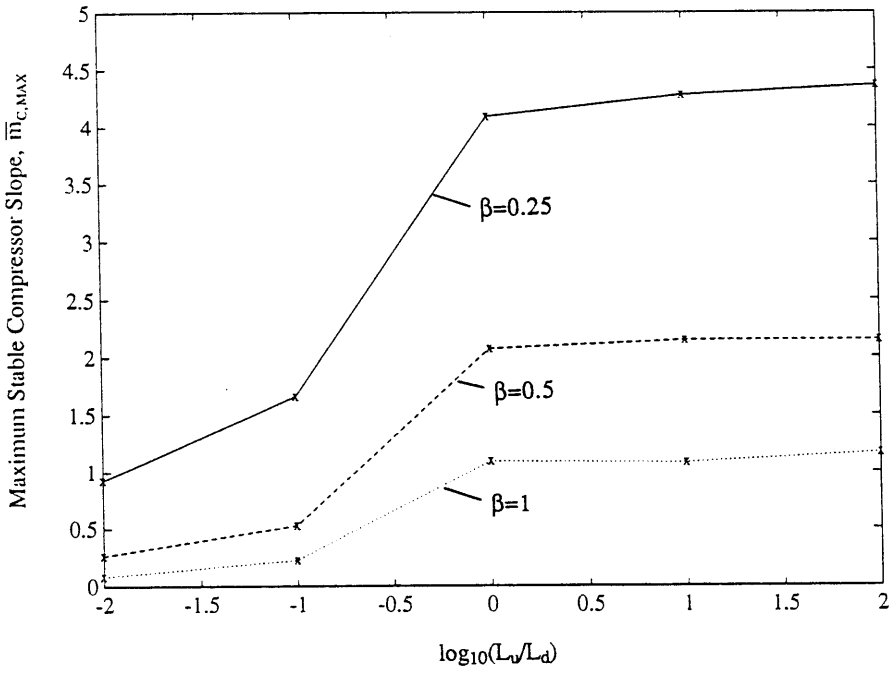

Figure 3.30: Maximum Stable Compressor Slope for Compressor Exit Bleed with Compressor Mass Flow Sensor as a Function of the Stability Parameter and Inertia Ratio: $(\omega_C/\omega_H)_{opt}$=0.5, -2.5<$K_N$<2.5, θ_B=2, LTS-101 Ch'ic.

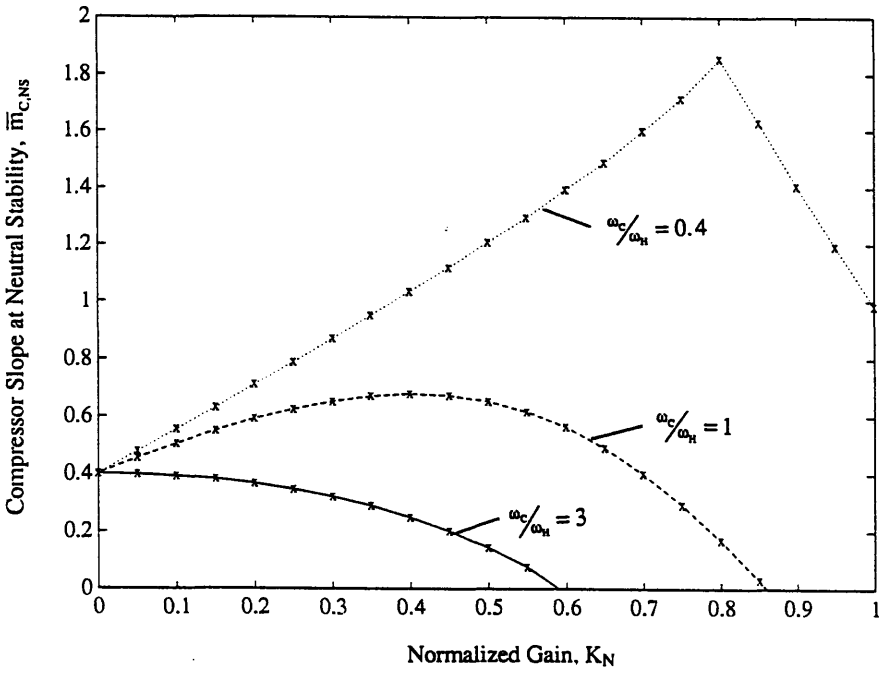

Figure 3.31: Closed-Loop Stability for Fuel-Flow Modulation with Compressor Mass Flow Sensor (W_C) as a Function of Controller Bandwidth (ω_C/ω_H) and Gain (K_N): β=0.4, L_u/L_d=0.4, θ_B=2, LTS-101 Ch'ic.

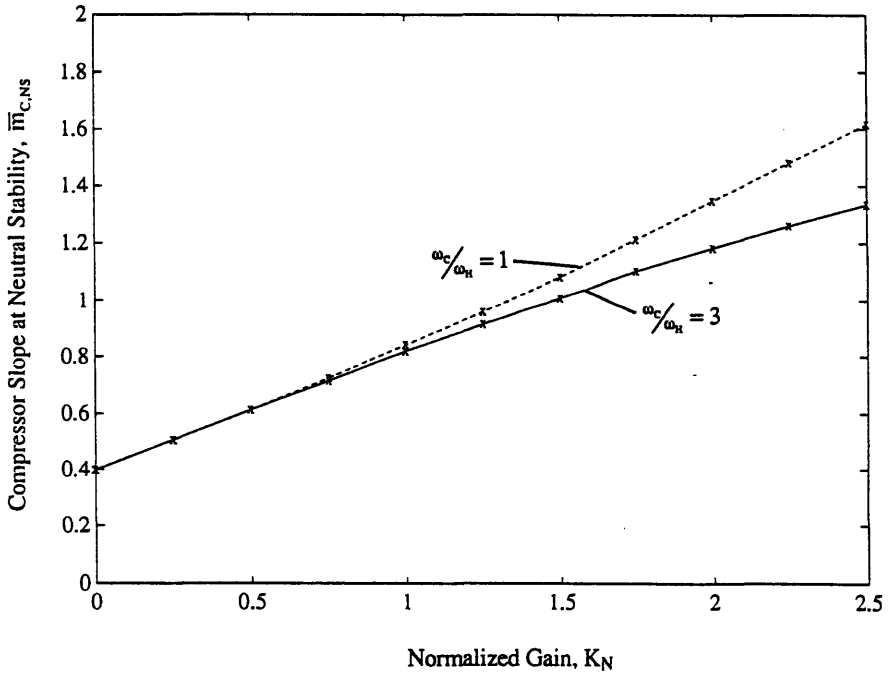

Figure 3.32: Closed-Loop Stability for Fuel-Flow Modulation with Burner Pressure Sensor (P_B^*) as a Function of Controller Bandwidth (ω_C/ω_H) and Gain (K_N): β=0.4, L_u/L_d=0.4, θ_B=2, LTS-101 Ch'ic.

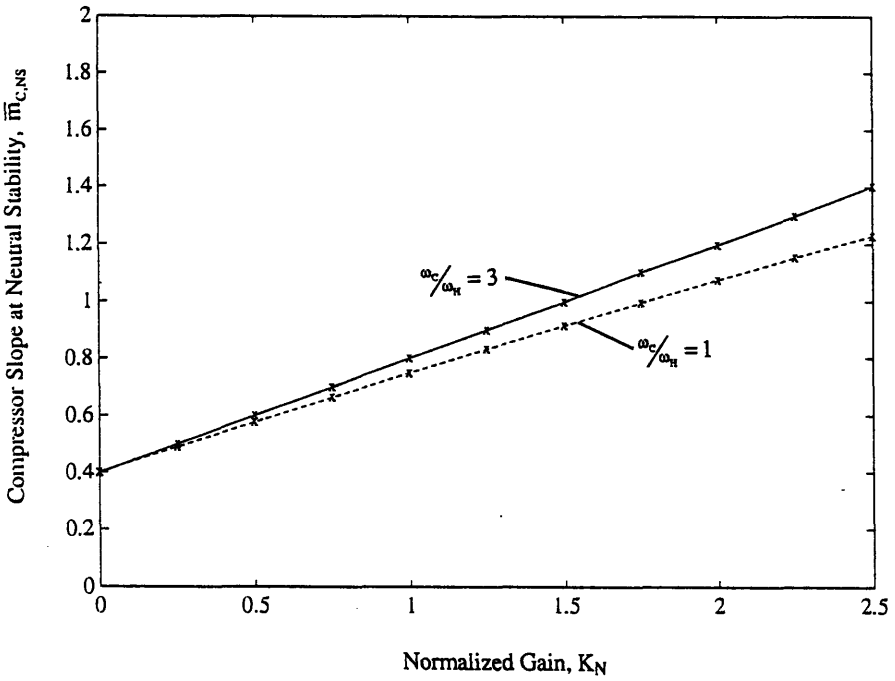

Figure 3.33: Closed-Loop Stability for Fuel-Flow Modulation with Inlet Total Pressure Sensor ($P^*_{O,2}$) as a Function of Controller Bandwidth (ω_C/ω_H) and Gain (K_N): β=0.4, L_u/L_d=0.4, θ_B=2, LTS-101 Ch'ic.

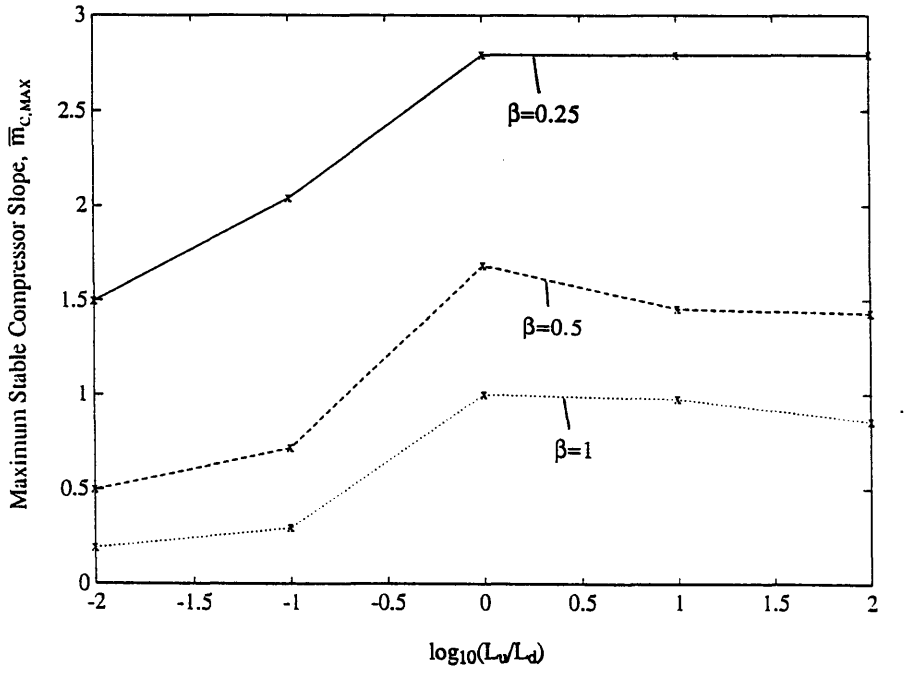

Figure 3.34: Maximum Stable Compressor Slope for Fuel-Flow Modulation with Compressor Mass Flow Sensor as a Function of the Stability Parameter and Inertia Ratio: $(\omega_C/\omega_H)_{opt}$=0.4, -2.5<$K_N$<2.5, θ_B=2, LTS-101 Ch'ic.

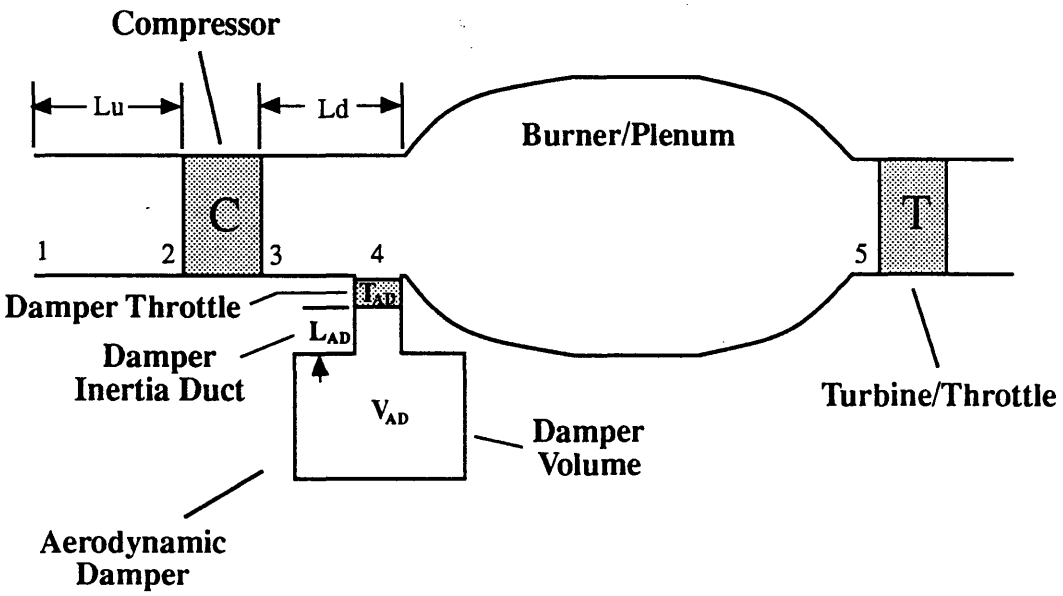

Figure 3.35: Schematic of Aerodynamic Damper Passive Surge Control Strategy.

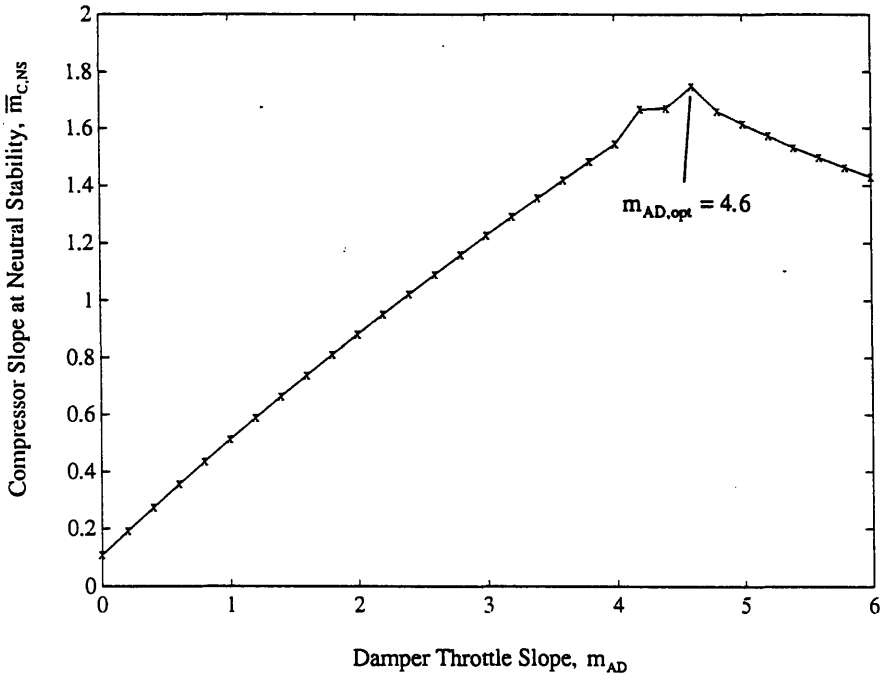

Figure 3.36: Closed-Loop Stability for the Aerodynamic Damper as a Function of the Damper Throttle Slope (m_{AD}): β=0.4, L_u/L_d=0.4, I=0.15, VR_{opt}=1.35, θ_B=2, LTS-101 Ch'ic.

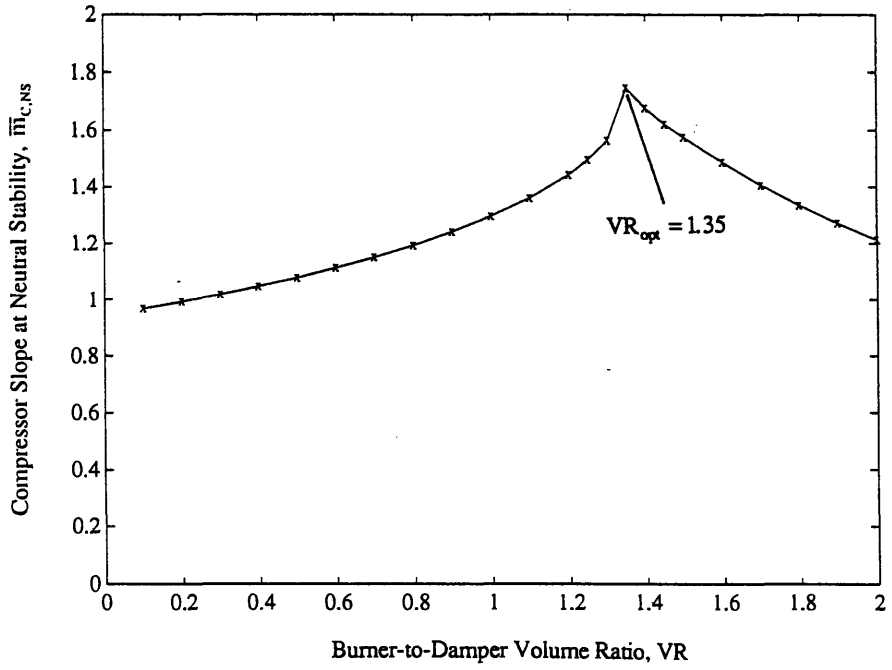

Figure 3.37: Closed-Loop Stability for the Aerodynamic Damper as a Function of the Burner-to-Damper Volume Ratio (VR): β=0.4, L_u/L_d=0.4, I=0.15, $m_{AD,opt}$=4.6, θ_B=2, LTS-101 Ch'ic.

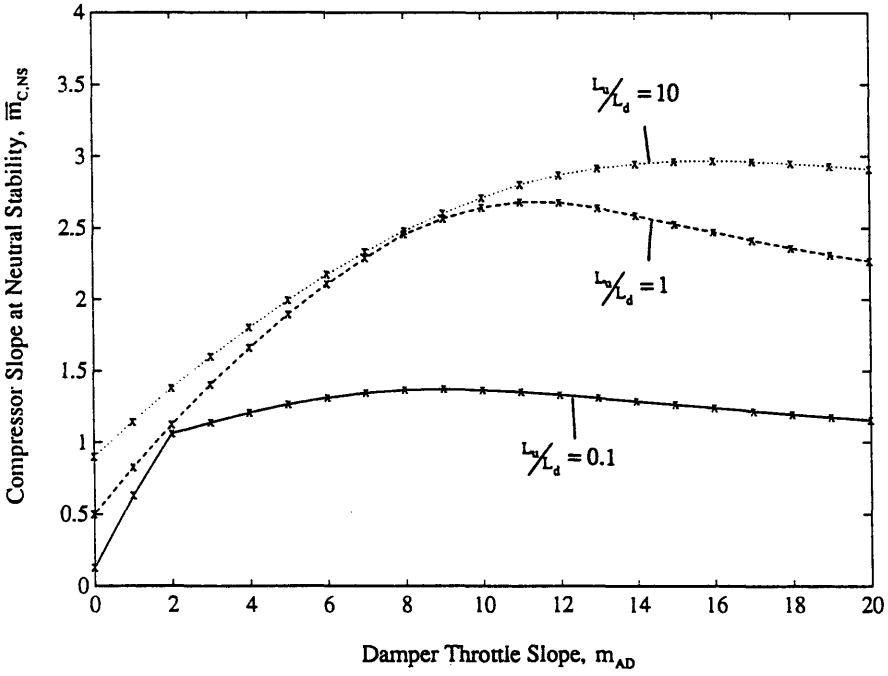

Figure 3.38: Closed-Loop Stability for the Aerodynamic Damper as a Function of the Damper Throttle Slope and Inertia Ratio: β=0.25, I=0.15, VR=1.35, θ_B=2, LTS-101 Ch'ic.

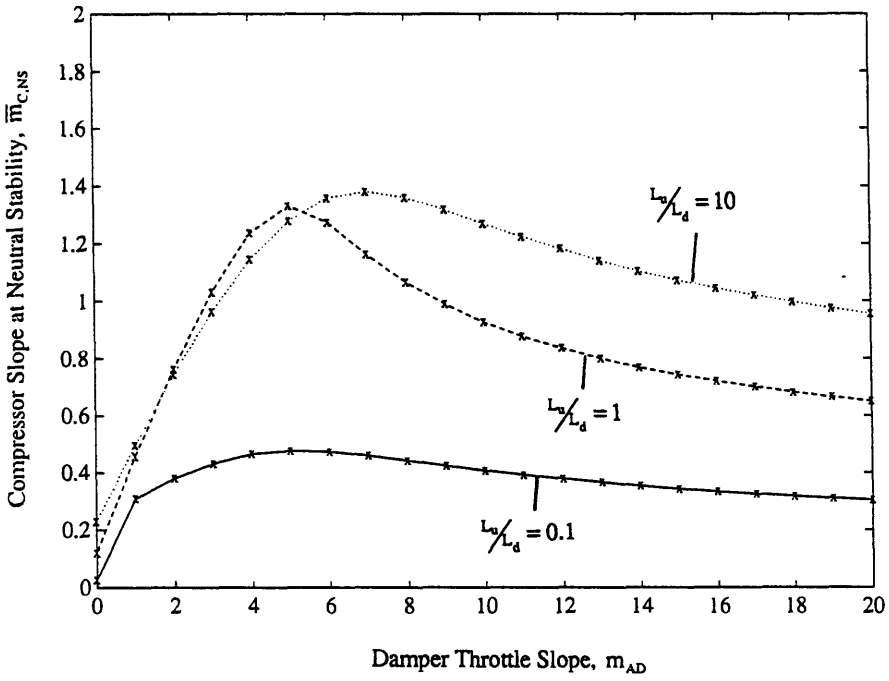

Figure 3.39: Closed-Loop Stability for the Aerodynamic Damper as a Function of the Damper Throttle Slope and Inertia Ratio: β=0.5, I=0.15, VR=1.35, θ_B=2, LTS-101 Ch'ic.

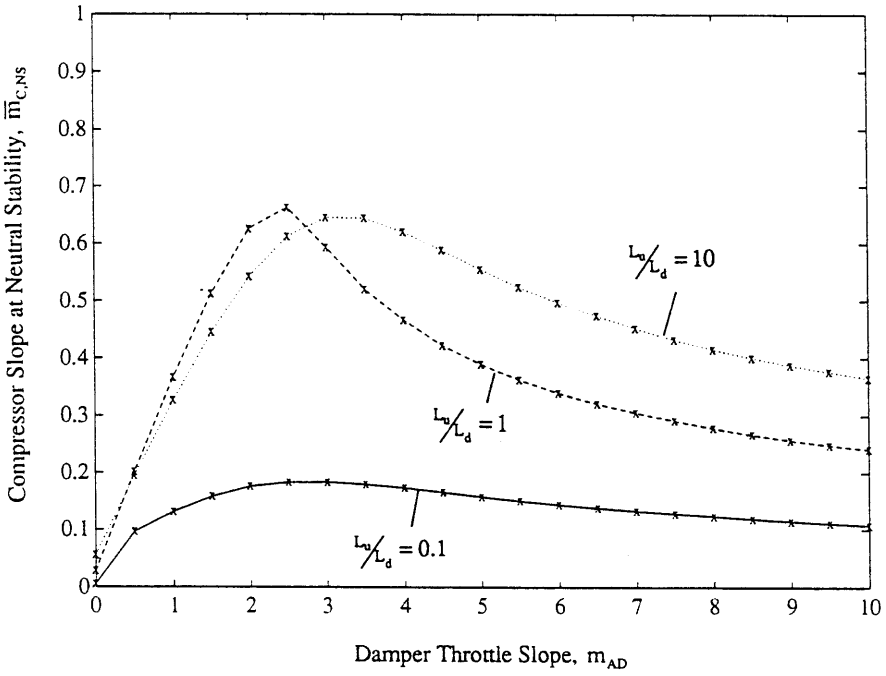

Figure 3.40: Closed-Loop Stability for the Aerodynamic Damper as a Function of the Damper Throttle Slope and Inertia Ratio: β=1.0, I=0.15, VR=1.35, θ_B=2, LTS-101 Ch'ic.

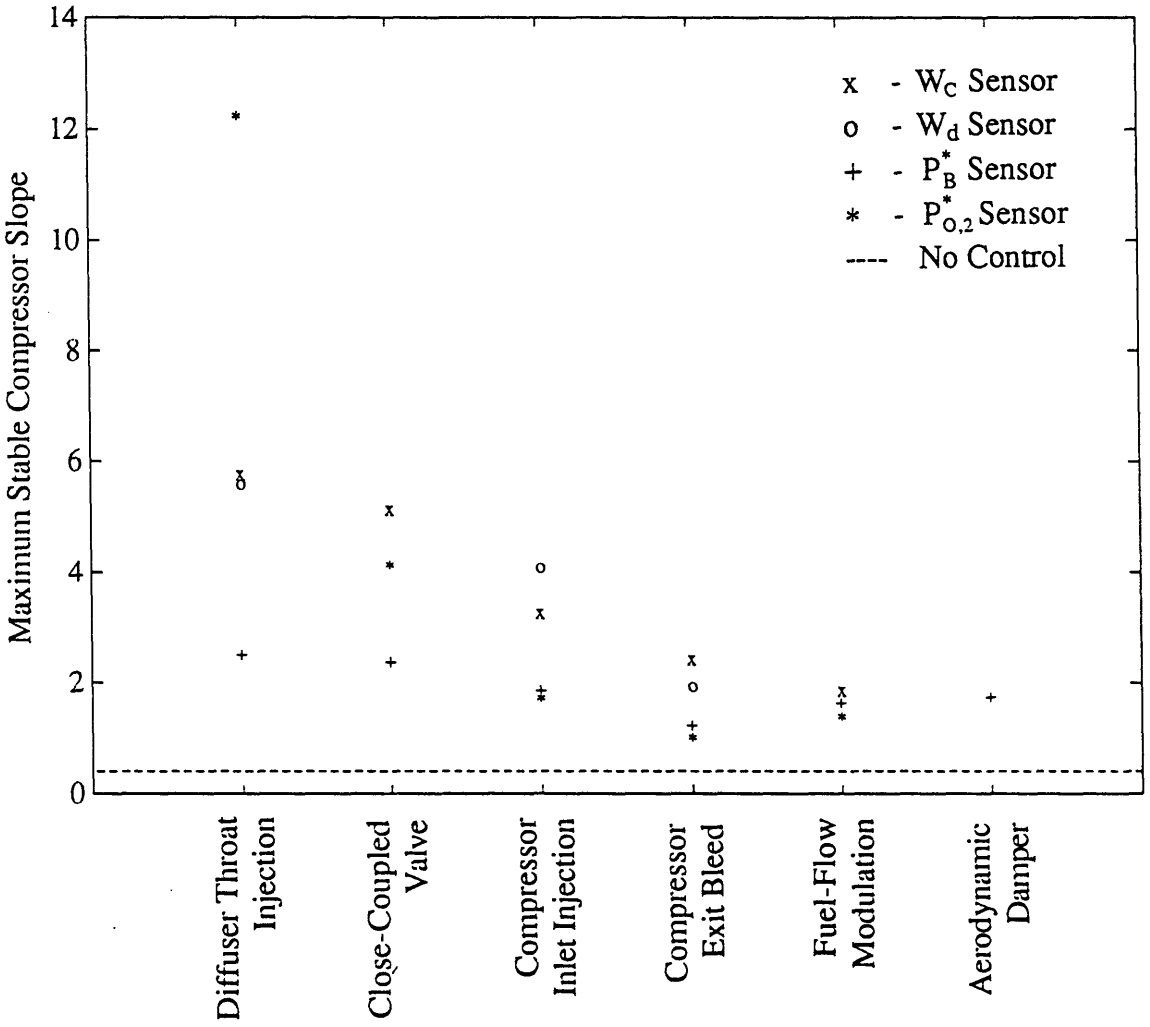

Figure 3.41: Summary of Actuator/Sensor Performance for LTS-101 Surge Model Parameters: β=0.4, L_u/L_d=0.4, θ_B=2, LTS-101 Ch'ic.

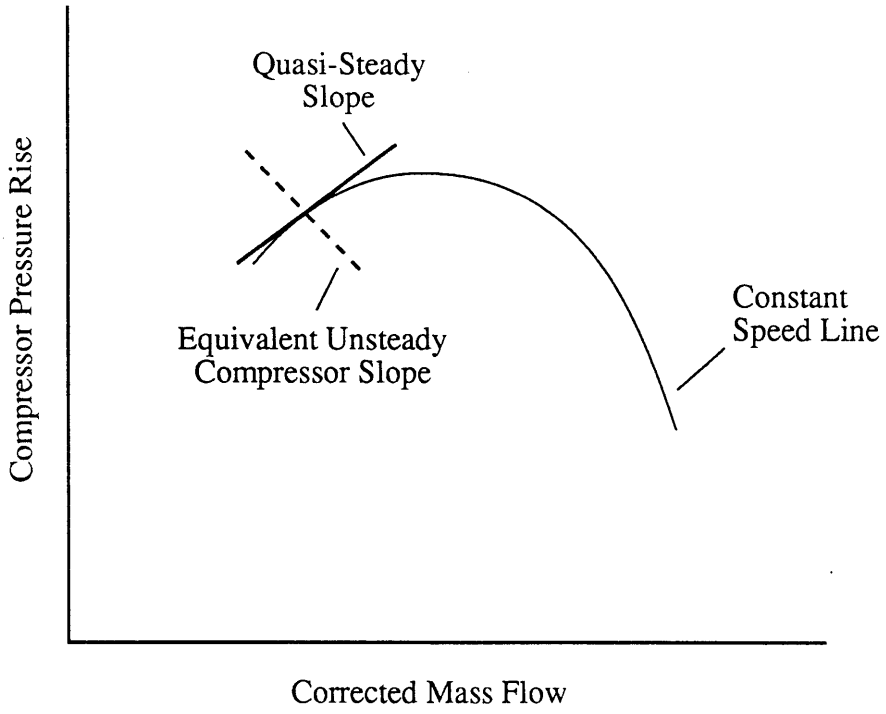

Figure 3.42: Illustration of the Effect of Close-Coupled Flow Momentum Actuation with Mass Flow Sensing on the Equivalent Unsteady Compressor Slope.

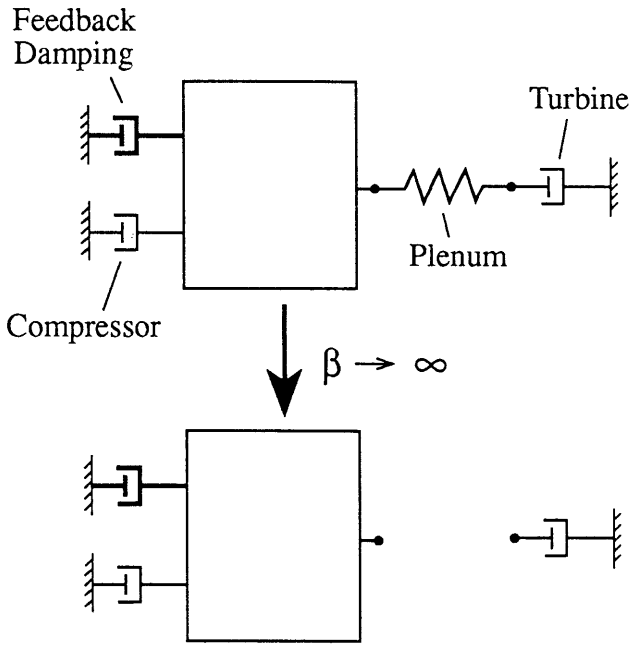

Close-Coupled Feedback is Still Effective

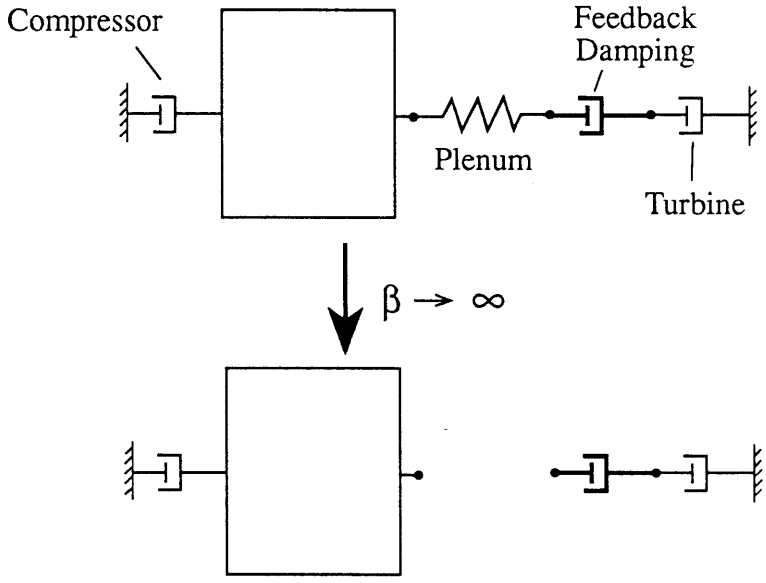

Non Close-Coupled Feedback is Ineffective

Figure 3.43: Mechanical Analogy Illustrating the Advantage of Close-Coupled Control at Large Stability Parameters (Compliance/Inertia).

Chapter 4
Summary and Conclusions

The summary and conclusions are divided into two sections: (a) results pertaining to the basic engine with no control and (b) results of the closed-loop actuator/sensor study.

4.1 Summary of Engine Stability Behavior with No Control

A lumped parameter model of a gas turbine engine has been developed. The criteria that must be satisfied for the lumped parameter approximations to hold were examined in some detail. A crucial assumption is related to the negligence of compliance in the compressor duct which depends on the characteristic length scales and wavelengths of the unsteadiness. For the LTS-101 engine examined these assumptions may be adequate for the open-loop dynamics; however, if high frequency actuators are placed in the engine to modify the dynamics, the modelling assumptions may break down.

The impact of phenomena in the engine environment on surge inception were examined, including the effects of compressor pressure ratio, density fluctuations at the compressor inlet due to upstream inertia, non-isentropic processes in the combustor, and rotor speed fluctuations due to compressor/turbine shaft dynamics. The main conclusions drawn from this analysis were:

- Increasing the compliance-to-inertia ratio (i.e. decoupling the turbine from the compressor) has a strong destabilizing influence on engine stability.
- Increasing the ratio of the upstream-to-dowstream inertia, L_u/L_d, has a stabilizing influence on engine stability, with the effect becoming stronger at high compressor pressure ratios.

- For values of steady-state heat addition and compressor temperature slope expected in a helicopter engine, the effect of non-isentropic processes in the combustor significantly destabilizes the engine.
- Rotor speed fluctuations due to compressor/turbine shaft dynamics have a negligible effect on engine stability for practical values of the rotor inertia.

4.2 Summary of Actuator/Sensor Study

The lumped parameter engine model was used to evaluate several dynamic surge control strategies. The following actuators were studied: diffuser throat injection, a close-coupled valve (flow-fence), compressor inlet injection, compressor exit bleed, fuel-flow modulation and a passive aerodynamic damper. The sensors examined were compressor duct mass flow, burner pressure, and compressor inlet total pressure. A stability analysis of each actuator/sensor pair was performed using the compression system parameters estimated for the LTS-101 helicopter engine. Constraints on controller bandwidth and gain were imposed to simulate practical limitations in both actuator technology and control authority. The conclusions of the study were:

- The most effective actuation approaches were those close-coupled to the compressor which modulate the flow momentum in the duct. In decreasing order of effectiveness, these were diffuser throat injection, a close-coupled valve and compressor inlet injection.
- The most promising control scheme was diffuser throat injection with inlet total pressure sensing, achieving compressor slopes of over 12. Diffuser throat injection with compressor mass flow sensing achieved a slope of roughly 6.
- The close-coupled valve and inlet injection actuators achieved compressor slopes in the range of 4 to 5 with a compressor mass flow sensor.
- Compressor exit bleed was not as effective, attaining compressor slopes of about 2.5 using a mass flow sensor.

- Fuel-flow modulation and the passive aerodynamic damper, both of which actuate in the downstream plenum, achieved compressor slopes of approximately 2.
- The performance of some actuator/sensor combinations improved as the controller bandwidth was decreased to some optimum level.

In summary, the analysis indicates that several dynamic surge control strategies have been identified which appear to be feasible for implementation in an existing gas turbine engine.

4.3 Recommendations for Future Research

There are several research areas that should further contribute to the goal of demonstrating dynamic control in a helicopter gas turbine engine. First and foremost, more complete high response surge inception data should be taken on the helicopter engines in the Gas Turbine Laboratory. The data should be used to determine the role of rotating stall in the surge inception process of a high pressure ratio centrifugal compressor with a vaned-diffuser. This is important in assessing the validity of one-dimensional modelling, actuation and sensing approaches.

The transfer function of both engines also should be measured to assess the validity of the lumped parameter model developed in this thesis. A more effective forcing method than the compressor exit bleed valve used by Bell [9] is needed to overcome the high noise levels in an operating engine; both mass flow and pressures in the engine should be measured. If the engine dynamics are found to be distributed, rather than lumped, for the frequencies of interest, an accurate transfer function of the compressor alone would be useful for the design of *close-coupled* actuation and sensing approaches.

There is also much to be done in the development of a control strategy. The analyses in this thesis indicate that further experimental study of close-coupled actuators that modulate the flow momentum is warranted. The diffuser throat injection scheme is the most promising. As a first step, the effect of steady-state mass injection, or bleed, at the

diffuser throat in the engine should be measured to give an idea of the effectiveness of this approach. Any experimental demonstration of close-coupled control strategies should measure, and attempt to minimize, any steady-state performance penalties (i.e. pressure drop, mass bleed or injection) associated with the active control.

Another area that can yield significant gains in control performance is the development of high bandwidth actuators. The effectiveness of the closed-coupled actuators that modulate the flow momentum using mass flow sensing was shown to increase significantly as controller bandwidth is increased.

The results of this study using proportional control indicates that more sophisticated control laws should be investigated for the actuator/sensor combinations that performed well with low controller bandwidths. There is a possibility that the performance of these schemes can be improved if the restriction to proportional control is removed.

Finally, due to the simplicity and low cost of the aerodynamic damper passive control scheme, it is recommended that this approach be implemented on one of the helicopter engines in the Gas Turbine Laboratory. The analysis predicts that a properly tuned damper can stabilize the engine to compressor slopes of approximately 2. Such an experiment would determine the effectiveness of the simplest possible dynamic control strategy as well as reveal information on the "steepness" of the compressor speedlines in the nominally unstable flow regime.

References

1. Epstein, A.H., Ffowcs Williams, J.E., Greitzer, E.M., "Active Suppression of Aerodynamic Instabilities in Turbomachines," *AIAA J. of Propulsion and Power*, Vol. 5, No. 2, March-April 1989, pp. 204-211.

2. Ffowcs Williams, F.E., Huang, X., "Active Stabilization of Compressor Surge," *Journal of Fluid Mechanics*, Vol. 204, 1989, pp. 245-262.

3. Pinsley, J.E., et al., "Active Stabilization of Centrifugal Compressor Surge," ASME Paper 90-GT-123, 1990.

4. Gysling, D., Dugundji, J., Greitzer, E.M., Epstein, A.H., "Dynamic Control of Centrifugal Compressor Surge Using Tailored Structures," *ASME J. of Turbomachinery*, Vol. 113, No. 4, 1991, pp. 710-722.

5. Simon, J.S., "Feedback Stabilization of Compression Systems," MIT Gas Turbine Laboratory Report No. 216, 1993.

6. Paduano, J.D., et al., "Active Control of Rotating Stall in a Low-Speed Axial Compressor," *ASME J. of Turbomachinery*, Vol. 115, No. 1, Jan. 1993, pp. 48-56.

7. Haynes, J.M., Hendricks, G.J., Epstein, A.H., "Active Stabilization of Rotating Stall in a Three-Stage Axial Compressor," ASME Paper No. 93-GT-346.

8. Gysling, D., "Dynamic Control of Rotating Stall in an Axial Compressor using Aeromechanical Feedback," Ph.D. Thesis, Department of Aeronautics and Astronautics, MIT, 1993.

9. Bell, J.T., "Measurements of Forced and Unforced Aerodynamic Disturbances in a Turbojet Engine," M.S. Thesis, Department of Aeronautics and Astronautics, MIT, 1993.

10. Borror, S., "Dynamic Control of Compressor Surge in a Gas Turbine Engine," M.S. Thesis, Department of Aeronautics and Astronautics, MIT, 1994.

11. Lothore, Y., Research Report regarding Dynamic Surge Control in a Gas Turbine Engine, Department of Aeronautics and Astronautics, MIT, 1994.

12. Emmons, A.W., Pearson, C.E., Grant, H.P., "Compressor Surge and Stall Propagation," *Trans. ASME*, Vol. 79, April 1955, pp. 455-469.

13. Greitzer, E.M., "Surge and Rotating Stall in Axial Flow Compressors, Parts I and II", *ASME J. for Eng. for Power*, Vol. 98, April 1976, pp. 190-217.

14. Fink, D.A., "Surge Dynamics and Unsteady Flow Phenomena in Centrifugal Compressors," MIT Gas Turbine Laboratory Report No. 193, 1988.

15. Lavrich, P.L., "Instability and Rotating Stall in High Speed Axial Flow Compression Systems," M.S. Thesis, Department of Aeronautics and Astronautics, MIT, 1985.

16. Mani, R., "Compressor Post Stall Operation," Lecture Notes from AIAA Professional Study on Airbreathing Propulsion, Gordon C. Oates, course director, June 1982.

17. Kuhlberg, J.F., Sheppard, D.E., King, E.O., Baker, J.R., "Dynamic Simulation of Turbine Engine Compressors," AIAA Paper 69-486, June 1969.

18. Tesch, W.A., Steenken, W.G., "Dynamic Blade Row Compression Component Model for Stability Studies," AIAA Paper 76-203, January 1976.

19. Hendricks, G.J., et. al.,"Analysis of Rotating Stall Onset in High Speed Axial Flow Compressors," AIAA Paper 93-2233.

20. Bonnaure, L.P., "Modelling High Speed Multistage Compressor Stability," M.S. Thesis, Department of Aeronautics and Astronautics, MIT, 1991.

21. Greitzer, E.M., "The Stability of Pumping Systems-The 1980 Freeman Scholar Lecture," *ASME J. of Fluids Eng.*, Vol. 103, June 1981, pp. 193-242.

22. Ffowcs Williams, J.E., Graham, W.R., "An Engine Demonstration of Active Surge Control," ASME Paper 90-GT-224.

23. Ffowcs Williams, J.E., Harper, M.F.L., Allwright, D.J., "Active Stabilization of Compressor Instability and Surge in a Working Engine," *Trans. of the ASME*, Vol. 115, January 1993, pp. 68-75.

24. Eveker, K.M., Nett, C.N., "Model Development for Active Surge Control/ Rotating Stall Avoidance in Aircraft Gas Turbine Engines," *Proc. of the American Control Conf.*, March 1991.

25. Hosny, W.M., Leventhal, L., Steenken, W.G., "Active Stabilization of Multi-Stage Axial-Compressor Aerodynamic System Instabilities," ASME Paper 91-GT-403, 1991.

26. Escuret, J.F., Elder, R.L., "Active Control of Surge in Multi-Stage Axial-Flow Compressors," ASME Paper 93-GT-39, 1993.

27. Day, I.J., "Active Suppression of Rotating Stall and Surge in Axial Compressors," *Trans. of the ASME*, Vol. 115, January, 1993, pp. 40-47.

28. Greitzer, E.M., Waitz, I.A., Class Notes from MIT Course 16.543 -- "Internal Flows in Turbomachinery," Spring 1992.

29. Cohen, H., Rogers, G.F.C., Saravanamuttoo, H.I.H., "Prediction of Performance of Simple Gas Turbines," Ch. 8 in *Gas Turbine Theory*, 3rd Ed., Longman Scientific and Technical Publications, 1987.

30. Bathie, W.W., "Component Matching," Ch. 10 in *Fundamentals of Gas Turbines*, John Wiley & Sons, Inc., 1984.

31. Szanca, E.M., Schum, H.J, "Experimental Determination of Aerodynamic Performance," Ch. 12 in *Turbine Design and Application*, Vol. 3, Arthur J. Glassman, Editor, NASA Special Publication SP-290, 1975.

32. Zucrow, M.J., Hoffman, J.D., Chapter 3 in *Gas Dynamics*, Vol. 1, John Wiley & Sons, Inc., 1976.

33. Dowling, A.P., Ffowcs Williams, J.E., "Resonators--from Bubbles to Reverberant Chambers," Ch. 6 in *Sound and Sources of Sound*, Ellis Horwood Limited, 1983.

34. Hill, P.G., Peterson, C.R., "Axial Compressors," Ch. 7 in *Mechanics and Thermodynamics of Propulsion*, Addison-Wesley Publishing Co., 1992, pp. 288-294.

35. Runstadler, P.W., Jr., Dolan, F.X., Dean, R.C., Jr., "Diffuser Data Book," Creare Technical Note TN-186, May 1975.

36. Wilson, D.G., "Diffusion and Diffusers," Ch. 4 in *The Design of High-Efficiency Turbomachinery and Gas Turbines*, The MIT Press, 1984.

37. Lawless, P.B., Fleeter, S., "Prediction of Active Control of Subsonic Centrifugal Compressor Rotating Stall," AIAA Paper No. 93-0153, 1993.

38. Abramovich, G.N., Chapter 12 in *The Theory of Turbulent Jets*, The MIT Press, 1963.

39. Simon, J.S., Personal Communication, 1992.

40. Kaplan, W., Ch. 2 in *Advanced Calculus*, 3rd Ed., Addison-Wesley Publishing Co., 1984.

41. Gysling, D., Personal Communication, 1992.

Appendix A
Estimation of Surge Model Parameters

In this appendix the method used to estimate the surge model parameters from an engine geometry is discussed and values are estimated for a Lycoming LTS-101 helicopter engine. Some of the issues involved with the estimation of model parameters for high pressure ratio compressors are discussed. The lumped parameter modelling assumptions are also assessed for the LTS-101 engine using the estimated parameters. The goal is to size the model parameters so that the same dynamic response as the real system is obtained.

A.1 Equivalent Model Inertia

To understand the method used to calculate the model geometry from an engine, the derivation of the momentum equation (previously given in Chapter 2) is presented. The problem is illustrated in Fig. A.1 by a variable area duct with a compressor operating in it. The compressor creates a density rise in the duct (the density can increase by as much as a factor of 4 in a helicopter engine). In the actual engine the density, velocity and area are all functions of axial distance, x, whereas, in the model the compressor duct is represented as being of constant area (see Fig. A.1). The main modelling assumption is that the compliance in the compressor duct, including the compressor, is negligible (i.e. the duct fluid dynamics are well approximated as an incompressible flow). The mass flow is thus viewed as being uniform throughout the duct with the density in each duct constant, although a finite density rise across the compressor is allowed.

Upstream Duct:

In Chapter 2 the incompressible form of the momentum equation is use to model the duct fluid dynamics, which was given as:

$$\rho_u \cdot \frac{\partial U_u(x)}{\partial t} = -\frac{\partial P_u(x)}{\partial x} - \frac{\partial(\frac{1}{2} \cdot \rho_u \cdot U_u^2(x))}{\partial x} = -\frac{\partial P_{O,u}(x)}{\partial x} \qquad (2.4)$$

This equation is integrated over the upstream duct assuming ρ_u is constant and using the continuity relation to yield,

$$\int_0^{L_u} \frac{\partial\left(\frac{\rho_u \cdot U_u(x) \cdot A_u(x)}{A_u(x)}\right)}{\partial t} \cdot dx = \int_0^{L_u} \frac{\partial\left(\frac{\dot{m}_u}{A_u(x)}\right)}{\partial t} \cdot dx = P_{O,1} - P_{O,2} \qquad (A.1)$$

Since the mass flow, $\dot{m}_u$, is not a function of x, the left hand side of Eqn. A.1 can be written as

$$\frac{d\dot{m}_u}{dt} \cdot \int_0^{L_U} \frac{1}{A_u(x)} \cdot dx = P_{O,1} - P_{O,2} \qquad (A.2)$$

where the upstream inertia duct length-to-area ratio is thus defined as,

$$\frac{L_u}{A_C} \equiv \int_0^{L_U} \frac{1}{A_u(x)} \cdot dx \qquad (A.3)$$

The engine and model should show similar dynamic behavior provided their equivalent length-to-area ratios are the same and the modelling assumptions are valid.

Downstream Duct:

The conservation of momentum equation for the downstream duct is integrated and manipulated, as done for the upstream duct, to yield

$$\frac{d\dot{m}_d}{dt} \cdot \int_{L_u}^{L_u+L_d} \frac{1}{A_d(x)} \cdot dx = P_{O,3} - P_{O,4} \qquad (A.4)$$

For no internal compliance in the compressor, $\dot{m}_u$ equals $\dot{m}_d$ and one can define the length-to-area ratio for the downstream duct as

$$\frac{L_d}{A_C} \equiv \int_{L_u}^{L_u+L_d} \frac{1}{A_d(x)} \cdot dx \qquad (A.5)$$

The analysis implies that the density rise across the compressor does not affect the calculation of the model duct lengths. This result seems counter-intuitive if one expected

the inertia, and thus duct length, to increase with density. However to obtain the same dynamic response, the product of mass and acceleration must be matched. Although the mass per unit volume increases with density, the velocity, and thus acceleration, must decrease to keep the mass flow constant across the compressor. Thus the two effects, increasing inertia and decreasing acceleration, balance each other so there is no direct effect of density rise on the model duct length calculation. However, we should note that the density variations existing in the actual engine are implicitly accounted for in the flow path geometry.

A.2 Equivalent Model Compliance

The combustor is assumed to behave as the compliance (spring) of the lumped parameter system. To understand how the equivalent model compliance is obtained from the engine geometry the equations governing the combustor dynamics derived in Chapter 2 are rewritten below. The control volume form of the mass conservation equation for the combustor was given as

$$\frac{d\tilde{\rho}_B}{dt} \cdot V_B = \dot{m}_C - \dot{m}_T \qquad (2.17)$$

and the conservation of energy equation as

$$\frac{d(c_V \cdot \tilde{\rho}_B \cdot \tilde{T}_B)}{dt} \cdot V_B = \dot{m}_C \cdot c_P T_{O,4} - \dot{m}_T \cdot c_P T_{O,5} + \dot{Q} \qquad (2.18)$$

In Equations 2.17 and 2.18, $\tilde{\rho}_B$ and $\tilde{T}_B$ are the volumetric average burner density and temperature, repectively, which are defined as

$$\tilde{\rho}_B = \frac{1}{V_B}\int \rho_B \cdot dV \qquad (A.6)$$

$$\tilde{T}_B = \frac{1}{V_B}\int T_B \cdot dV \qquad (A.7)$$

From these equations we see that the model should have the same volume size and flow property distributions as the real engine.

A.3 Estimation of LTS-101 Model Geometry

A cross-section of the LTS-101 engine is shown in Fig. A.2. The engine geometry is divided into 6 distinct regions to allow various duct length and volume combinations to be used according to the different lumping assumptions discussed below. An inlet bellmouth is used on the experimental test engine but is not shown in the figure. The 6 regions of the engine geometry are:

I. Inlet Bellmouth - geometry not shown in Fig. A.2

II. Compressor Inlet - transition ducting from bellmouth to compressor face

III. Compressor - axial stage (rotor and stator) and impeller (rotor only)

IV. Radial Diffuser - vaneless region and vaned-diffuser (r-θ geometry not shown)

V. Transition Duct - ducting from vaned-diffuser exit to combustor inlet

VI. Combustor - combustor inlet to HP turbine inlet

The length-to-area ratio and volumes are estimated for each region of the engine. The flow path was discretized into finite sections to allow an accurate approximation of the geometric integrals with a finite summation. Detailed estimates of the geometry were made except in regions where detailed flow path information was not available. For example, the internal compressor flow path was not available so the flow areas, lengths and volumes were estimated from the cross-section geometry. Table A.1 gives the estimates of the model parameters (L/A and Volume) for each region of the LTS-101 engine. The asterisks mark regions where detailed flow path geometry was not available or was only approximate.

Other relevant engine parameters used in the calculation of the non-dimensional surge model parameters are listed in Table A.2.

Region	L/A [in^{-1}]	V_B [in^3]
I	0.373	2,920
II	0.171*	1,120*
III	0.402*	86.1*
IV	0.843	36.1
V	0.222	139
VI	0.074*	477

Table A.1: LTS-101 Engine Geometry Estimates

Compressor Inlet Flow Area, A_C	18.45 in^2
Impeller Tip Speed, U_{tip}, at N=95%	1751 ft/s
Impeller Tip Mach Number, $M_{tip,a}$, at N=95%	1.57
Speed of Sound in Combustor at N=95% (approximate)	2,137 ft/s

Table A.2: Relevant LTS-101 Engine Parameters

A.4 Estimation of LTS-101 Surge Model Parameters

The engine model of Chapter 2 showed that the engine surge dynamics depends on the stability parameter, β, and the inertia ratio, L_u/L_d. The definition of β is given below for reference:

$$\beta = \frac{1}{\sqrt{\gamma \cdot \overline{T}_B^*}} \cdot \sqrt{\frac{V_B}{(L_u + L_d) \cdot A_C}} = \frac{2 \cdot B}{\sqrt{\gamma} \cdot M_{T,a}} \qquad (2.33)$$

The stability parameter has been expressed as a function of the B parameter [13], which is also calculated for reference.

Another relevant parameter for active control is the system Helmholtz frequency, ω_H, which is rewritten below for convenience.

$$\omega_H = \bar{a}_B \cdot \sqrt{\frac{A_C}{V_B \cdot (L_u + L_d)}} \qquad (2.28)$$

ω_H is a relevant time scale for the linear surge inception oscillations.

From the LTS-101 engine geometry one can see that the boundaries of the "lumped" parameter inertia (characterized by L/A) and compliance elements (characterized by V) are not easy to discern. Therefore, several different sets of assumptions are made in the lumped modelling of the system to try to bracket the actual values of the surge model parameters. The lumping assumptions are listed below, generally in order of decreasing confidence.

1. Inertia duct consists of regions I through V; Plenum volume consists of region VI
2. Inertia duct consists of regions I through V; Plenum volume consists of regions IV through VI
3. Inertia duct consists of regions II through V (no bellmouth); plenum volume consists of region VI
4. Inertia duct consists of regions I through V; Plenum volume consists of regions I through VI (entire engine)
5. Inertia duct consists of regions II through V (no bellmouth); plenum volume consists of regions I through VI (entire engine)

Table A.3 lists the estimates of the surge model parameters from the engine geometry using the various lumping assumptions given above and geometry parameters listed in Table A.2.

The predicted ranges on the surge model parameters is, β between 0.37 and 1.29, B between 0.34 and 1.20, and ω_H between 42 and 146 Hz. The purpose of the different lumping assumptions was to bracket the values of the model parameters. However, assumptions 4 and 5 used the entire engine volume as the compliance volume; which is

dubious considering that the volume downstream of the compressor contains most of the mass stored in the system. The first three assumptions are believed to be more appropriate estimates.

Assumpt.	L/A [in^{-1}]	V_B [in^3]	B	β	ω_H [Hz]
1	2.011	477	0.342	0.368	132
2	2.011	652	0.400	0.431	113
3	1.638	477	0.379	0.408	146
4	2.011	4,778	1.082	1.165	41.6
5	1.638	4,778	1.199	1.291	46.1

Table A.3: Estimates of LTS-101 Surge Model Parameters at 95 Percent Speed

The estimation of the ratio of the upstream-to-downstream inertia, L_u/L_d, requires a different set of assumptions. The various lumping assumptions used, in order of decreasing confidence, are:

1. The upstream inertia duct consists of regions I and II; the downstream inertia duct consists of regions III through V.
2. The upstream inertia duct consists of regions I through III (includes the compressor); the downstream duct consists of regions IV through V.
3. The upstream inertia duct consists of regions I and II; the downstream inertia duct consists of regions IV and V.
4. The upstream inertia duct consists of regions I and II; the downstream inertia duct consists of region V.

Table A.4 presents the estimates for the engine using the different lumping assumptions.

The estimates show that the inertia ratio should be in the range between 0.37 and 2.45. However, the consistency of assumptions 3 and 4 are doubtful because the upstream and downstream inertias do not add up to the total duct inertia.

Assumption	L_u/L_d
1	0.37
2	0.89
3	0.51
4	2.45

Table A.4: Estimates of the Inertia Ratio for the LTS-101 Engine.

The "best" estimates for the surge model parameters for the LTS-101 engine at 95 percent speed are thus β=0.4, L_u/L_d=0.4, and ω_H=130 Hz.

A.5 Assessment of Modelling Assumptions for LTS-101 Engine

Using the best estimates for the LTS-101 engine model parameters the lumped parameter assumptions can be assessed, in particular, the negligence of compliance in the compressor duct and the quasi-steady compressor assumptions . Recall from Chapter 2, that the following inequality must be satisfied for the compressibility of an unsteady flow to be neglected:

$$\omega_R^* \cdot M << 1 \qquad (2.1)$$

The reduced frequency was defined as

$$\omega_R^* \equiv \frac{\omega_{US} \cdot L}{U} \qquad (2.2)$$

where, ω_{US} is a characteristic frequency of the unsteadiness

L is a characteristic length (i.e. duct length)

U is a characteristic velocity (i.e. mean flow velocity in the duct)

For the engine with no control the characteristic frequency of the unsteadiness is the linear surge frequency. Using the best estimates for the LTS-101 model parameters, the engine model of Chapter 2 predicts that the surge frequency is roughy 0.55 times the Helmholtz frequency. This corresponds to a surge frequency of rougly 72 Hz using the

best estimate for ω_H. The product of the reduced frequency and Mach number in Eqn. 2.1 is presented for the upstream (defined as regions I and II) and downstream ducts (defined as region IV) in Table A.5. The reduced frequency for the compressor (defined as regions III and IV) is also given.

$(\omega_R^* \cdot M)_u$	$(\omega_R^* \cdot M)_d$	$(\omega_R^*)_C$
0.3	0.1	1.1

Table A.5: Estimated Reduced Frequencies for LTS-101 Engine (No Control)

For the gas turbine engine with no control, these values indicate that the lumped parameter modelling of the compressor ducts may be adequate, although the compressor's unsteady response should be modelled (see Ref. 5). However, if a high bandwidth actuator is used to modulate the flow in the ducts or the compressor these assumptions may very well break down.

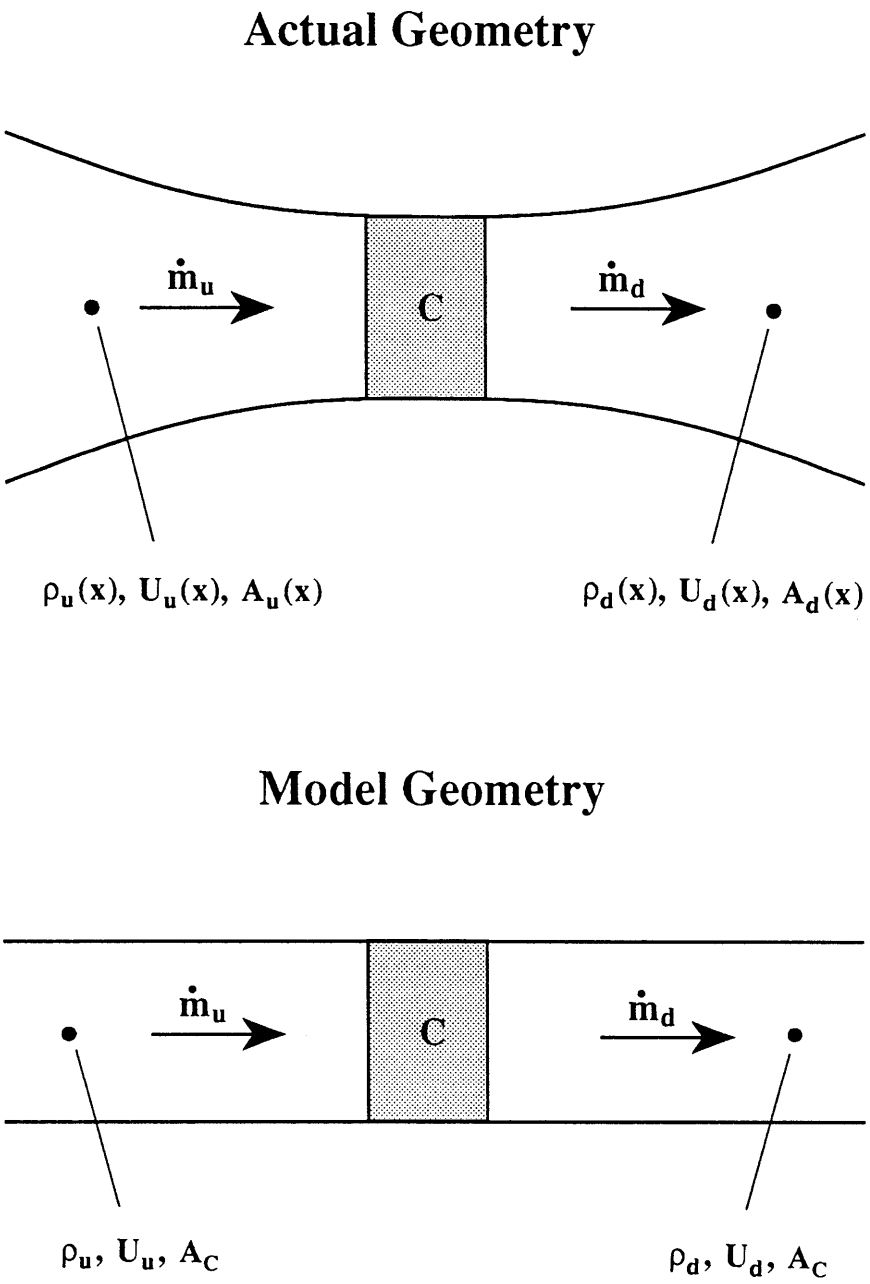

Figure A.1: Schematic of Compressor Duct Geometries.

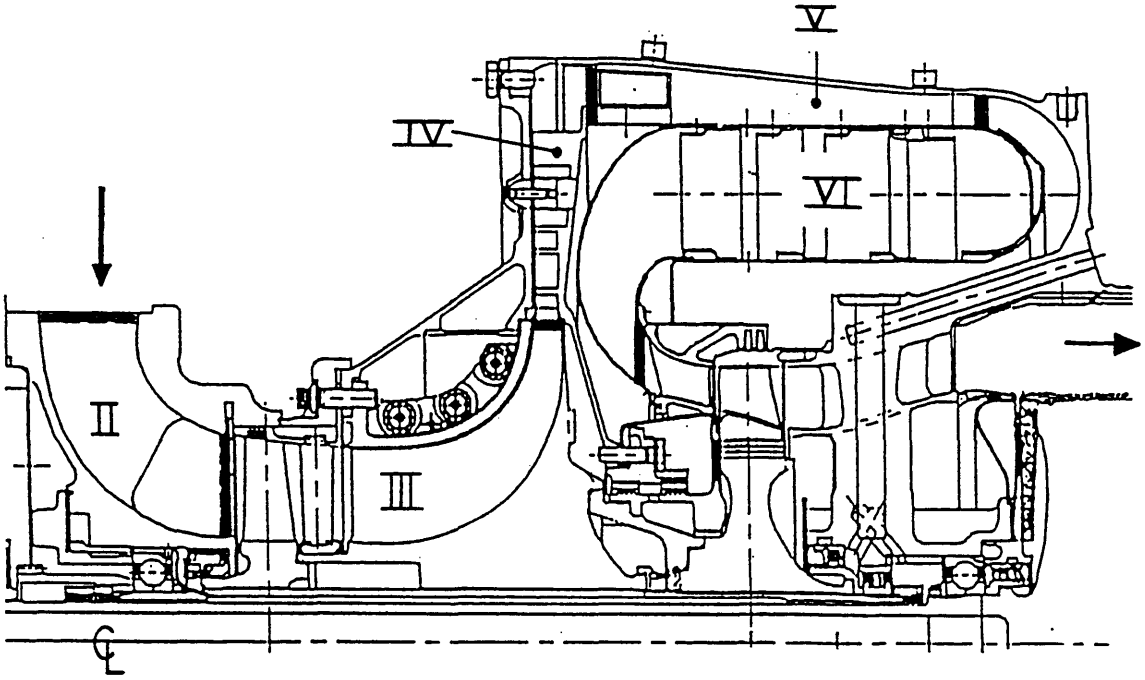

Figure A.2: Cross-Section of Lycoming LTS-101 Helicopter Engine.

Appendix B
Linearization of Gas Turbine Engine Surge Model

In this appendix the non-linear equations governing the gas turbine engine surge dynamics are linearized.

B.1 Recap of Non-Linear Governing Equations

The non-linear governing equations previously derived in Chapter 2 are rewritten here for convenience.

(Momentum Conservation)
$$\frac{dW_C}{d\tau} = \beta \cdot \frac{\left(\frac{L_u}{L_d} + 1\right)}{\left(\pi_C \cdot \frac{L_u}{L_d} + 1\right)} \cdot \left(\pi_C - P_B^*\right) \tag{2.30}$$

(Mass Conservation)
$$\frac{d\rho_B^*}{d\tau} = \frac{1}{\gamma \cdot \overline{T}_B^* \cdot \beta} \cdot \left(W_C - W_T\right) \tag{2.31}$$

(Energy Conservation)
$$\frac{dP_B^*}{d\tau} = \frac{1}{\overline{T}_B^* \cdot \beta} \cdot \left(W_C \cdot T_{O,4}^* - W_T \cdot T_B^*\right) + \dot{Q}^* \tag{2.32}$$

The additional relationships needed to solve these equations are also rewritten here for convenience.

$$\pi_C = \pi_C(W_{C,COR}, M_{tip,2}) \tag{2.13}$$

$$\theta_C = \theta_C(W_{C,COR}, M_{tip,2}) \tag{2.14}$$

$$W_{C,COR} = \frac{W_C \cdot \sqrt{T_{O,2}^*}}{P_{O,2}^*} = W_C \cdot \left(P_{O,2}^*\right)^{-\left(\frac{\gamma+1}{2\gamma}\right)} \tag{2.35}$$

$$M_{tip,2} = \frac{\overline{M}_{tip,a}}{\sqrt{T_{O,2}^*}} = \overline{M}_{tip,a} \cdot \left(P_{O,2}^*\right)^{-\left(\frac{\gamma-1}{2\gamma}\right)} \tag{2.36}$$

$$P_{O,2}^* = 1 - \frac{1}{\left(1 + \frac{L_d}{L_u}\right) \cdot \beta} \cdot \frac{dWc}{d\tau} \tag{2.37}$$

$$W_T = \frac{\overline{W}_T \cdot \sqrt{\overline{T}_B^*}}{\overline{P}_B^*} \cdot \sqrt{P_B^* \cdot \rho_B^*} \tag{2.39}$$

$$T_{O,2}^* = \left(P_{O,2}^*\right)^{\frac{\gamma-1}{\gamma}} \tag{2.38}$$

$$T_{O,4}^* = \theta_C \cdot \left(\frac{P_B^*}{\pi_C}\right)^{\frac{\gamma-1}{\gamma}} \tag{2.11}$$

Using these additional relationships the governing equations can be written in the following functional form:

(Conservation of Momentum) $$\frac{dW_C}{d\tau} = F_1\left(W_C, P_B^*, \frac{dW_C}{d\tau}\right) \tag{2.40}$$

(Conservation of Mass) $$\frac{d\rho_B^*}{d\tau} = F_2\left(W_C, \rho_B^*, P_B^*\right) \tag{2.41}$$

(Conservation of Energy) $$\frac{dP_B^*}{d\tau} = F_3\left(W_C, \rho_B^*, P_B^*, \frac{dW_C}{d\tau}\right) \tag{2.42}$$

These are three coupled, first-order, ordinary differential equations which are not only non-linear functions of the state variables W_C, ρ_B^* and P_B^*, but also the time derivative, $\frac{dW_C}{d\tau}$, through the effect of the upsteam inertia.

B.2 Linearization

To linearize Eqns. 2.40, 2.41 and 2.42 the equations are first written as implicit functions.

(Conservation of Momentum) $$G_1\left(W_C, P_B^*, \frac{dW_C}{d\tau}\right) = 0 \tag{B.1}$$

(Conservation of Mass) $$G_2\left(W_C, \rho_B^*, P_B^*, \frac{d\rho_B^*}{d\tau}\right) = 0 \tag{B.2}$$

(Conservation of Energy) $$G_3\left(W_C, \rho_B^*, P_B^*, \frac{dW_C}{d\tau}, \frac{dP_B^*}{d\tau}\right) = 0 \tag{B.3}$$

The Implicit Function Theorem from multi-variable calculus [40] is then used to linearize this system. The resulting linear system of equations are:

(B.4)

$$\frac{d}{d\tau}\begin{pmatrix}\hat{W}_C\\ \hat{\rho}_B^*\\ \hat{P}_B^*\end{pmatrix}=\begin{bmatrix} -\left\{\dfrac{G_{1,W_C}}{G_{1,\frac{dW_C}{d\tau}}}\right\} & 0 & -\left\{\dfrac{G_{1,P_B^*}}{G_{1,\frac{dW_C}{d\tau}}}\right\} \\ -G_{2,W_C} & -G_{2,\rho_B^*} & -G_{2,P_B^*} \\ \left\{-G_{3,W_C}+G_{3,\frac{dW_C}{d\tau}}\left\{\dfrac{G_{1,W_C}}{G_{1,\frac{dW_C}{d\tau}}}\right\}\right\} & -G_{3,\rho_B^*} & \left\{-G_{3,P_B^*}+G_{3,\frac{dW_C}{d\tau}}\left\{\dfrac{G_{1,P_B^*}}{G_{1,\frac{dW_C}{d\tau}}}\right\}\right\} \end{bmatrix}\cdot\begin{pmatrix}\hat{W}_C\\ \hat{\rho}_B^*\\ \hat{P}_B^*\end{pmatrix}$$

Stability of the compression system is determined by the eigenvalues of the **A** matrix in the above equation.

The elements of the Jacobian matrix (**A** matrix) are found by calculating the partial derivatives of the implicit functions. These derivatives are given below.

$$G_{1,W_C}=\left(\frac{\overline{\partial G_1}}{\partial W_C}\right)=-\left[\beta\cdot\frac{\left(\frac{L_u}{L_d}+1\right)}{\left(\pi_C\cdot\frac{L_u}{L_d}+1\right)}\right]\cdot\left(\frac{\overline{\partial\pi_C}}{\partial W_C}\right) \tag{B.5}$$

$$G_{1,P_B^*}=\left(\frac{\overline{\partial G_1}}{\partial P_B^*}\right)=\left[\beta\cdot\frac{\left(\frac{L_u}{L_d}+1\right)}{\left(\pi_C\cdot\frac{L_u}{L_d}+1\right)}\right] \tag{B.6}$$

$$G_{1,\frac{dW_C}{d\tau}}=\left(\frac{\overline{\partial G_1}}{\partial\left(\frac{dW_C}{d\tau}\right)}\right)=1-\left[\beta\cdot\frac{\left(\frac{L_u}{L_d}+1\right)}{\left(\pi_C\cdot\frac{L_u}{L_d}+1\right)}\right]\cdot\left(\frac{\overline{\partial\pi_C}}{\partial\left(\frac{dW_C}{d\tau}\right)}\right) \tag{B.7}$$

$$G_{2,W_C}=\left(\frac{\overline{\partial G_2}}{\partial W_C}\right)=-\frac{1}{\gamma\cdot\overline{T}_B^*\cdot\beta} \tag{B.8}$$

$$G_{2,\rho_B^*}=\left(\frac{\overline{\partial G_2}}{\partial\rho_B^*}\right)=\frac{1}{\gamma\cdot\overline{T}_B^*\cdot\beta}\cdot\left(\frac{\overline{\partial W_T}}{\partial\rho_B^*}\right) \tag{B.9}$$

$$G_{2,P_B^*}=\left(\frac{\overline{\partial G_2}}{\partial P_B^*}\right)=\frac{1}{\gamma\cdot\overline{T}_B^*\cdot\beta}\cdot\left(\frac{\overline{\partial W_T}}{\partial P_B^*}\right) \tag{B.10}$$

$$G_{3,W_C} = \left(\overline{\frac{\partial G_3}{\partial W_C}}\right) = -\frac{1}{\overline{T}_B^* \cdot \beta} \cdot \left(\overline{\theta}_C + \overline{W}_C \cdot \left(\overline{\frac{\partial T_{O,4}^*}{\partial W_C}}\right)\right) \tag{B.11}$$

$$G_{3,\rho_B^*} = \left(\overline{\frac{\partial G_3}{\partial \rho_B^*}}\right) = \frac{1}{\overline{T}_B^* \cdot \beta} \cdot \left(\overline{T}_B^* \cdot \left(\overline{\frac{\partial W_T}{\partial \rho_B^*}}\right) - \overline{W}_T \cdot \frac{\left(\overline{T}_B^*\right)^2}{\overline{P}_B^*}\right) \tag{B.12}$$

$$G_{3,P_B^*} = \left(\overline{\frac{\partial G_3}{\partial P_B^*}}\right) = \frac{1}{\overline{T}_B^* \cdot \beta} \cdot \left(-\overline{W}_C \cdot \left(\overline{\frac{\partial T_{O,4}^*}{\partial P_B^*}}\right) + \frac{\overline{T}_B^*}{\overline{P}_B^*} \cdot \overline{W}_T + \overline{T}_B^* \cdot \left(\overline{\frac{\partial W_T}{\partial P_B^*}}\right)\right) \tag{B.12}$$

$$G_{3,\frac{dW_C}{d\tau}} = \left(\overline{\frac{\partial G_3}{\partial\left(\frac{dW_C}{d\tau}\right)}}\right) = -\frac{\overline{W}_C}{\overline{T}_B^* \cdot \beta} \cdot \left(\overline{\frac{\partial T_{O,4}^*}{\partial\left(\frac{dW_C}{d\tau}\right)}}\right) \tag{B.13}$$

The chain rule is used to find the other partial derivatives required above:

$$\left(\overline{\frac{\partial \pi_C}{\partial W_C}}\right) = \overline{m}_C \tag{B.14}$$

$$\left(\overline{\frac{\partial \pi_C}{\partial\left(\frac{dW_C}{d\tau}\right)}}\right) = \overline{m}_C \cdot \left(\overline{\frac{\partial W_{C,COR}}{\partial\left(\frac{dW_C}{d\tau}\right)}}\right) + \left(\overline{\frac{\partial \pi_C}{\partial M_{tip,2}}}\right) \cdot \left(\overline{\frac{dM_{tip,2}}{dP_{O,2}^*}}\right) \cdot \left(\overline{\frac{dP_{O,2}^*}{d\left(\frac{dW_C}{d\tau}\right)}}\right) \tag{B.15}$$

$$\left(\overline{\frac{\partial W_{C,COR}}{\partial\left(\frac{dW_C}{d\tau}\right)}}\right) = \left(\overline{\frac{\partial W_{C,COR}}{\partial P_{O,2}^*}}\right) \cdot \left(\overline{\frac{dP_{O,2}^*}{d\left(\frac{dW_C}{d\tau}\right)}}\right) \tag{B.16}$$

$$\left(\overline{\frac{\partial T_{O,4}^*}{\partial W_C}}\right) = \left(\overline{\frac{\partial T_{O,4}^*}{\partial \pi_C}}\right) \cdot \left(\overline{\frac{\partial \pi_C}{\partial W_C}}\right) + \left(\overline{\frac{\partial T_{O,4}^*}{\partial \theta_C}}\right) \cdot \left(\overline{\frac{\partial \theta_C}{\partial W_C}}\right) \tag{B.17}$$

$$\left(\overline{\frac{\partial T_{O,4}^*}{\partial\left(\frac{dW_C}{d\tau}\right)}}\right) = \left(\overline{\frac{\partial T_{O,4}^*}{\partial \theta_C}}\right) \cdot \left(\overline{\frac{\partial \theta_C}{\partial\left(\frac{dW_C}{d\tau}\right)}}\right) + \left(\overline{\frac{\partial T_{O,4}^*}{\partial \pi_C}}\right) \cdot \left(\overline{\frac{\partial \pi_C}{\partial\left(\frac{dW_C}{d\tau}\right)}}\right) \tag{B.18}$$

$$\left(\overline{\frac{\partial \theta_C}{\partial\left(\frac{dW_C}{d\tau}\right)}}\right) = \left(\overline{\frac{\partial \theta_C}{\partial W_{C,COR}}}\right) \cdot \left(\overline{\frac{\partial W_{C,COR}}{\partial\left(\frac{dW_C}{d\tau}\right)}}\right) + \left(\overline{\frac{\partial \theta_C}{\partial M_{tip,2}}}\right) \cdot \left(\overline{\frac{dM_{tip,2}}{dP_{O,2}^*}}\right) \cdot \left(\overline{\frac{dP_{O,2}^*}{d\left(\frac{dW_C}{d\tau}\right)}}\right) \tag{B.19}$$

where,

$$\left(\overline{\frac{\partial W_{C,COR}}{\partial P^*_{O,2}}}\right) = -\frac{(\gamma+1)}{2\gamma}\cdot\overline{W}_C \tag{B.20}$$

$$\left(\overline{\frac{dP^*_{O,2}}{d\left(\frac{dW_C}{d\tau}\right)}}\right) = -\left(\frac{1}{\left(1+\frac{L_d}{L_u}\right)\cdot\beta}\right) \tag{B.21}$$

$$\left(\overline{\frac{dM_{tip,2}}{dP^*_{O,2}}}\right) = -\frac{(\gamma-1)}{2\gamma}\cdot\overline{M}_{tip,a} \tag{B.22}$$

$$\left(\overline{\frac{\partial T^*_{O,4}}{\partial \pi_C}}\right) = -\frac{(\gamma-1)}{\gamma}\cdot\frac{\overline{\theta}_C}{\overline{\pi}_C} \tag{B.23}$$

$$\left(\overline{\frac{\partial T^*_{O,4}}{\partial \theta_C}}\right) = 1 \tag{B.24}$$

$$\left(\overline{\frac{\partial T^*_{O,4}}{\partial P^*_B}}\right) = \frac{(\gamma-1)}{\gamma}\cdot\frac{\overline{\theta}_C}{\overline{\pi}_C} \tag{B.25}$$

$$\left(\overline{\frac{\partial \theta_C}{\partial W_C}}\right) = \left(\overline{\frac{\partial \theta_C}{\partial W_{C,COR}}}\right) \tag{B.26}$$

These equations along with the specified values of β, L_u/L_d, $\overline{m}_C$, $\overline{\pi}_C$, $\overline{W}_{C,COR}$, $\overline{M}_{tip,2}$, $\left(\overline{\frac{\partial(\pi_C)}{\partial(M_{tip,2})}}\right)$, $\overline{\theta}_C$, $\left(\overline{\frac{\partial(\theta_C)}{\partial(W_{C,COR})}}\right)$, $\left(\overline{\frac{\partial(\theta_C)}{\partial(M_{tip,2})}}\right)$, $\left(\overline{\frac{\partial(W_T)}{\partial(\rho^*_B)}}\right)$, $\left(\overline{\frac{\partial(W_T)}{\partial(P^*_B)}}\right)$ and $\overline{T}^*_B$ (see Section 2.3.1) determine the open-loop linear stability of the gas turbine engine.